Using Small Molecules and Peptides as Chemical Tools to Study Metal-Amyloid, Membrane-Amyloid, and Peptide-Amyloid Interactions

by

Amit S. Pithadia

A dissertation submitted in partial fulfillment
of the requirements for the degree of
Doctor of Philosophy
(Chemistry)
in the University of Michigan
2016

Doctoral Committee:

Professor Ayyalusamy Ramamoorthy, Co-Chair
Professor Carol A. Fierke, Co-Chair
Professor Zaneta Nikolovska-Coleksa
Professor Brandon Ruotolo
Professor John P. Wolfe

2016

Acknowledgements

First and foremost, I would like to thank my advisers, Professor Ayyalusamy Ramamoorthy and Professor Carol Fierke for their dedication, support and enthusiasm for research throughout my time at the University of Michigan. They are truly incredible mentors and individuals. They helped me during desperate times and without their guidance and mentorship, I would not have completed my Ph.D. I am very lucky to have two brilliant and energetic advisers who have helped shape me into the researcher I am today. Importantly, they have instilled in me the values of being a diligent student, both academically and in life.

I would also like to acknowledge my committee Professors John Wolfe, Brandon Ruotolo, and Zaneta Nikolovska-Coleska. Professor Wolfe has been a remarkable teacher and has encouraged me throughout the course of graduate school. He has also been great at putting science and life into perspective. Additionally, Professor Ruotolo has been a frequent collaborator and valuable resource for my projects. His knowledge of amyloids has helped shape many of the problems on during my dissertation. I would like to also acknowledge Professor Ruotolo's group members, specifically Dr. Molly Soper and Dr. Richard Kerr for providing insights into science and being available for meaningful discussions. Lastly, Professor Nikolovska-Coleksa has been very positive and enthusiastic to learn about my projects and see my progression over the years. She has always provided great feedback and asked meaningful questions which has helped me understand my projects from a different light.

I would like to acknowledge Professor Mi Hee Lim and her group members. I began my Ph.D in her laboratory and she truly helped me become a critical thinker as well as helped

broaden my experimental scope. It was a pleasure working for her and much of my degree is owed to her support and mentorship. It was a great experience working alongside intelligent and charismatic scientists in the Lim lab, specifically, Dr. Joseph Braymer, Dr. Jung-Suk Choi, Dr. Alaina DeToma, Dr. Michael Beck, and Dr. Masha Savelieff. Drs. Braymer and DeToma were my scientific big brother and sister, respectively and are two individuals I could always count on to help me through good and bad times.

I would additionally like to thank past and present members of the Ramamoorthy and Fierke groups that have provided support and plentiful insights throughout my time at UM. A special thanks to my endearing RAMyloiders: Dr. Patrick Walsh, my fellow flannel Friday followers: Dr. Sam Kotler and Kyle Korshavn, Dr. Jeffrey Brender, Kian Kamgar-Parsi, Dr. Anirban Bhunia, and the talented Michael McCullough. Additional gratitude to Dr. Kamal Mroue, Dr. Kazutoshi Yamamoto, Dr. Rongchun Zhang, Meng Zhang and Katie Gentry who been critical toward my progress as well as the best morning coffee group at U of M. Members of the Fierke lab have been great asset to help me assimilate into my new settings and expose me to different areas of science I was not familiar with. A special thank you is due to Andrea Stoddard who worked with me from the beginning to help me understand molecular biology and protein prep. Dr. Byungchul Kim, Dr. Michael Howard and Eric Sullivan, for always providing me with laughs and the afternoon pick-me-up coffee.

Furthermore, I would like to thank my family (parents, siblings, aunts, uncles, grandparents, cousins, etc.). It was difficult for them to have me away from home for so long, but their unconditional love and support is the reason I am who I am today, someone they can be proud of. My parents, Snehal and Asha have always been my brain and heart, teaching me compassion, humility and respect. My brothers, Hiral and Sagar have always been my arms and

legs, giving me support and strength. Both of my grandmothers, though do not understand anything I do, have cheered me on since day 1. Without my friends, I would not have an outlet. There are too many people to name here, but each and every single person that has stayed with me through this journey has had their role in my success and I owe them a special thanks from the bottom of my heart. Always save the best for last. I would like to thank my fiancée, Namrata (Niki) for being my rock, my cheerleader and my friend. Without her, I would not be a hard-working, patient, fun man I am today.

Table of Contents

List of Figures

List of Tables

List of Appendices

Abstract

Amyloid proteins are a family a proteins that are characterized by the misfolding an intrinsically disordered monomer subunit into an ordered beta-sheet fibril. Recent evidence has suggested that the monomer and fibril species are relatively inert; however, aggregates along the misfolding pathway are directly linked to cytotoxicity. It is known that biological cofactors and membranes may play a part in these deleterious events. Specifically metal ions and lipid bilayers may have a role in amyloid-associated toxicity through misregulation of metal ions and generation of oxidative stress with redox active metal ions or disruption of membrane integrity through pore formation and fragmentation of the bilayer. In order to better understand how metal ions and lipid bilayers are involved with amyloid aggregation and toxicity, small molecules can be used as chemical tools. A series of diphenylpropynone derivatives were developed to study the interaction of bifunctional ligands on metal-Aβ aggregation. Both **DPP1** and **DPP2** showed reactivity toward metal–Aβ species over metal-free Aβ species to different extents. In particular, **DPP2**, which contains a dimethylamino group, exhibited greater reactivity with metal–Aβ species than **DPP1**. Small molecules can also be applied as chemical modulators for lipid-associated amyloid aggregation. A curcumin derivative, **CurDAc**, was developed to investigate the mitigation of hIAPP aggregation in the absence and presence of lipid membrane. **CurDAc** showed tremendous inhibitory propensity for both lipid-free and lipid-assisted IAPP aggregation in vitro, making it an ideal candidate for further SAR studies.

To gain insights into the misfolding pathway and oligomerization of amyloid proteins, the self-assembly of TK9, a nine-residue peptide and its variants were characterized through biophysical, spectroscopic, and simulated studies, and it was confirmed that the structure of these peptides influences their aggregation propensity, hence, mimicking amyloid proteins. This peptide also showed promise as a chemical inhibitor for hIAPP aggregation.

Through this work, insights into effective structural scaffold to modify amyloid aggregation in the presence of biological cofactors are understood. Moreover, the discovery of a structural scaffold to monitor oligomer and fibril formation in order to elucidate species along the misfolding pathway has also been made.

Chapter 1: Introduction

Portions of this chapter have been adapted from the following publications:

Pithadia A. S.; Lim, M. H. *Curr. Opin. Chem. Biol*. **2012**, *16*, 67-73.

Patel, H. R.; **Pithadia, A. S**.; Brender, J. R.; Fierke, C. A.; Ramamoorthy, A. *J. Phys Chem. Lett*. **2014**, 5, 1864.

Pithadia, A. S.; Brender, J. A.; Fierke C. A.; Ramamoorthy, A. *J. Diabetes Res.*, **2016**. Article ID 2046327, doi: 10.1155/2016/2046327.

1.1 Introduction

Amyloidosis is a condition belonging to a growing family of degenerative systemic and neurological diseases in which major component of degenerative processes is the amyloid formation.[1] These amyloids are insoluble deposits formed by protein precursor assembles into highly ordered β-sheet-rich fibers observed in distinctly intracellular and extracellular locations.[2,3] Amyloids are characterized by a cross-β sheet quaternary structure, in which individual beta-strands are thought to be oriented orthogonal to the long fiber axis.[4] Diseases, such as Alzheimer's, and Type II Diabetes, have also been linked with the formation of such complex misfolded amyloid proteins (amyloid-β (Aβ) and human islet amyloid polypeptide (hIAPP), respectively); however, there appears to be little or no sequence homology between the peptides involved in the various amyloid diseases.[5] A growing body of evidence suggests that fibril formation may follow similar pathways: a nucleation process (Figure 1.1), in which the formation of numerous small oligomeric assemblies, also known as prefibrillar aggregates, of

proteins is believed to precede the formation of mature fibrils and be closely associated with cell death and cytotoxicity.[6-9]

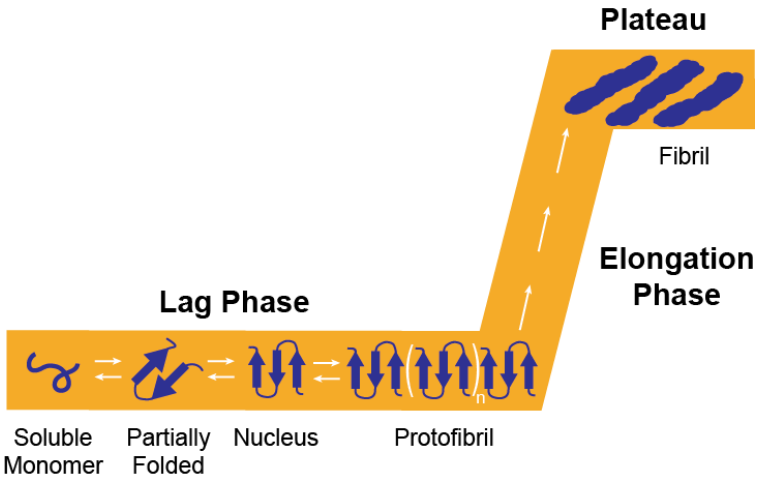

Figure 1.1. Kinetic growth model of amyloid proteins. During the lag phase, there is the intrinsicly disordered monomer aggregates to form low molecular weight oligomers and protofibrils which then self associate during the elongation phase to form insoluble protenacious fibrils.

1.1.1 Amyloid-beta (Aβ)

Monomeric Aβ peptides (39 − 43 amino acids in length) are generated *via* the cleavage of amyloid precursor protein (APP) by β− and γ−secretases [10-14]. These peptides are composed of a hydrophilic *N*-terminal region (1 − 28) and a hydrophobic *C*-terminal region (29 − 39/43). Two common forms of amyloidogenic Aβ peptides found in the AD brain are A$\beta_{1\text{-}40}$ and A$\beta_{1\text{-}42}$, with present indication being that A$\beta_{1\text{-}42}$ is the predominant component in senile plaques; it is also considered to be more toxic than A$\beta_{1\text{-}40}$ [10-13]. The generated monomeric Aβ species have the capability to aggregate, mainly through hydrophobic interactions [1]. Residues L17 – A21 and G29 – M35 have been suggested to form an internal β-sheet structure, which is stabilized by a salt bridge (residues K28 and D23/E22). L17 – A21 have been suggested to be a self-recognition site which can be important in forming higher order structures via hydrophobic

interactions. Aβ monomers and dimers containing these β-sheet structures can have contacts (e.g. hydrophilic interactions and hydrogen bonding) to form further aggregated species (e.g., oligomers, fibrils). Recent reports indicate that low molecular weight oligomeric Aβ species may be the most relevant to AD pathogenesis [11,14,15]. It is, however, still not completely understood which conformation of Aβ species is responsible for the pathology of AD.

1.1.2 Islet Amyloid Polypeptide (IAPP)

Islet Amyloid Polypeptide (IAPP, also known as amylin) is a 37-residue hormone produced and secreted in the pancreas has a role in controlling metabolic functions.[16] There is strong evidence which suggests that the aggregation of hIAPP plays a significant role in β-cell death, an important step in the transition from insulin resistance to overt type II diabetes.[17] It is well known through *in vitro*, tissue culture, and postmortem clinical examinations that hIAPP aggregate formation is correlated with the development of type II diabetes and can be implicated in the severity of the disease.[17] A causative role for IAPP in the etiology of type II diabetes has become clearer in recent years with the development of transgenic animal models that express the human variant of IAPP. Animals (such as rats) which do not spontaneously develop type II diabetes have an IAPP variant which does not readily form amyloid fibers and is also non-cytotoxic.[18] However, transgenic rats expressing the amyloidogenic hIAPP develop type II diabetes with metabolic characteristics similar to human type II diabetes.[19,20] A current hypothesis is that overt type II diabetes develops when a combination of genetic and environmental factors, most of which are unknown at present, make an individual susceptible to β-cell death induced by hIAPP aggregation.[17] In the prediabetic stage of diabetes, insulin resistance is partly compensated for by increased insulin production.[21] However, increased insulin production also leads to increased hIAPP production as both are co-secretion products,

hence, physiologically connected.[16] The increased production of hIAPP in the prediabetic stage is believed to lead to the death of β-cells, starting a biochemical cycle that progresses as the disease worsens into overt type II diabetes.[17] Although hIAPP aggregation is not likely to be the sole cause of diabetes, it is proposed to play a major role in the development and progression of the disease.

1.1.3 Metal Ions and Aβ

Metal ions play essential roles throughout the body, especially in the brain [13,22−25]. Maintaining the homeostasis and compartmentalization of metal ions in the brain is necessary for proper neurological functions. Evidence has demonstrated that transition metals such as Cu, Zn, and Fe are colocalized in high micromolar to low millimolar concentrations in amyloid plaques (*ca*. 0.4 mM for Cu, 1 mM for Zn, and 0.9 mM for Fe) [11,13,14,25,26]. This observation may serve as a link to explain metal ion dyshomeostasis in the AD brain.

Copper (Cu) exists under physiological conditions in both reduced (Cu(I)) and oxidized (Cu(II)) forms and is controlled tightly by biological ligands (*e.g*., proteins) [22-24]. Zinc, on the other hand, is not redox active and exists as Zn(II) in biological systems. Both Cu and Zn ions have been found to serve a role in neurotransmission activity and are present in micromolar concentrations in the synaptic cleft [13,24-27]. Also, Cu and Zn have been shown to co-purify with Aβ plaques in *post mortem* brains. Different from Cu and Zn, Fe has not been determined to co-purify with Aβ, but is still present in high amounts in Aβ plaques [13,27]. Taken together, the findings of the abundant levels of Cu, Zn, and Fe in Aβ plaques have triggered extensive investigations of metal-Aβ interaction/reactivity and its implications in AD pathology.

Through a variety of techniques, Cu(II) and Zn(II) have been shown to interact with Aβ in a 1:1 metal to Aβ binding stoichiometry; however, binding modes and coordination

environments of metal ions in Aβ are variable and dependent on experimental conditions [14, 26-32]. Though Cu-Aβ can exist in many forms depending on pH, in the physiological pH range primarily exists in two forms: component I (between pH 6.0 and 8.0) and component II (slightly above pH 8.0. At pH 7.4 (physiological pH), it has been observed that Cu(II) binding to Aβ involves three nitrogen donor atoms and one oxygen donor atom (3N1O, component I). In this binding mode, the nitrogen donor atoms are possibly from three histidine (His) residues (His6, His13, His14) or two His ligands and the amine of the *N*-terminal region. Based on EPR and isotopic labeling studies the source of the oxygen donor atom has most likely been proposed to be from Asp1 in both nitrogen binding modes [33]. At pH *ca.* 8.0, metal binding (component II) can occur *via* three His residues (nitrogen donor atoms) and the carbonyl group of Ala2 (oxygen donor atom) or a combination of the *N*-terminal amine, a His residue and amide backbone nitrogen, and carbonyl from Ala2 [33]. It has also been proposed that the four coordinating ligands in component II are the *N*-terminal amine or a deprotonated backbone amide with three His residues. In the case of Zn(II), the metal ion has shown to bind to Aβ *via* three His residues, but a total of four to six coordinating ligands on the metal center has been suggested [14,28,29]. Other ligands proposed to be involved in Zn(II) binding are Asp1, Glu11, and possibly, Arg5. Unlike Cu(II) and Zn(II), relatively less has been known about the coordination of Fe(II/III) and Cu(I) to Aβ species [28,34-38]. Studies have proposed a two coordinate linear binding geometry of monomeric Aβ to Cu(I) and oligomeric Aβ-Cu(I) complexes have a tetrahedral coordination geometry [36]. Overall, metal ions have been demonstrated to bind to Aβ species through nitrogen and oxygen sources in the peptide.

1.1.4 Metal-Aβ-Induced Neurotoxicity

Metal-Aβ species have been studied to determine their contribution to AD neuropathogenesis [14, 39-41]. Several findings have suggested that two avenues for metal-Aβ species are linked to neurotoxicity: The facilitation of Aβ aggregation and the induction of oxidative stress through ROS generation, leading to neuronal cell death and cognitive impairment.

Both Cu and Zn ions, found at and around the synapse, could be involved in the process of generating Aβ aggregates and their accumulation in the synaptic cleft [24-26,29,41]. At physiological pH, Zn(II) could cause Aβ to aggregate into amorphous insoluble aggregates within milliseconds at concentrations below 100 *m*M [42,43]. Depending on experimental conditions, Cu(II) could promote the formation of fibrillar or amorphous aggregates and also accelerate the rate of nucleated aggregate formation relative to metal-free conditions [43]. These studies demonstrate that Aβ aggregation can be advanced in the presence of metal ions. The neurotoxic effects that could be induced by metal-Aβ species may be related to the disruption of membranes leading to apoptosis and/or aggregate accumulation at and around the synapse resulting in weakened cell signaling and neuronal death [11].

The second avenue of neurotoxicity is associated with oxidative stress. Cu(I/II) and Fe(II/III) are redox active metal ions and can undergo redox cycling in the presence of dioxygen (O_2) and a reducing agent producing ROS [10,11,13,39-41]. When metal ions are surrounded by Aβ species, ROS such as hydrogen peroxide (H_2O_2) and hydroxyl radicals (•OH) can be generated. Though a clear understanding of the mechanistic pathway is presently unknown, it has been suggested that internal sources such as Met35 at *C*-terminus of Aβ or external sources such as ascorbate could provide electrons for the redox cycle [26]. Cu(I)-Aβ oligomers can form a highly O_2 reactive Cu(I) center, which can also assist in the formation of ROS [36]. In the AD

brain, an imbalance between production and removal of ROS can be observed. Along with the dysfunction of neuroprotective systems such as catalases and superoxide dismutases, the overproduction of ROS can trigger oxidative damage of biological targets (*e.g.*, lipids, proteins, DNA) as well as oxidation of Aβ peptides (e.g., the formation of dityrosine bond (Tyr10-Tyr10) and three electron bond (Met35-Met35) between two peptides) resulting in the acceleration of Aβ aggregation [11, 27].Overall, metal-induced Aβ aggregation and oxidative stress could be attributed to a high degree of neurotoxicity leading to neuronal death and ultimately, cognitive impairment. This correlation is still not completely understood; thus, further investigations are necessary in order to advance our understanding of metal-Aβ-involved neuropathogenesis in AD.

1.1.5 Membranes play a critical role in both IAPP fibrillogenesis and toxicity

Fibrillization of IAPP can be affected by many factors. Of these, phospholipid membranes are perhaps the most important.[44,45] Membranes have a two-fold effect on IAPP. First, membranes can greatly accelerate the rate of fiber formation by IAPP.[46,47] Aggregation of IAPP, in turn, has been linked to numerous pathologies.[1] Some of these pathologies include the formation of reactive oxygen species in the presence of redox active metal ions,[48] endoplasmic reticulum stress caused by the accumulation of misfolded proteins,[49] and an inflammatory response triggered by IAPP amyloid fibers.[50,51] Membranes can therefore indirectly contribute to the cytotoxicity of IAPP by accelerating the formation of these toxic species.

Second, and perhaps more importantly, IAPP can directly disrupt plasma and possibly organelle membranes during aggregation through two processes: the generation of pores and the eventual fragmentation of the lipid bilayer through a detergent-like mechanism (Figure 1.2).[52,53] Disruption of cellular membranes leads to an immediate influx of Ca^{2+}, which if not

controlled, initiates the process of apoptosis. Severe membrane disruption can lead to immediate necrosis through the leakage of critical cellular contents. The cell membrane therefore contributes both directly and indirectly to IAPP toxicity as both a site for the accumulation of toxic oligomers and as a target for their cytotoxic effect.

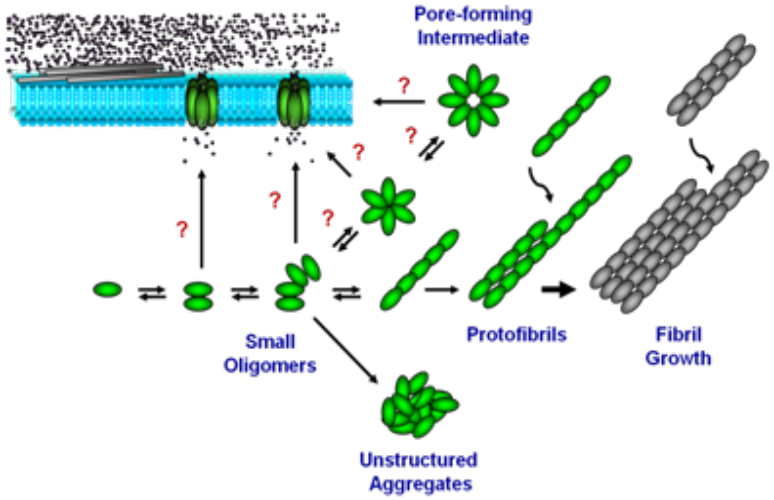

Figure 1.2: Potential routes towards the formation of toxic oligomers and amyloid fibers from the monomeric state via multiple intermediate states.

Traditionally, membrane disruption by amyloidogenic proteins has been thought to be the result of the formation of unregulated ion channels in the membrane that resemble traditional barrel-stave pores in many respects. In the channel hypothesis, small annular oligomers of IAPP possessing a hydrophobic exterior and hydrophilic interior insert into the membrane, spanning the bilayer.[54] The hollow structure of the oligomers allows ions to cross through the hydrophilic interior of the pore, causing an unregulated influx of Ca^{2+} into the cell (Figure 1.2).[55] Since cells are highly sensitive to perturbations in ionic strength, a small perturbation in intracellular calcium levels caused by unregulated IAPP channels can trigger an apoptotic cascade.[56]

While the channel hypothesis accounts for many facets of IAPP membrane disruption, it does not account for known facts about IAPP membrane interactions. First, large IAPP aggregates are the most disruptive to membranes, mirroring observations from other amyloid proteins.[57,58] This finding is surprising in light of the channel hypothesis, which would predict such large spherical aggregates could not easily form ion channels unless disassembled into smaller oligomers.[59] Second, aggregation of IAPP is often accompanied by large-scale morphological changes in the membrane, such as induction of excessive membrane curvature that would not be expected by the insertion of small oligomeric pores.[60-62] Finally, the time-course of membrane disruption is strongly correlated with amyloid fibril formation and can be altered by seeding amyloid formation, implying a direct link between fibril formation and membrane disruption. It is difficult to reconcile this observation with a pore-dominated mechanism, as the dimensions of a fibril or protofibril are too large to form pores of a traditional type. These findings suggest the process of fiber formation disrupts the integrity of the membrane by some unknown process. Although it is fairly clear that a strong interaction between prefibrillar IAPP and the membrane is involved, the actual process by which IAPP and other amyloidogenic proteins fragment the membrane remains almost completely uncharacterized.

1.1.6 Chemical Reagents for Targeting and Modulating Metal-Aβ Species

In order to identify the relationship between metal-Aβ interaction/reactivity and AD initiation/progression, suitable chemical reagents, capable of targeting metal-Aβ species specifically and regulating their interaction/reactivity, would be valuable. For this purpose, current efforts have been directed toward a rational structure based design of small molecules that can directly interact with both metal ions and Aβ. [63-65] The basic concept of this design

principle is that the two structural moieties for bifunctionality (metal chelation and Aβ interaction) must be in the same molecule.

Traditional metal chelators have been used to sequester and/or redistribute metal ions from metal-bound Aβ species in order to suppress metal-mediated Aβ aggregation and neurotoxicity *in vitro* and *in vivo*. Specifically, clioquinol (CQ, 5-chloro-7-iodo-8-hydroxyquinoline) and its derivative (PBT2) have been able to reduce metal-induced Aβ aggregation, Aβ plaque deposition, and ROS generation *in vitro and in vivo*, leading to improved cognition [42,43]. In addition to the metal chelation property, the ability of the compounds to interact with Aβ is necessary in order to target metal-Aβ species specifically in heterogeneous settings like the brain. Among Aβ imaging agents, *p*-I-stilbene has been used and shown to have appropriate properties for brain applications (*e.g.*, blood-brain barrier permeability) [68]. It has been illustrated that introducing different substituents into stilbene derivatives could tune their binding affinity for Aβ [64]. Thus, the frameworks from these known imaging agents are a small portion of known compounds which may be employed as Aβ interacting scaffolds toward the construction of new chemical reagents for metal-Aβ species.

Utilizing the structural moieties for bifunctionality (metal chelation and Aβ interaction), two synthetic approaches (linkage and incorporation) have been taken to fashion small molecules toward targeting and modulating metal-Aβ species [13,14,63,64].

On the basis of the incorporation approach, a metal chelation site can be directly installed into an Aβ interacting framework to produce a small molecule having bifunctionality (*vide infra*). As an example, the stilbene derivative, L2-b, was created *via* inclusion of two nitrogen donor atoms on the structure of an Aβ imaging agent (*p*-I-stilbene) [69]. L2-b has been shown to control metal-induced Aβ aggregation *in vitro*, as well as target and break down Aβ aggregates

isolated from human AD brain tissue homogenates containing a certain amount of metal ions. L2-b was also capable of diminishing ROS generation by Cu-Aβ *in vitro* and reducing metal-Aβ neurotoxicity in human neuroblastoma cells [69]. Specific disruption between metal ions and Aβ followed by the control of their reactivity using chemical reagents in the diseased settings could deepen our understanding of their direct correlation to the pathogenesis, which could contribute to new directions of diagnostic and therapeutic discovery for AD.

1.1.6 Natural products are natural choices for amyloid intervention

Particular areas of interest toward discovering agents against amyloidosis have been natural products. Natural products are small molecules found abundantly in nature, particularly in foods, and have been the main source for early medicines and therapeutics. They feature specific scaffolds that have made them beneficial receptor agonists, enzyme activators, inhibitors of protein-protein and DNA-protein interactions and channel openers.[70] Some natural products have also been shown to act as colloidal species which can sequester low molecular weight aggregates and prevent their fibrillation.[71] Importantly, natural products often exhibit better pharmacological profiles than their synthetic counterparts, especially with regard to toxicity and absorption.[70] Based on early successes, naturals products such as flavonoids and curcuminoids have been extensively researched in regards to reduction of the amyloid associated toxicity of Aβ and α-synuclein.

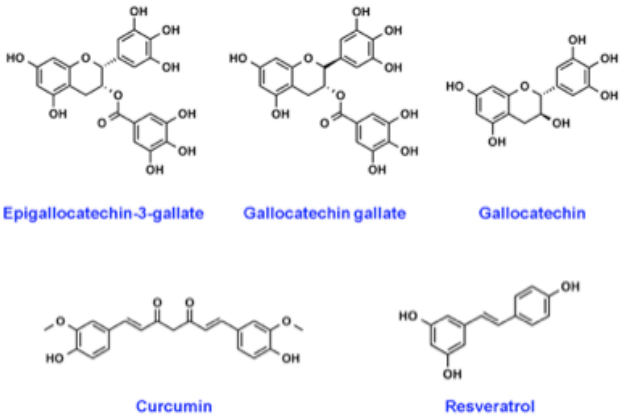

Figure 1.3. Chemical structures of the most studied polyphenolic small molecule inhibitors of hIAPP aggregation: Epigallocatechin Gallate (EGCG), Gallocatechin Gallate (GCG), Gallocatechin (GC), curcumin, and resveratrol.

There have been two main approaches to blocking the toxicity associated with amyloid aggregation. The first approach is to reduce toxicity by preventing the toxic species from forming. The second approach attempts to mediate the effects of the toxic oligomer formation by serving as an antioxidant to reduce the reactive oxygen species (ROS) generated by the aggregation process,[72, 73] reduce inflammatory effects,[74] prevent membrane association,[75, 76] or block the channels created by the peptide.[77-80] Given their ability to target multiple facets of amyloid-associated toxicity through their anti-inflammatory, antioxidant, and anti-amyloidogenic properties,[81, 82] natural products make a very promising class of candidates as viable small molecule inhibitors toward amyloids, specifically hIAPP. Through more stringent investigations, the use of natural products as aggregation modulators of hIAPP has provided more direct structural information about the hIAPP aggregation process itself. Herein, we will discuss the application of small molecule natural products toward the modulation of hIAPP aggregation with a particular focus on the most studied natural products, epigallocatechin-3-gallate (EGCG), curcumin, and resveratrol (Figure 1.3).

1.1.7 Methods to study amyloid aggregation and misfolding pathways

Identifying adequate structures of individual species involved in the fibrillation process is still extremely difficult.[83] Currently, most of the approaches to analyze the misfolding of IAPP are based on the Aβ protein, which is a more extensively studied amyloidogenic protein than hIAPP. A common method to investigate the process of fibril formation has been the thioflavin T (ThT) based fluorescence assay as it provides indirect evidence of how individual monomers convert into oligomeric species and eventually to the growth of fibrillar IAPP (Figure 1.4). Although this method is usually sensitive and reliable for most amyloidogenic proteins in the absence of other cofactors such as small molecule inhibitors, in some cases it cannot differentiate between oligomeric intermediates.[84] Furthermore, the ThT fluorescence is dependent on the surface charge of the fiber and therefore can give skewed results with alterations of pH[85] or when highly charged amyloidogenic proteins are considered.[86] A more serious complication occurs when small molecule inhibitors are introduced, as these often have either an intrinsic fluorescence that interferes with ThT detection[87] or bind to a similar site on the amyloid fiber, resulting in a false positive from competitive inhibition.[88]

Another method to follow the conformational transitions involved in IAPP amyloid formation is circular dichroism (CD) (Figure 1.4).[89] Changes in secondary structure content can be followed through CD during the fibrillation process. While CD can effectively distinguish between monomers and aggregates, it does not distinguish specifically between amyloid fibers and other β-sheet containing aggregates and it needs to rely on other techniques for quantitative prediction in this respect. CD is also problematic in inhibition studies when compounds that absorb in the near-UV range are considered. Time evolution of the size of aggregates can be tracked by dynamic light scattering (DLS) but the heterogeneous nature of the aggregates pose tremendous challenges to the application of DLS experiments. And, the accuracy of light

scattering experiments on small complexes is severely affected by the presence of even a small percentage of high-molecular weight species such as amyloid fibers.[90] This can be partially eliminated by running the solution through a size exclusion column (SEC) prior to acquisition. However, in general, separation based techniques can suffer from serious artifacts when applied to weakly associating aggregates like early intermediates. A careful study showed that SDS gels, a common method for detecting non-fibrillar aggregates, can underestimate the size of oligomers by more than a factor of 20 by fragmenting larger oligomers.[91] Similar, although less severe, results have been obtained with SEC in the

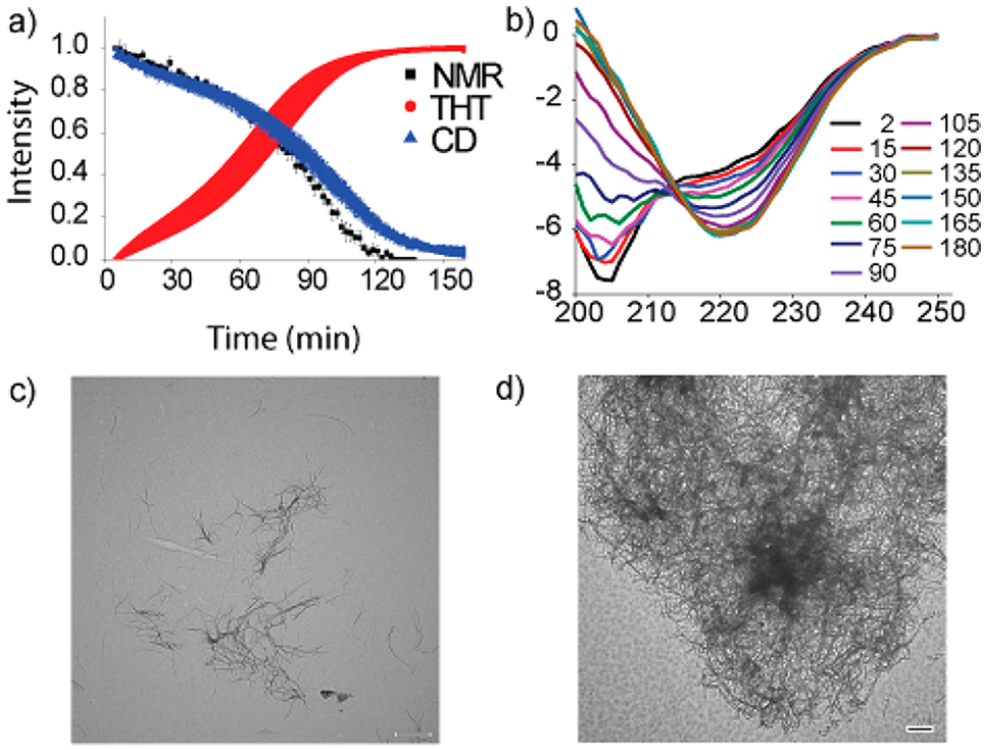

Figure 1.4. Comparison of the rates of monomer consumption and fiber formation. (a) Overlay of kinetic traces obtained via 19F NMR (black), ThT fluorescence (red), and CD (blue). (b) Time course CD trace of hIAPP aggregation. (c and d) TEM micrographs of hIAPP at an early time point and late time point, respectively. (Reprinted with permission, Copyright © 2012, American Chemical Society).

absence of detergents.[92] Several other techniques such as Electron Microscopy (EM, Figure 1.4) can detect the morphology of aggregates. Both transmission and scanning EM have been used comprehensively for low-resolution characterization and visualization of mature protein fibrils.[83] In particular, these techniques have proved invaluable for investigating membrane-bound oligomers,[93] which are inaccessible to most other techniques. However, these methods suffer from extensive surface contact between amyloid and sample support,[83] and have been shown to show a bias towards certain oligomers with a high affinity towards the surface.[91]

Real-time NMR is another promising alternative that fulfills most of the seven requirements listed above. NMR is moderately sensitive in modern spectrometers is non-perturbative, can easily track aggregation in the presence of inhibitors using labeled protein samples, detects a broad range of oligomers within certain size limits, and can yield rapid atomic-level structural details. While most of the spectra obtained from common solution NMR experiments is only observable for smaller oligomers, larger oligomers (up to 50 nm) [94] give rise to a characteristic spectra that is easily identified by pulse field gradient experiments.[95-97] A particular advantage of real-time NMR is the large amount of data encoded even in a 1D experiment and its ability to track the individual components of a heterogeneous sample (for example monomers, small oligomers, amyloid fibers) separately, at equilibrium, and non-perturbatively through differences in their chemical shift frequency or diffusion constants.[94,97] In this respect, real-time NMR can therefore provide a more clear understanding of the early stages of amyloid assembly and other amyloidogenic proteins. However, traditional NMR experiments on amyloids suffer from low sensitivity and low time resolution, severely limiting their applications to investigate a class of proteins that inherently have low solubility and display time-dependent aggregation. Despite these challenges, NMR has been able to track the

conformational changes that occur during aggregation in real-time for a limited number of amyloidogenic proteins.[98–100] In particular, the aggregation of hIAPP at pH 6 and 4 °C is slow enough that changes in ^{1}H or ^{15}N chemical shift values have provided residue specific information on the amyloid nucleation process. This study showed that the peaks for individual residues do not disappear uniformly. Instead, the N-terminal cross-peaks disappear before the C-terminal cross-peaks, implying that the formation of large aggregates that are invisible to NMR begins with the formation of N-terminal contacts.

Ion mobility-mass spectrometry (IM-MS) IM-MS is a dynamic tool, useful in the elucidation of protein mass and size. However, IM-MS data alone is often not enough to generate a complete model of amyloidogenic protein structure. In much of the literature, IM-MS results are presented in combination with other techniques such as NMR, X-ray crystallography, transmission electron microscopy (TEM), and gel electrophoresis. Useful information regarding the collisional cross section (CCS) paired with other biophysical data, these methods can provide a robust integrated framework from which to filter potential structural models for amyloid-forming peptides as well as small-molecule and metal ion interactions with amyloid peptides and proteins. In general, IM-MS can help study protein oligomerization and interaction pathways along with affording rich information about how small molecule compounds interact with and reorganize protein aggregates thus providing a method to screen compounds and study how these small molecules modify the distribution of amyloid species in the gas phase.

The ideal method for biophysical characterization would therefore be: (1) sensitive enough to pick up intermediate species that likely occur at low population; (2) not suffer from interference effects when used with small molecule inhibitors; (3) non-perturbative; (4) have a high distinguishing capability between different aggregates; (5) applicable to a broad range of

aggregates in terms of size and structure; (6) capable of providing an unbiased view of the total aggregates present, or at least an unbiased view of a subset that can be defined in a precise way; (7) yielding atomic-level structural details.

1.2 Dissertation objectives

It is evident that the events during the aggregation process of Aβ and hIAPP still have yet to be more clearly characterized. This does not even take into the factor the involvement of biological co-factors and biomolecules such as metal ions and lipid membranes. Though we now better understand how these systems are involved in protein assembly, there still remains a gap on how to target their specific interactions and mitigate their detrimental effects. The objectives of this thesis provide insights into methods on how to more clearly understand amyloid protein aggregation and provide methods on how to use small molecules and peptides to probe these interactions (Figure 1.5).

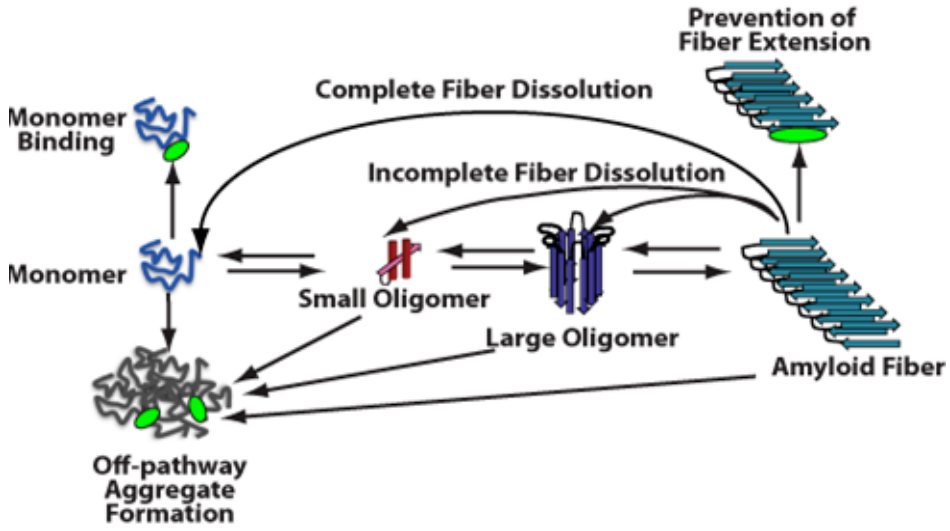

Figure 1.5. Possible influences of ligands on hIAPP aggregation**.** Schematic illustrating some of the possible mechanisms by which an inhibitor can affect aggregation: (A) Monomer stabilization; (B) Stabilization of off-pathway intermediates; (D and E) Dissolution of fibers either completely to the monomeric state (D) or incompletely to another oligomeric form (E); (F) Prevention of fiber extension. Note that this is not an exhaustive list of possible interactions.

Furthermore, the objectives of this work looks closely at key structural components that are required to investigate metal-Aβ interactions, membrane-hIAPP interactions, and amyloid self-assembly. In Chapter 2 the preparation, characterization, and metal–Aβ reactivity of two diphenylpropynone derivatives (**DPP1** and **DPP2**) composed of structural moieties for metal chelation and Aβ interaction is presented. These compounds were capable of interacting with both metal ions and Aβ species, as well as regulating metal-induced Aβ aggregation *in vitro*. Particularly, **DPP2**, which contains a dimethylamino group, exhibited greater reactivity with metal–Aβ species than **DPP1**, suggesting a structure-reactivity relationship. Overall, our studies present a new bifunctional scaffold that could be utilized to develop chemical reagents for investigating metal–Aβ species in AD. The deposition of aggregates of human islet amyloid polypeptide (hIAPP) has been correlated with the death of β-cells in type II diabetes mellitus. The actual molecular mechanism of cell death remains largely unknown; however, it has been postulated that the process of aggregation from monomeric hIAPP is closely involved. A possible cause of cellular toxicity may be through the disruption of structural integrity of the cell membrane by IAPP. In Chapter 3, the utility of a water-soluble curcumin derivative, **CurDAc**, is used to investigate the mitigation of hIAPP aggregation in the absence and presence of the lipid membrane, thus giving insights into how we can functionalize natural products to increase their effectiveness toward studying amyloid-lipid interactions. Lastly, molecular self-assembly, a phenomenon widely observed in nature, has been exploited through organic molecules, proteins, DNA and peptides to study complex biological systems. These self-assembly systems may also be used in understanding the molecular and structural biology which can inspire the design and synthesis of increasingly complex biomaterials. Specifically, use of these building blocks to

investigate protein folding and misfolding has been of particular value since it can provide tremendous insights into peptide aggregation related to a variety of protein misfolding diseases, or amyloid diseases (e.g. Alzheimer's disease, Parkinson's disease, type-II diabetes). In Chapter 4 the self-assembly of **TK9**, a 9 residue peptide of the extra membrane C-terminal tail of the SARS Corona virus envelope is characterized through biophysical, spectroscopic and simulated studies, and it was confirmed that the structure of these peptides influence their aggregation propensity, hence, mimicking amyloid proteins. **TK9**, which forms a beta-sheet rich fibril, contains a key sequence motif that may be critical for β-sheet formation, thus making it an interesting system to study amyloid fibrillation and inhibition through self-recognition.

1.3 References

1. Brender, J. R.; Salamekh, S.; Ramamoorthy, A. *Acc. Chem. Res.* **2012**, *45*, 454–462.

2. Lin, C. Y.; Gurlo, T.; Kayed, R.; Butler, A. E.; Haataja, L.; Glabe, C. G.; Butler, P. C. *Diabetes* **2007**, *56*, 1324–1332.

3. de Koning, E. J.; Morris, E. R.; Hofhuis, F. M.; Posthuma, G.; Höppener, J. W.; Morris, J. F.; Capel, P. J.; Clark, A.; Verbeek, J. S. *Proc. Natl. Acad. Sci. U.S.A* **1994**, *91*, 8467–8471.

4. Knight J. D.; Hebda, J. A.; Miranker, A. D. *Biochemistry* **2006**, *45*, 9496–9508.

5. Wetzel, R.; Shivaprasad, S.; Williams, A. D. *Biochemistry* **2007**, *46*, 1–10.

6. Jayasinghe, S. A.; Langen, R. *Biochemistry* **2005**, *44*, 12113–12119.

7. Kayed, R.; Head, E.; Thompson, J. L.; McIntire, T. M.; Milton, S. C.; Cotman, C. W.; Glabe, C. G. *Science* **2003**, *300*, 486–489.

8. Glabe, C. G. *J. Biol. Chem.* **2008**, *283*, 29639–29643.

9. Khemtémourian, L.; Killian, J. A.; Höppener, J. W.; Engel, M. F. M. *Exp. Diabetes Res.* **2008**, Article ID: 421287*,* 1–9.

10. Jakob-Roetne R.; Jacobsen H. *Angew. Chem. Int. Ed.* **2009**, *48,* 3030-3059.

11. Rauk A. *Chem. Soc. Rev.* **2009**, *38*, 2698-2715.

12. Hardy J. A.; Higgins G. A. *Science* **1992**, *256*, 184-185.

13. Scott L. E.; Orvig C. *Chem. Rev.* **2009**, *109*, 4885-4910.

14. DeToma A. S.; Salamekh S.; Ramamoorthy A.; Lim M. H. *Chem. Soc. Rev. 2012*, DOI: 10.1039/c1cs15112f.

15. Haass C.; Selkoe D. J. *Nat. Rev. Mol. Cell. Biol.* **2007**, *8*, 101-112.

16. Westermark, P.; Andersson, A.; Westermark, G. T. *Physiol. Rev.* **2011**, *91*, 795-826.

17. Hoppener, J. W. M., Ahren, B.; Lips, C. J. M. *N. Engl. J. Med.* **2000**, *343*, 411-419.

18. Huang, C. J., Haataja, L., Gurlo, T., Butler, A. E., Wu, X. J., Soeller, W. C.; Butler, P. C. *Am. J. Physiol.* **2007**, *293*, E1656-E1662.

19. Matveyenko, A. V.; Butler, P. C. *ILAR J.* **2006**, *47*, 225-233.

20. Matveyenko, A. V.; Butler, P. C. *Diabetes* **2006**, *55*, 2106-2114.

21. Luca, S.; Yau, W. M.; Leapman, R.; Tycko, R. Biochemistry, 2007, 46, 13505-13522.

22. Lippard S. J.; Berg J. M. *Principles of Bioinorganic Chemistry*. University Science Books; 1994.

23. Bertini I.; Gray H. B.; Stiefel E. I.; Valentine J. S. *Biological Inorganic Chemistry: Structure and Reactivity*. University Science Books; 2007.

24. Burdette S. C.; Lippard S. J.; *Proc. Natl. Acad Sci.* **2003**, *100*, 3605-3610.

25. Que E. L.; Domaille D. W.; Chang C. J. *Chem. Rev.* **2008**, *108*, 1517-1549.

26. Bush A. I.; Tanzi R. E. *Neurotherapeutics* **2008**, *5*, 421-432.

27. Frederickson C. J.; Koh J-Y; Bush A. I. *Nat. Rev. Neurosci.* **2005**, *6*, 449-462.

28. Faller P. *ChemBioChem* **2009**, *10*, 2837-2845.

29. Faller P.; Hureau C. *Dalton. Trans.* **2009**, *7*, 1080-1094.

30. Gaggelli E.; Kozlowski H.; Valensin D.; Valensin G. *Chem. Rev.* **2006**, *106*, 1995-2044.

31. Drew S. C, Barnham K. J. *Acc. Chem. Res.* **2011**, DOI: 10.1021/ar200014u.

32. Karr J. W.; Szalai V. A. *Biochemistry* **2008**, *47*, 5006-5016.

33. Dorlett P.; Gamberelli S.; Faller P.; Hureau C. *Angew. Chem. Int. Ed.* **2009**, *48*, 9273-9276.

34. Shearer J.; Szalai V. A. *J. Am. Chem. Soc.* **2008**, *130*, 17826-17835.

35. Himes R. A.; Park G. Y.; Siluvai G. S.; Blackburn N. J.; Karlin K. D. *Angew. Chem. Int. Ed.* **2008**, *47*, 9084-9087.

36. Shearer J.; Callan P. E.; Tran T.; Szalai V. A. *Chem. Commun.* **2010**, *46*, 9137-9139.

37. Feaga H. A; Maduka R. C.; Foster M. N.; Szalai V. A. *Inorg. Chem* **2011**, *50*,1614-1618.

38. Bousejra-ElGarah F.; Bigani C.; Coppel Y.; Faller P.; Hureau C. *Inorg. Chem.* **2011**, DOI: 10.1021/ic201233b.

39. Zatta P.; Drago D.; Bolognin S.; Sensi S. L. *Trends Pharmacol. Sci.* **2009**, *30*, 346-355.

40. Hureau C.; Faller P. *Biochimie* **2009**, *91*, 1212-1217.

41. Maynard C. J.; Bush A. I.; Masters C. L.; Cappai R.; Li Q-X. *Int. J. Exp. Pathol.* **2005**, *86*, 147-159.

42. Noy D.; Solomonov I.; Sinkevich O.; Arad T.; Kjaer K.; Sagi I. *J. Am. Chem. Soc.* **2008**, *130*, 1376-1383.

43. Chen W.-T.; Liao Y.-H.; Yu H.-M.; Cheng I. H.; Chen Y.-R. *J. Biol. Chem.* **2011**, *286*, 9646-9656.

44. Singh S, Trikha S, Bhowmick DC, Sarkar AA, Jeremic AM. *Adv. Exp. Med. Biol.* **2015,** *855*, 95-116.

45. Wakabayashi M, Matsuzaki K. *FEBS Lett*. **2009,** *583*, 2854-8.

46. Knight, J. D. & Miranker, A. D. *J. Mol. Biol.* **2004**, *341*, 1175-1187.

47. Jayasinghe, S. A. & Langen, R. *Biochemistry* **2005**, *44*, 12113-12119.

48. Pithadia A. S.; Lim M. H. *Curr. Opin. Chem. Biol*. **2012**, *16*, 67-73.

49. Huang, C. J.; Lin, C. Y.; Haataja, L.; Gurlo, T.; Butler, A. E.; Rizza, R. A.; Butler, P. C. *Diabetes* **2007**, *56*, 2016-2027.

50. Sjolander, J.; Westermark, G. T.; Renstrom, E.; Blom, A. M. *J. Biol. Chem.* **2012**, *287*, 10824-10833.

51. Masters, S. L.; Dunne, A.; Subramanian, S. L.; Hull, R. L.; Tannahill, G. M.; Sharp, F. A.; Becker, C.; Franchi, L.; Yoshihara, E.; Chen, Z.; Mullooly, N.; Mielke, L. A.; Harris, J.; Coll, R. C.; Mills, K. H. G.; Mok, K. H.; Newsholme, P.; Nunez, G.; Yodoi, J.; Kahn, S. E.; Lavelle, E. C.; O'Neill, L. A. J. *Nat. Immunol.* **2010**, *11,* 897-904.

52. Haataja, L.; Gurlo, T.; Huang, C. J.; Butler, P. C. *Endocr. Rev.* **2008**, *29*, 302-316.

53. Hebda, J. A.; Miranker, A. D. *Annu. Rev. Biophys. Biomol. Struct.* **2009**, *38*, 125-52.

54. Lal, R.; Lin, H.; Quist, A. P. *Biochim. Biophys. Acta* **2007**, *1768*, 1966-1975.

55. Kagan, B. L.; Thundimadathil, J. *Proteins* **2010**, *677*, 150-167.

56. Demuro, A.; Parker, I.; Stutzmann, G. E. *J. Biol. Chem.* **2010**, *285*, 12463-12468.

57. Hoshi, M.; Sato, M.; Matsumoto, S.; Noguchi, A.; Yasutake, K.; Yoshida, N.; Sato, K. *Proc. Natl. Acad. Sci. U. S. A.* **2003**, *100*, 6370-6375.

58. Solomonov, I.; Korkotian, E.; Born, B.; Feldman, Y.; Bitler, A.; Rahimi, F.; Li, H.; Bitan, G.; Sagi, I. *J. Biol. Chem.* **2012**, *287*, 20555-64.

59. Janson, J.; Ashley, R. H.; Harrison, D.; McIntyre, S.; Butler, P. C. *Diabetes* **1999**, *48*, 491-498.

60. Green, J. D.; Kreplak, L.; Goldsbury, C.; Blatter, X. L.; Stolz, M.; Cooper, G. S.; Seelig, A.; Kist-Ler, J.; Aebi, U. *J. Mol. Biol.* **2004**, *342*, 877-887.

61. Ikeda, K.; Yamaguchi, T.; Fukunaga, S.; Hoshino, M.; Matsuzaki, K. *Biochemistry* **2011**, *50*, 6433-6440.

62. Williams, T. L.; Johnson, B. R. G.; Urbanc, B.; Jenkins, A. T. A.; Connell, S. D. A. & Serpell, L. C. *Biochem. J.* **2011**, *439*, 67-77.

63. Hureau C.; Sasaki I.; Gras E.; Faller, P. *ChemBioChem* **2010**, *11*, 950-953.

64. Braymer J. J; DeToma A. S.; Choi J.-S.; Ko K. S.; Lim M. H. *Int. J. Alzheimers Dis.* **2011**, 623051.

65. Perez L. R.; Franz K. J. *Dalton. Trans.* **2010**, *39*, 2177-2187.

66. Cherny, R. A.; Atwood, C. S.; Xilinas, M. E.; Gray, D. N.; Jones, W. D.; McLean, C. A.; Barnham, K. J.; Volitakis, I.; Fraser, F. W.; Kim, Y.-S.; Huang X. D.; *et al*: *Neuron* **2001**, *30*, 665-676.

67. Adlard, P. A.; Cherny, R. A.; Finkelstein, D. I.; Gautier, E.; Robb, E.; Cortes, M.; Volitakis I.; Liu, X.; Smith, J. P; Perez, K.; Laughton, K.; *et al*: *Neuron* **2008**, *59*, 43-55.

68. Kung, H. F.; Lee, C.-W.; Zhuang, Z.-P.; Kung, M.-P.; Hou, C.; Plössl, K. *J. Am. Chem. Soc.* **2001**, *123*, 12740-12741.

69. Choi, J.-.S; Braymer, J. J.; Nanga, R. P. R.; Ramamoorthy, A.; Lim, M. H. *Proc. Natl. Acad. Sci. U.S.A.* **2010**, *107*, 21990-21995.

70. T. Beghyn, R. Deprez-Poulain, N. Willand, B. Folleas and B. Deprez, *Chem. Biol. Drug Design*, vol. 72, no. 1, pp. 3-15, 2008.

71. B. J. Blanchard, A. Chen, L. M. Rozeboom, K. A. Stafford, P. Weigele and V. M. Ingram, *Proc. Natl. Acad. Sci. U.S.A.*, vol. 101, no. 40, pp. 14326-14332, 2004.

72. J. H. Jang and Y. J. Surh, *Free Rad. Biol. Med.*, vol. 34, no. 8, pp. 1100-1110, 2003.

73. S. Chakrabarti, M. Sinha, I. G. Thakurta, P. Banerjee and M. Chattopadhyay, *Curr. Med. Chem.*, vol. 20, no. 37, pp. 4648-4664, 2013.

74. N. Apetz, G. Munch, S. Govindaraghavan and E. Gyengesi, *CNS Neurol. Disord. - Drug Targets*, vol. 13, no. 7, pp. 1175-1191, 2014.

75. R. Mishra, D. Sellin, D. Radovan, A. Gohlke and R. Winter, *ChemBioChem*, vol. 10, pp. 445-449, 2009.

76. F. Evers, C. Jeworrek, S. Tiemeyer, K. Weise, D. Sellin, M. Paulus, B. Struth, M. Tolan and R. Winter. *J. Am. Chem. Soc.*, vol. 131, no. 27, pp. 9516-9521, 2009.

77. N. Arispe, J. Diaz, S. R. Durell, Y. Shafrir and H. R. Guy, *Biochemistry*, vol. 49, no. 36, pp. 7847-7853, 2010.

78. N. Arispe, J. C. Diaz and O. Simakova, *Biochim. Biophys. Acta.* vol. 1768, no. 8, pp. 1952-1965, 2007.

79. J. C. Diaz, O. Simakova, K. A. Jacobson, N. Arispe and H. B. Pollard *Proc. Natl. Acad. Sci. U.S.A.*, vol. 106, no. 9, pp. 3348-3353, 2009.

80. J. Fantini, C. Di Scala, N. Yahi, J. D. Troadec, K. Sadelli, H. Chahinian and N. Garmy, *ACS Chem. Neurosci.*, vol. 5, no. 3, pp. 216-224, 2014.

81. Y. Porat, A. Abramowitz and E. Gazit, *Chem. Biol. Drug Design.*, vol. 67, pp. 27-37, 2006.

82. M. Stefani and S. Rigacci, *Int. J. Mol. Sci.*, vol. 14, pp. 12411-12457, 2013.

83 Langkilde, A. E.; Vestergaard, B. *FEBS Lett.* **2009**, *583*, 2600–2609.

84 Maezawa, I.; Hong, H.-S.; Liu, R.; Wu, C.-Y.; Cheng, R. H.; Kung, M.-P.; Kung, H. F.; Lam, K. S.; Oddo, S.; LaFerla, F. M.; Jin, L.-W. **2008**, *104*, 457–468.

85 Jha, S.; Snell, J. M.; Sheftic, S. R.; Patil, S. M.; Daniels, S. B.; Kolling, F. W.; Alexandrescu, A. T. *Biochemistry* **2014**, DOI: 10.1021/bi401164k.

86 Easterhoff, D.; DiMaio, J. T. M.; Liyanage, W.; Lo, C.-W.; Bae, W.; Doran, T. M.; Smrcka, A.; Nilsson, B. L.; Dewhurst, S. *Bioorg. Med. Chem. Lett.* **2013**, *23*, 5199–5202.

87 Hudson, S. A.; Ecroyd, H.; Kee, T. W.; Carver, J. A. *FEBS J.* **2009**, *276*, 5960–5972.

88 Meng, F.; Marek, P.; Potter, K. J.; Verchere, C. B.; Raleigh, D. P. *Biochemistry* **2008**, *47*, 6016–6024.

89 Kayed, R.; Bernhagen, J.; Greenfield, N.; Sweimeh, K.; Brunner, H.; Voelter, W.; Kapurniotu, A. *J. Mol. Biol.* **1999**, *287*, 781–796.

90 Li, H.; Rahimi, F.; Sinha, S.; Maiti, P.; Bitan, G.. **2009**; Published Online, DOI: 10.1002/9780470027318.a9038.

91 Hepler, R. W.; Grimm, K. M.; Nahas, D. D.; Breese, R.; Dodson, E. C.; Acton, P.; Keller, P. M.; Yeager, M.; Wang, H.; Shughrue, P.; Kinney, G.; Joyce, J. G. *Biochemistry* **2006**, *45*, 15157–15167.

92. Pan, J.; Han, J.; Borchers, C. H.; Konermann, L. *Biochemistry* **2012**, *51*, 3694–3703.

93. Connelly, L.; Jang, H.; Arce, F. T.; Capone, R.; Kotler, S. A.; Ramachandran, S.; Kagan, B. L.; Nussinov, R.; Lal, R. *J. Phys. Chem. B*. **2012**, *116*, 1728-1735.

94. Soong, R.; Brender, J. R.; Macdonald, P. M.; Ramamoorthy, A. *J. Am. Chem. Soc.* **2009**, *131*, 7079–7085.

95. Krishnamoorthy, J.; Brender, J. R.; Vivekanandan, S.; Jahr, N.; Ramamoorthy, A. *J. Phys. Chem. B* **2012**, *116*, 13618–13623.

96. Narayanan, S.; Reif, B. *Biochemistry* **2005**, *44*, 1444–1452.

97. Huang, R.; Vivekanandan, S.; Brender, J. R.; Abe, Y.; Naito, A.; Ramamoorthy, A. *J. Mol. Biol.* **2012**, *416*, 108–120.

98. Corazza, A.; Rennella, E.; Schanda, P.; Mimmi, M. C.; Cutuil, T.; Raimondi, S.; Giorgetti, S.; Fogolari, F.; Viglino, P.; Frydman, L.; et al. *J. Biol. Chem.* **2010**, *285*, 5827–5835.

99. Mishra, R.; Geyer, M.; Winter, R. *ChemBioChem* **2009**, *10*, 1769–1772.

100. Kanaori, K.; Nosaka, A. Y. *Biochemistry* **1995**, *34*, 12138–12143.

Chapter 2: Reactivity of Diphenylpropynone Derviatives Toward Metal-Associated Amyloid-β Species

This chapter was adapted from the following publication:

> **Pithadia, A. S.**; Kochi, A.; Soper, M. T.; Beck, M. W.; Liu, Y.; Lee, S.; DeToma, A. S.; Ruotolo, B. T.; Lim, M. H. *Inorg. Chem.* **2012**, 51, 12959. [1]

2.1. Introduction

Alzheimer's disease (AD) is a devastating and fatal neurodegenerative disease that affects over 5 million people in the United States.[1,2] A pathological hallmark of the diseased brain is an accumulation of misfolded amyloid-β (Aβ) peptides and its aggregated forms (*e.g.,* oligomers, protofibrils, fibrils).[2-6] Monomeric Aβ species result from the proteolytic cleavage of the transmembrane protein, amyloid precursor protein (APP) which can further aggregate to produce oligomers, protofibrils, and eventually fibrils.[2-5,7,8] It is still not completely understood which conformation of Aβ is associated with AD neuropathogensis; however, recent evidence has proposed that soluble oligomers might be the toxic species due to their ability to interrupt neurotransmission.[4,5,9]

In addition, elevated concentrations of transition metals, such as Cu, Zn, and Fe, have been observed within the deposits of Aβ aggregates.[2,7,10-15] These metals serve important functions in the body, especially in the brain, and a misregulation may lead to adverse consequences.[2,7,8] The possible relationship between metal-associated Aβ species (metal–Aβ species) and neurotoxicity has been suggested based on observations that metal ions facilitate Aβ aggregation as well as enhance oxidative stress caused by reactive oxygen species (ROS).[2,4,5,7,8,12-21] It has not been, however, clearly revealed if and how metal–Aβ species are linked to AD pathology.

[I] ASP – synthesis, metal binding, speciation; AK, YL – gel assays; MTS – mass spec; MWB – docking; ASD – revising

To gain a better understanding of this connection, previous efforts in metal chelation therapy were taken by utilizing metal chelators such as clioquinol (CQ) as tools to disturb the metal–Aβ interaction.[2,4,5,7,8,19,22] However, due to the lack of specificity of these metal chelators for Aβ, recent advancements in the development of chemical reagents to specifically target metal–Aβ species and modulate their interaction and reactivity have been made.[2,7,8,21,23-33] Among them, rationally-designed small molecules with metal chelation and Aβ interaction properties (defined as bifunctionality) have been constructed. Some of the compounds have been fashioned based on the incorporation approach (Figure 2.1), where a metal chelation site is directly inserted into the structure of a known Aβ imaging agent with minimal structural modifications, along with consideration of criteria for possible brain uptake.[8,21,23-26,28-33] They have been able to control the interactions and reactivity of metal–Aβ species *in vitro* and/or in living cells, suggesting that the incorporation approach (Figure 2.1) could be considered as a promising design strategy to develop suitable chemical reagents for studying the involvement of metal–Aβ species in AD. Herein, we report the design, preparation, and characterization of a new class of bifunctional small molecules (**DPP1** and **DPP2**, Figure 2.1) that were developed for targeting and regulating metal–Aβ species utilizing a diphenylpropynone framework. In addition, their reactivity with metal–Aβ species *in vitro* was investigated and described. Our recent findings suggest that the diphenylpropynone framework may be beneficial for targeting metal–Aβ species and altering their reactivity, as well as minor structural features such as the dimethylamino functionality may be responsible for a refined interaction with Aβ, thus potentially enhancing reactivity with metal–Aβ species.

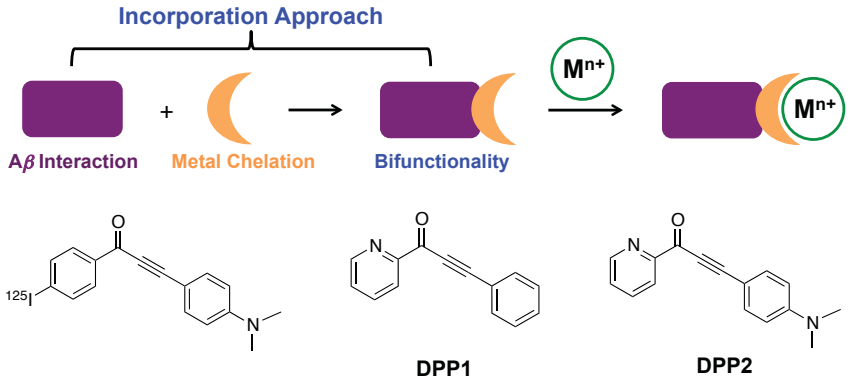

Figure 2.1. Incorporation approach (top) and structures of small molecules (bottom). Left to right: 3-(4-(dimethylamino)-phenyl)-1-(4-iodophenyl)-2-propyn-1-one; **DPP1** = 3-phenyl-1-(pyridin-2-yl)-2-propyn-1-one; **DPP2** = 3-(4-(dimethylami-no)phenyl)-1-(pyridin-2-yl)-2-propyn-1-one.

Materials and Procedures

All reagents were purchased from commercial suppliers and used as received unless otherwise stated. The compound, 3-phenyl-1-(pyridin-2-yl)prop-2-yn-1-one (**DPP1**) was prepared following previously reported methods.[34-36] A$\beta_{1\text{-}40}$ (DAEFRHDSGYEVHHQKLVFFAEDVGSNKGAIIG-LMVGGVV) was purchased from AnaSpec (Fremont, CA). An Agilent 8453 UV-Visible (UV-Vis) spectrophotometer was used to measure the optical spectra. Transmission electron microscopy (TEM) images were recorded with a Philips CM-100 transmission electron microscope. A SpectraMax M5 microplate reader (Molecular Devices, Sunnyvale, CA) was employed for the measurement of absorbance for 3-(4,5-dimethylthiazol-2-yl)-2,5-diphenyltetrazolium bromide (MTT) and PAMPA-BBB assays. NMR spectra of small molecules and for Zn^{2+} binding studies were obtained by a Varian 400 MHz NMR spectrometer. Mass spectrometric measurements for compounds were made using a Micromass LCT Electrospray Time-of-Flight mass spectrometer. Mass spectrometric studies for investigating the interaction of **DPP1** and **DPP2** with the peptide were carried out on a Waters Synapt G2 ion-mobility mass spectrometer (Milford, MA).

Preparation of 3-(4-(dimethylamino)phenyl)-1-(pyridin-2-yl)-2-propyn-1-one (DPP2). **DPP2** was synthesized by slight modifications to a previously reported procedure.[36] To a solution of 4'-dimethylaminophenyl acetylene (0.42 g, 2.9 mmol) in dry tetrahydrofuran (THF, 5 mL) was added *n*-butyllithium (0.72 mL, 2.9 mmol, 2.5 M solution in hexanes) dropwise by a syringe over 5 min at -40 °C. The reaction mixture was allowed to stir at -40 °C for 10 min and then warmed to -15 °C. After 30 min, the mixture was cooled to -78 °C (dry ice/acetone) and a

solution of Weinreb's amide (0.40 g, 2.4 mmol in 9 mL of dry THF) was introduced through a syringe. The reaction mixture was allowed to react at -78 °C for 10 min and then warmed to room temperature and followed by 1 h stirring. The reaction was quenched by adding saturated aqueous $NaHCO_3$ (2 mL), diluted with EtOAc (10 mL), and washed with brine (2 x 25 mL). The aqueous layer was extracted with EtOAc (2 x 15 mL), and the combined organic solutions were dried over $MgSO_4$ and filtered, followed by removal of the solvent *in vacuo*. The crude product was purified by silica gel chromatography (CH_2Cl_2 : EtOAc = 9 : 1) to yield an orange product (202 mg, 0.81 mmol, 28%). ^{1}H NMR (400 MHz, $CDCl_3$)/δ (ppm): 8.77 (d, J = 4.8 Hz, 1 H), 8.14 (d, J = 7.6 Hz, 1 H), 7.82 (td, J = 7.6, 1.6 Hz, 1 H), 7.57 (d, J = 8.4 Hz, 2 H), 7.44 (m, 1 H), 6.59 (d, J = 8.4 Hz, 2 H), 2.98 (s, 6 H). ^{13}C NMR (100 MHz, $CDCl_3$)/δ (ppm): 177.6, 153.7, 151.8, 149.7, 136.8, 135.6, 126.9, 123.3, 111.4, 105.5, 100.2, 89.3, 39.9. HRMS: Calcd for $[M+H]^+$, 251.1179; Found, 251.1176.

Parallel Artificial Membrane Permeability Assay (PAMPA). PAMPA-BBB experiments were carried out using the PAMPA Explorer kit (*p*ION Inc.) with modification to previously reported protocols.[30,37-39] Each stock solution was diluted with pH 7.4 Prisma HT buffer (*p*ION) to a final concentration of 25 μM (1% v/v final DMSO concentration) and 200 μL were added to the wells of the donor plate (number of replicates = 12). BBB-1 lipid formulation (5 μL, *p*ION) was used to coat the polyvinylidene fluoride (PVDF, 0.45 *m*M) filter membrane on the acceptor plate and brain sink buffer (BSB, 200 μL, *p*ION) was added to each well of the acceptor plate. The acceptor plate was placed on top of the donor plate forming a "sandwich." The sandwich was incubated for 4 h at ambient temperature without stirring. UV-Vis spectra of the solutions in the reference, acceptor, and donor plates were measured using a microplate reader. The PAMPA Explorer software v. 3.5 (*p*ION) was used to calculate the $-\log P_e$ for each

compound. CNS+/− designations were assigned by comparison to compounds that were identified in previous reports.[37-39]

Determination of Solution Speciation for DPP1, DPP2, and the Cu^{2+}–DPP2 Complex. The pK_a values for **DPP1** and **DPP2** were determined by UV-Vis variable-pH titrations based on a previously reported procedure.[30] To establish the pK_a values, a solution (100 mM NaCl, 10 mM NaOH, pH 12) of **DPP1** (40 μM) or **DPP2** (20 μM) was titrated with small aliquots of HCl. At least 30 spectra were recorded in the range of pH 2 - 10. Similarly, a solution containing **DPP2** (20 μM) and $CuCl_2$ in a ratio of 2:1 was titrated with small additions of HCl and at least 30 spectra were recorded over the range of pH 2 - 7. The acidity and stability constants were calculated by using the HypSpec program (Protonic Software, UK).[40] Speciation diagrams for **DPP1**, **DPP2**, and Cu^{2+}–**DPP2** complexes were modeled using the HySS2009 program (Protonic Software).[41]

Metal Binding Studies. The interaction of **DPP1** and **DPP2** with Cu^{2+} and Zn^{2+} was determined by UV-Vis and ^{1}H NMR spectroscopy, respectively, based on previously reported procedures.[30,42] A solution of ligand (20 μM in EtOH) was prepared, treated with 1 to 20 equiv of $CuCl_2$, and incubated at room temperature for 2.5 h (for **DPP1**) or 5 min (for **DPP2**). The optical spectra of the resulting solutions were measured by UV-Vis. The interaction of **DPP1** or **DPP2** with $ZnCl_2$ was observed by ^{1}H NMR. $ZnCl_2$ (1 equiv) was added to a solution of **DPP1** or **DPP2** (4 mM) in CD_3CN. The metal selectivity of both compounds was investigated by measuring the optical changes upon addition of 1 equiv of $CuCl_2$ to a solution of ligand (**DPP1** = 40 μM; **DPP2** = 20 μM in EtOH) containing 1 equiv or 25 equiv of a divalent metal chloride salt ($MgCl_2$, $CaCl_2$, $MnCl_2$, $FeCl_2$, $CoCl_2$, $NiCl_2$, or $ZnCl_2$). The Fe^{2+} samples were prepared anaerobically (all solutions were purged with N_2). Quantification of the metal

selectivity was calculated by comparing and normalizing the absorption values of metal-ligand complexes at λ = 360 nm (for **DPP1**) or 580 nm (for **DPP2**) to the absorption at this wavelength before and after the addition of $CuCl_2$ (A_M/A_{Cu}). Cu^{2+} binding of **DPP2** in the presence of Aβ was examined by UV-Vis. Aβ (25 μM) was treated with $CuCl_2$ (25 μM) in 20 mM HEPES (2-[4-(2-hydroxyethyl)piperazin-1-yl]ethanesulfonic acid), pH 6.6, 150 mM NaCl for 2 min at room temperature. **DPP2** (50 μM) was added to the resulting solution, followed by 4 h incubation. For comparison, the optical spectra of **DPP2** (50 μM) were measured in the absence and presence of $CuCl_2$ (25 μM; 4 h incubation) without Aβ at pH 6.6.

Aβ Interaction of DPP1 and DPP2 by Mass Spectrometry. The interaction of **DPP1** or **DPP2** with $A\beta_{1\text{-}40}$ was investigated by nano-electrospray ionization-mass spectrometry (nESI-MS) that was carried out on a Synapt G2 quadrupole-ion mobility-mass spectrometry system. Samples were prepared by mixing stock solutions of **DPP1** or **DPP2** (prepared in DMSO) and $A\beta_{1\text{–}40}$ (dissolved in 100 mM ammonium acetate, pH 6.8) to generate desired final concentrations of the peptide and the compound. Mixtures were incubated on ice or at room temperature for 2 or 4 h, respectively and then analyzed. To produce protein complex ions, an aliquot of the sample (*ca.* 5 μL) was sprayed from the nESI emitter using a capillary voltage of 1.4 kV, with the source operating in positive ion mode and the sample cone operated at 50 V. In order to normalize nESI-MS data for non-specific and electrospray artifact interactions which could occur at high concentrations, data were acquired for Aβ samples containing thioflavin-T (ThT), a compound known to have no affinity for soluble forms of the Aβ peptide, under identical concentration conditions as our **DPP1** and **DPP2** experiments. Any ThT binding observed was assumed to be due to either non-specific binding or the electrospray process, and subtracted from the intensities of the **DPP1** and **DPP2** interactions observed.[43] This procedure was performed over a broad

range of concentrations. The mass spectra were acquired with the following settings and tuned to avoid ion activation and to preserve non-covalent protein–ligand complexes:[44] backing pressure, 7.3 mbar; IMS pressure reading, 3.09 mbar; ToF analyzer pressure, 1.14×10^{-6} mbar.

Docking Studies. Flexible ligand docking studies using AutoDock Vina[45] for **DPP1** and **DPP2** were conducted against the A$\beta_{1\text{-}40}$ monomer from the previously determined aqueous solution NMR structure (PDB 2LFM).[46] Ten conformations were selected from 20 conformations within the PDB file (1, 3, 5, 8, 10, 12, 13, 16, 17, and 20). The MMFF94 energy minimization in ChemBio3D Ultra 11.0 was used to optimize the structures of the ligands for the docking studies. The structural files of **DPP1**, **DPP2**, and the peptide were generated by AutoDock Tools and imported into PyRx, which was used to run AutoDock Vina. The search space dimensions were set to contain the entire peptide. The exhaustiveness for the docking runs was set at 1024. Docked poses of the ligands were visualized with Aβ using Pymol.

Amyloid-β (Aβ) Peptide Experiments. A$\beta_{1\text{-}40}$ was used in all Aβ experiments. A$\beta_{1\text{-}40}$ peptide (1 mg) was dissolved with ammonium hydroxide (NH_4OH, 1% v/v, aq), aliquoted, lyophilized, and stored at -80 °C. A stock solution (*ca*. 200 μM) was prepared by redissolving Aβ with NH_4OH (1% v/v, aq, 10 μL) followed by dilution with ddH_2O. All Aβ solutions were prepared following previously reported procedures.[29,30] The buffered solutions (20 μM HEPES, pH 6.6 (for Cu^{2+} samples) or pH 7.4 (for metal-free and Zn^{2+} samples), 150 μM NaCl) were used for both inhibition and disaggregation studies. For the inhibition experiment, Aβ (25 μM) was first treated with a metal chloride salt ($CuCl_2$ or $ZnCl_2$, 25 μM) for 2 min followed by addition of a compound (**DPP1** or **DPP2**, 50 μM in DMSO, 1% v/v final DMSO concentration). The resulting samples were incubated at 37 °C for 4, 8, or 24 h with constant agitation. For the disaggregation experiment, Aβ and a metal chloride salt ($CuCl_2$ or $ZnCl_2$) were initially incubated at 37 °C for

24 h with steady agitation. The compound was added afterwards followed by additional 4, 8, or 24 h incubation at 37 °C with constant agitation.

Native Gel Electrophoresis/Sodium Dodecyl Sulfate-Polyacrylamide Gel Electrophoresis (SDS-PAGE) with Western Blotting. The Aβ peptide experiments (as described above) were analyzed by both native gel electrophoresis and SDS-PAGE with Western blotting using an anti-Aβ antibody (6E10).[29,30] Each sample containing 25 μM Aβ (10 μL) was separated using either a 10 - 20% gradient Tris-tricine gel (Invitrogen) or SDS gel (4% stacking gel; 10% resolving gel; non-reducing conditions). The gel was transferred to a nitrocellulose membrane and blocked overnight with bovine serum albumin (BSA, Sigma, 3% w/v) dissolved in Tris-buffered saline (TBS, Fisher) containing 0.1% Tween-20 (TBS-T, Sigma). The membrane was treated with 6E10 (1:2,000; 2% BSA in TBS-T, Covance, Princeton, NJ) for 4 h at room temperature. The membrane was probed with a horseradish peroxidase-conjugated goat anti-mouse secondary antibody (1:5,000; Cayman Chemical, Ann Arbor, MI) in 2% BSA in TBS-T solution for 1 h at room temperature. The protein bands were visualized using the Thermo Scientific Supersignal West Pico Chemiluminescent Subtrate.

Transmission Electron Microscopy (TEM). Samples for TEM were prepared following a previously reported method.[29,30,47] Glow-discharged grids (Formar/Carbon 300-mesh, Electron Microscopy Sciences, Hatfield, PA) were treated with samples from either inhibition or disaggregation experiments (5 μL) for 2 min at room temperature. Excess sample was removed with filter paper and washed with ddH_2O five times. Each grid was stained with uranyl acetate (1% w/v, ddH_2O, 5 μL) for 1 min. Uranyl acetate was blotted off and grids were dried for 15 min at room temperature. Images of samples were taken by a Philips CM-100 transmission electron microscope (80 kV, 25,000x magnification).

Cytotoxicity (MTT Assay). The murine neuro-2a (N2a) neuroblastoma cell line was purchased from the American Type Culture Collection (ATCC, Manassas, VA). The cell line was maintained in media containing 45% Dulbecco's modified Eagle's medium (DMEM) and 50% OPTI-MEM (GIBCO), supplemented with 5% fetal bovine serum (FBS, Sigma), 2 mM glutamine, 100 U/ml penicillin, and 100 mg/ml streptomycin (GIBCO). The cells were grown and maintained at 37 °C in a humidified atmosphere with 5% CO_2. Cell viability upon treatment of compounds was determined using the MTT assay (Sigma Aldrich). N2a cells were seeded in a 96 well plate (15,000 cells in 100 μL per well) and treated with various concentrations of **DPP1** and **DPP2** (2.5 - 50 μM, final 1% v/v DMSO). After 24 h incubation at 37 °C, 25 μL MTT (5 mg/mL in phosphate buffered saline, PBS, GIBCO, pH 7.4) was added to each well and the plates were incubated for 4 h at 37 °C. Formazan produced by the cells was dissolved by addition of a solution (100 μL) containing *N,N*-dimethylformamide (DMF, 50% v/v, aq, pH 4.5) and sodium dodecyl sulfate (SDS, 20% w/v) overnight at room temperature. A microplate reader was used to measure the absorbance (A_{600}).

Results and Discussion

Design Consideration, Preparation, and Characterization of Diphenylpropynone Derivatives for Targeting and Modulating Metal–Aβ Species.

A triple bond in the diphenylpropynone scaffold, which has been reported as an Aβ imaging probe (Figure 2.1), was shown to have high binding affinity for the β-sheet secondary structure of Aβ fibrils due to its rigidity.[48] Based on the incorporation approach, a nitrogen donor atom was installed into this framework to generate a metal chelation site with an oxygen donor atom of the carbonyl group, which afforded two bifunctional molecules (**DPP1** and **DPP2**, Figure 2.1). Furthermore, a minor structural difference (*i.e.*, a dimethylamino functionality,

suggested to be critical for Aβ interaction),[30,32,49] could help elucidate a structure-reactivity relationship. **DPP1** was synthesized as previously established.[34-36] The new compound, **DPP2**, was prepared by slight modifications to a previously reported method (Scheme 2.1).[36]

In order to predict potential applications of **DPP1** and **DPP2** in the brain, values of Lipinski's rules and logBB, theoretical measures of blood-brain barrier (BBB) penetration, were calculated.[7,50,51] To verify this prediction, an *in vitro* parallel artificial membrane permeability assay adapted for BBB (PAMPA-BBB) was performed.[30] Permeability values ($-\log P_e$) were measured to be 4.2 (±0.1) for both **DPP1** and **DPP2**. Based on empirical classification of BBB-permeable molecules (*i.e.*, verapamil),[30] **DPP1** and **DPP2** would also be likely to cross the BBB.

Scheme 2.1. Synthesis of **DPP2**.

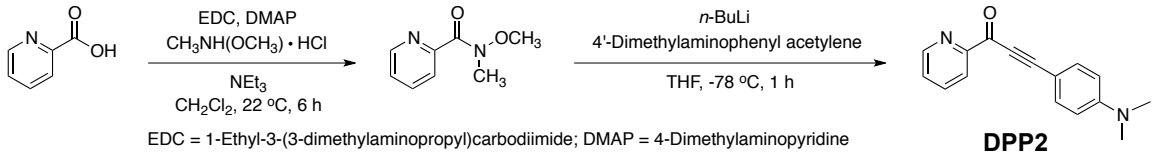

Studies to determine the solution speciation of **DPP1** and **DPP2**, UV-Visible (UV-Vis) variable-pH titration experiments (I = 0.10 M NaCl) were conducted at room temperature from pH 2.0 to 10.[28,30] An acidity constant (pK_a) for **DPP1** (pK_a = 2.035(5)) and two pK_a values for **DPP2** (pK_{a1} = 7.106(1) and pK_{a2} = 2.959(4)) were obtained, indicating the generation of a monoprotonated (H**DPP1**$^+$) and diprotonated species (H_2**DPP2**), respectively (Figure 2.2). Based on these data, the generated solution speciation diagrams of **DPP1** and **DPP2** suggest that at physiologically relevant pH (*i.e.*, 7.4), their neutral forms, which may more easily penetrate the BBB, are relatively predominant (**DPP1**, 100%; **DPP2**, *ca*. 65%).

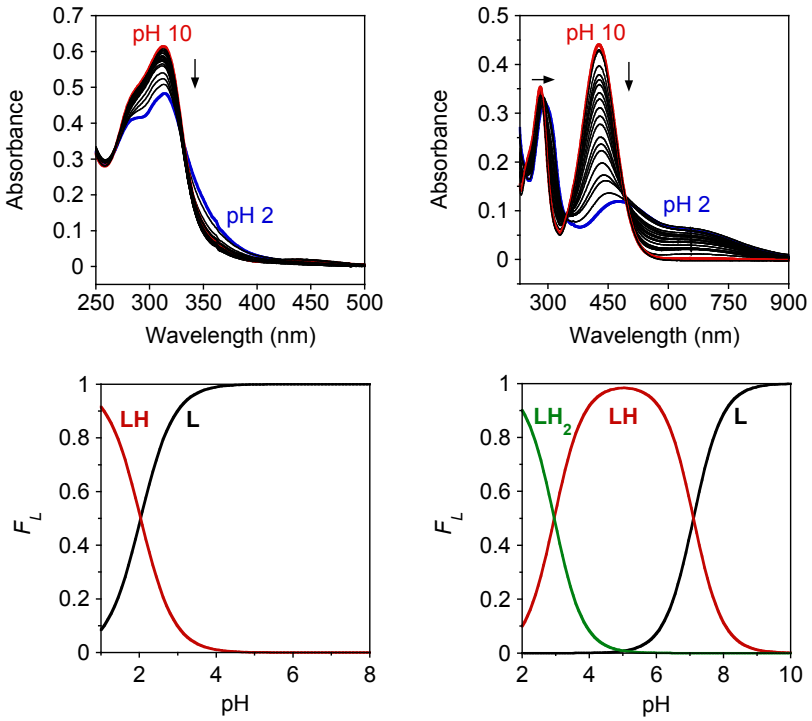

					pK_a[a]	
					DPP1	**DPP2**
LH_2	⇌	LH + H		(pK_{a1})	–	7.106(1)
LH	⇌	L + H		(pK_{a2})	2.035(5)	2.959(4)

Figure 2.2. Solution speciation studies of **DPP1** and **DPP2**. **Top**: UV-Vis spectra of **DPP1** (40 μM, left) and **DPP2** (20 μM, right) in the range of pH 2 - 10. **Middle**: Solution speciation diagrams for **DPP1** (left) and **DPP2** (right) (F_L = fraction of compound with given protonation). **Bottom**: Acidity constants (pK_a) of L (L = **DPP1** or **DPP2**). Charges are omitted for clarity. [a] Error is shown in the last digit. Conditions: I = 0.10 M NaCl; room temperature.

Metal Binding Properties of DPP1 and DPP2

Metal binding properties of **DPP1** and **DPP2** (specifically, Cu^{2+} and Zn^{2+}) were studied using UV-Vis and nuclear magnetic resonance (NMR) spectroscopy. Upon the addition of $CuCl_2$ (1 - 20 equiv) to a solution of **DPP1** and **DPP2** in EtOH, new optical bands were observed indicating Cu^{2+} binding to the ligand (Figure 2.3b). In particular, in the presence of Cu^{2+}, **DPP2**, which has a dimethylamino group, showed a distinguishable optical shift from 407 to 525 nm. NMR was

employed to investigate Zn^{2+} binding to the ligand in detail. When 1 equiv of $ZnCl_2$ was introduced in a solution of **DPP1** or **DPP2** (CD_3CN), noticeable downfield chemical shifts of the pyridyl protons were recorded (Figure 2.3c), demonstrating that Zn^{2+} binding to the ligand occurred through the pyridyl N-donor atom.

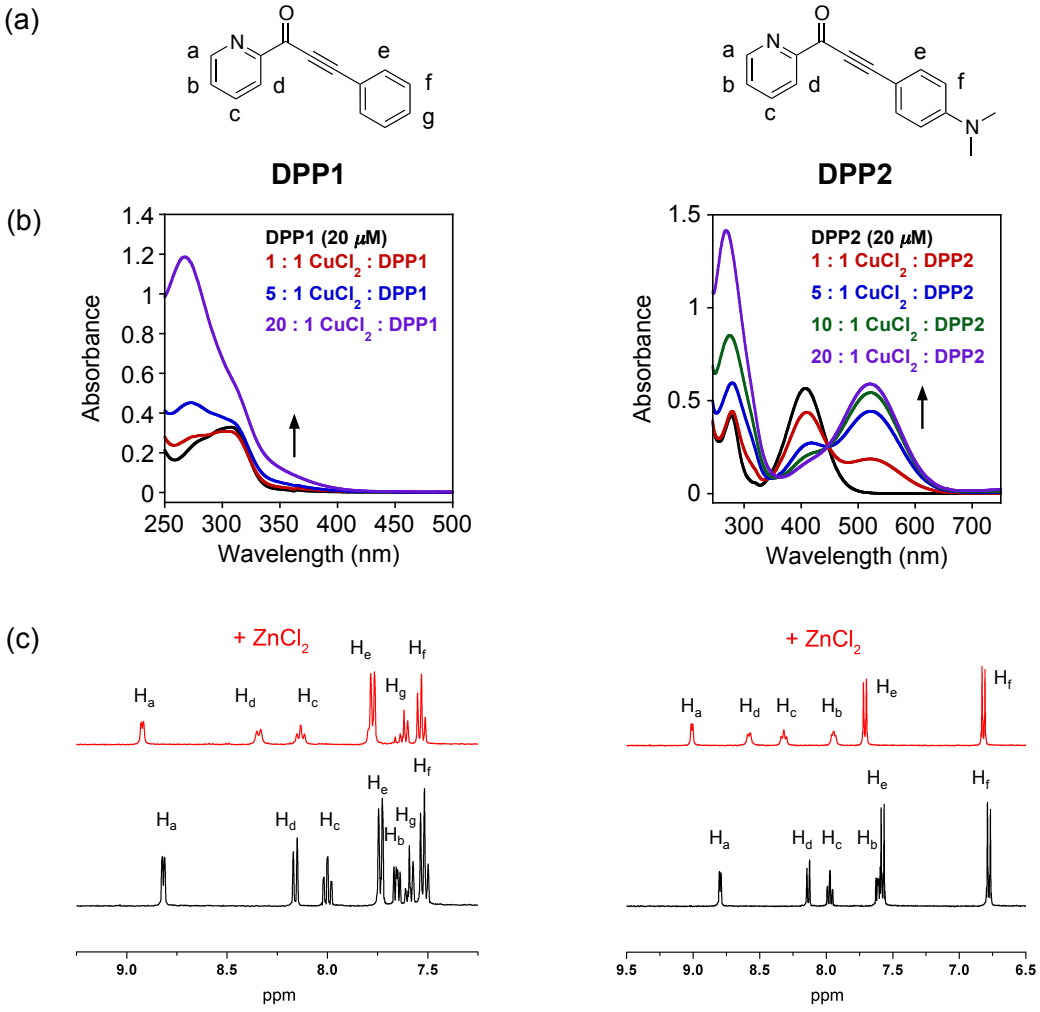

Figure 2.3. Interaction of DPP1 and **DPP2 with Cu^{2+} and Zn^{2+}**. (a) Assigned chemical structures of **DPP1** (left) and **DPP2** (right) (b) UV-Vis spectra of **DPP1** (left) and **DPP2** (right) with $CuCl_2$ (1 - 20 equiv) in EtOH at room temperature (incubation for 2.5 h (for **DPP1**) and 5 min (for **DPP2**)). (c) ^1H NMR spectra of **DPP1** (black) or **DPP2** (black) with $ZnCl_2$ (red) in CD_3CN at room temperature ([compound] = 4 mM; [$ZnCl_2$] = 4 mM).

To obtain binding stoichiometry and approximate binding affinity, solution speciation of the Cu^{2+}–**DPP2** complex was also studied (1:2 [Cu^{2+}]/[**DPP2**]; I = 0.10 M NaCl, room temperature) through UV-Vis variable-pH titration experiments. Based on the pK_a values of **DPP2** and these titration data, stability constants for the Cu^{2+}–**DPP2** complexes were obtained (Figure 2.4, M + LH $\rightleftharpoons$ M(LH) (logβ_1 = 12.99(9)); M + L $\rightleftharpoons$ ML (logβ_2 = 5.85(3)); M = Cu^{2+}, L = **DPP2**). A solution speciation diagram was generated from these stability constants, suggesting that the major species at pH 7 are a mixture of Cu(LH) and CuL complexes in a ratio of 3:2. Free Cu^{2+} was indicated up to pH 7, showing pCu = 6.6 at pH 6.6 (pCu = −log[$Cu_{unchelated}$]) (Figure 2.4),[28,30,52] which suggests the approximate dissociation constant (K_d) of Cu^{2+}–**DPP2** to be *ca.* high nanomolar. When compared to the reported K_d values of Cu^{2+}–Aβ (picomolar to nanomolar),[2,7,8,14] **DPP2** may interact with Cu^{2+} from soluble Cu^{2+}–Aβ species.

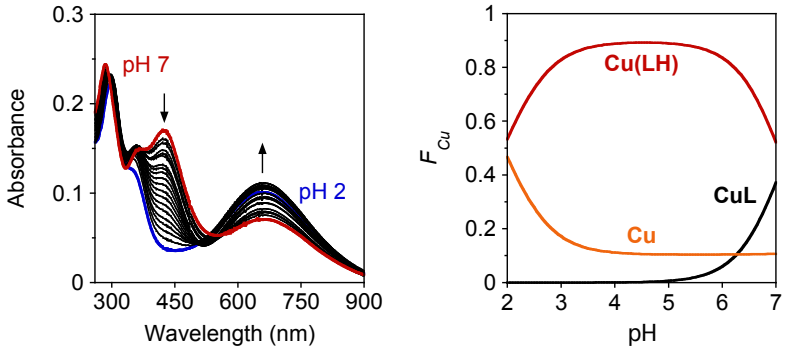

				logβ [a,b]
Cu	+ LH	$\rightleftharpoons$	Cu(LH)	12.99(9)
Cu	+ L	$\rightleftharpoons$	CuL	5.85(3)
Cu	+ 2L	$\rightleftharpoons$	CuL_2	1.7(6)

Figure 2.4. Solution speciation investigation of the Cu^{2+}–**DPP2** complex. **Top left**: UV-Vis spectra (pH 2 - 7) for the Cu^{2+}–**DPP2** complexes. ($[Cu^{2+}]/[L]$ = 1:2; $[Cu^{2+}]_{total}$ = 10 μM; 7 h incubation with ligand (L), L = **DPP2**; room temperature). **Top right**: Solution speciation diagram of the Cu^{2+}–**DPP2** complexes (F_{Cu} = fraction of free Cu and Cu complexes). **Bottom**: Stability constants (logβ) of the Cu^{2+}–**DPP2** complexes. Charges are omitted for clarity. [a] Error is shown in the last digit. [b] The species containing CuL_2 was introduced into the calculation model yielding a good fit to the data.

In order to test Cu^{2+} binding of **DPP2** in the presence of Aβ species (Figure A.1), **DPP2** was added to the solution of Aβ pre-incubated with 1 equiv of $CuCl_2$. The new spectral features coincided with those of the Cu^{2+}–**DPP2** complex without Aβ (Figure A.1). In the presence of Aβ, the binding of **DPP2** to Cu^{2+} occurred more slowly, proposing that Aβ could interfere with metal binding to the ligand. Taken together, our spectroscopic studies present the capability of **DPP1** and **DPP2** to chelate Cu^{2+} and Zn^{2+}, as well as the potential interaction of **DPP2** with Cu^{2+} in the presence of Aβ species, which may be associated with reactivity toward metal–Aβ species (*vide infra*).

The metal selectivity of **DPP1** and **DPP2** was also investigated by competitive reactions with Cu^{2+} over biologically relevant divalent metal ions (Mg^{2+}, Ca^{2+}, Mn^{2+}, Fe^{2+}, Co^{2+}, Ni^{2+}, and Zn^{2+}), monitored by UV-Vis. As depicted in Figure A.2, **DPP1** and **DPP2** displayed selectivity for Cu^{2+} over Mg^{2+}, Ca^{2+}, Mn^{2+}, and Zn^{2+}. Binding of both ligands to Co^{2+} and Ni^{2+} was, however, also observed. Considering the lower abundance of Co^{2+} and Ni^{2+} than Cu^{2+} in biological systems,[53,54] the overall metal selectivity of **DPP1** and **DPP2** may be sufficient to be used for targeting and interacting with Cu^{2+}–Aβ species in heterogeneous environments like the brain.

Aβ Interaction with DPP1 and DPP2 Investigated by MS and Docking Studies

The interaction of **DPP1** and **DPP2** with $A\beta_{1-40}$ in the absence of metals ions was probed by electrospray ionization-mass spectrometry (ESI-MS), tuned to preserve non-covalent protein–

ligand interactions.[43] At a low Aβ concentration (10 μM), a small signal corresponding to the interaction between **DPP2** (30 μM) and the Aβ monomer in the 3+ charge state could be detected, while no interaction between **DPP1** (60 μM) and the peptide was observed under these conditions (Figure A.3). At high concentrations of the peptide (100 μM) and compounds (600 μM), both **DPP1** and **DPP2** interacted with Aβ species to different extents (Figure 2.5a). Data for **DPP1** indicated that the molecule interacted broadly with Aβ monomers and oligomers in 1:1, 2:1, and 3:1 Aβ to ligand ratios. In the case of **DPP2**, a stronger preference toward larger Aβ oligomers was shown, but with similar stoichiometries as **DPP1**. The total bound intensities recorded from MS data, and those from individual oligomeric species were shown in Figure 2.6b and Table 2.1. The intensities shown were normalized for both non-specific interactions and artifactual complexes formed during the electrospray process using Aβ:thioflavin-T binding data as a control, and ion mobility separation was used to separate oligomers that overlapped in m/z.[6,43,55] From these data, it was clear that, at high concentrations, a higher proportion of **DPP1** was bound to Aβ species than **DPP2**, but that both could be classified as having weak Aβ affinity in solution (low mM K_d). Therefore, a weak Aβ/compound interaction was captured by MS. Normalized intensity MS data suggest that **DPP2** binding was almost exclusively driven through Aβ multimer interactions (Figure 2.5b). Overall, our MS results suggest that while both compounds could interact with Aβ species at high concentrations, **DPP2** was able to bind Aβ species at both low and high concentrations.

In order to visualize the potential interaction between Aβ and **DPP1**/**DPP2**, docking studies by AutoDock Vina were performed using the previously determined NMR structure (PDB 2LFM) of A$\beta_{1\text{-}40}$ monomer.[45,46] Typically, both compounds were positioned between the α-helix and the unstructured *N*-terminal side of Aβ (Figures 2.5c and Figure A.4). Most

docked structures showed a non-specific orientation of the ligand with respect to the surface features of Aβ. Our preliminary docking studies support the interaction of the compounds with Aβ monomer, observed by MS.

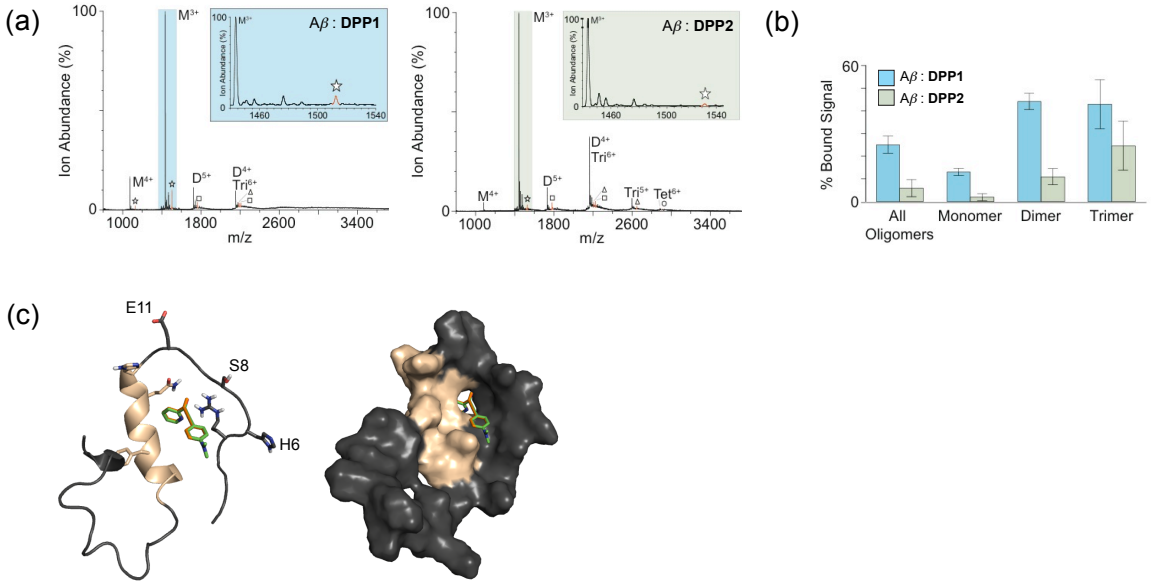

Figure 2.5. Interactions of **DPP1** and **DPP2** with Aβ species. (a) MS data for A$\beta_{1\text{-}40$:**DPP1**/**DPP2** complexes ([Aβ] = 100 μM; [compound] = 600 μM; M = monomer, D = dimer, and T = trimer). Many binding stoichiometries were detected, including 1:1 (star), 2:1 (square), and 3:1 (triangle). (b) A histogram showing the total bound MS signal intensity, normalized for non-specific interactions and ESI-MS artifacts, for each binding stoichiometry observed in (a). (c) Docking studies of **DPP1 (**orange**)** and **DPP2 (**green**)** with A$\beta_{1\text{-}40}$ (PDB 2LFM) by AutoDock Vina. Poses for both compounds were overlapped in this conformation (other conformations, Figure A.4). The helical region of Aβ (H13 - D23) is highlighted in color (tan) in both the cartoon (left) and surface (right) representations.

Effects of DPP1 and DPP2 on Metal-free and Metal-induced Aβ *In Vitro*

Confirming metal binding and Aβ interaction properties (bifunctionality) of **DPP1** and **DPP2**, their influence on of metal-free and metal-induced Aβ aggregation were studied *in vitro*.[27-33] To investigate if **DPP1**/**DPP2** can control the formation of metal-free and metal-induced Aβ

aggregates or transform preformed metal-free and metal-induced Aβ aggregates, inhibition (Figure 2.6) and disaggregation experiments (Figure A.5) were conducted. The visualization of various-sized Aβ species from both inhibition and disaggregation studies were carried out by native gel electrophoresis and SDS-PAGE followed by Western blotting with an anti-Aβ antibody (6E10), while morphological changes were identified by transmission electron microscopy (TEM).[27-32]

In the inhibition studies, different reactivity of **DPP1** or **DPP2** toward metal-induced Aβ species over metal-free Aβ species was observed. In the case of metal-involved Aβ aggregation, Aβ species with a wide range of MW were indicated with **DPP2** for both Cu^{2+}- and Zn^{2+}-treated samples upon longer incubation (Figure 2.6a, lanes 6 and 9). In the samples containing **DPP1 (**lanes 5 and 8), less intense gel bands were detected across the longer incubation time, suggesting that further Aβ aggregation may have occurred. The reaction of **DPP1** or **DPP2** with metal-free Aβ also exhibited a different distribution of various-sized Aβ species (Figure 2.6a, lanes 2 and 3). Aβ species formed with compounds in both metal-mediated and metal-free conditions were not completely denatured by SDS implying that these molecules may generate different Aβ assemblies (Figure 2.6b). TEM images of metal-induced Aβ species incubated with **DPP2** for 24 h revealed smaller amorphous aggregates compared to **DPP1**; some of the metal-free Aβ species treated with **DPP1** and **DPP2** presented similar morphology to those untreated with compounds (Figure 2.6c). Overall, **DPP1** and **DPP2** displayed the ability to recognizably modulate metal-induced Aβ aggregation to different extents.

Furthermore, for the disaggregation studies, in metal-mediated conditions, **DPP2**- treated metal-triggered Aβ aggregates presented different-sized Aβ species than **DPP1**-treated samples, indicating that **DPP2** could alter the properties of preformed Aβ aggregates to a greater extent

than **DPP1 (**Figure A.5a**)**. In the metal-free conditions, more various-sized Aβ species were indicated in the presence of **DPP2** than **DPP1 (**in particular, at 4 h, Figure A.5a, lanes 2 and 3**)**. The Aβ species generated with compounds in both metal-triggered and metal-free conditions were relatively stable in the presence of SDS (Figure A.5b). As shown in Figure A.5c, **DPP2** was able to reorganize preformed structured metal-Aβ aggregates to amorphous species more noticeably than **DPP1**. Taken together, the results from both the inhibition and disaggregation experiments presented that **DPP1** and **DPP2** could regulate metal-involved Aβ aggregation over metal-free aggregation *in vitro* differently. Moreover, the structural variation (*i.e.*, dimethylamino functionality) was shown to possibly differentiate the reactivity with metal–Aβ species.

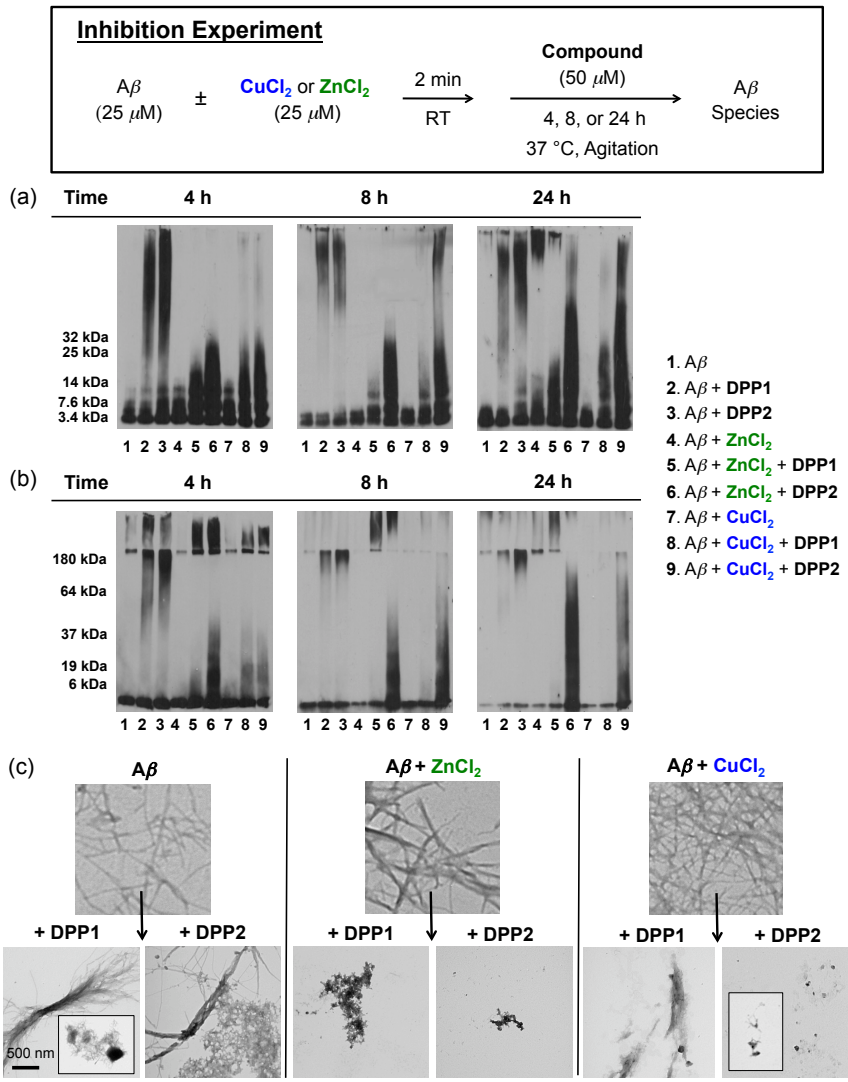

Figure 2.6. Inhibition experiment (scheme, top). Analysis of various-sized Aβ species by (a) native gel electrophoresis and (b) SDS-PAGE (non-reducing conditions) with Western blot. (c) TEM images of the 24 h incubated samples. Conditions: [Aβ] = 25 μM; [$CuCl_2$ or $ZnCl_2$] = 25 μM; [compound] = 50 μM; pH 6.6 (for Cu^{2+} samples) or 7.4 (for metal-free and Zn^{2+} samples); 4, 8, or 24 h incubation; 37 °C; constant agitation.

Summary and Perspective

Following the incorporation approach, we have developed bifunctional small molecules (**DPP1** and **DPP2**) composed of a metal chelation site and a diphenylpropynone framework (for Aβ interaction), which could possibly serve as chemical reagents to target and modulate metal–

Aβ species *in vitro*. Their bifunctionality (metal chelation and Aβ interaction) was confirmed by physical methods and preliminary docking studies. Biochemical and TEM studies revealed that **DPP1** and **DPP2** could modulate metal-induced Aβ aggregation *in vitro*. Notably, **DPP2**, which has a dimethylamino group, exhibited more apparent reactivity toward metal–Aβ species, compared to **DPP1**. This suggests that the interaction and reactivity of molecules with metal–Aβ species can be tuned by such structural variations (a structure-interaction-reactivity relationship). **DPP1** and **DPP2**, however, would be limited in their biological applications since they displayed cytotoxicity in living cells at low micromolar concentrations (Figure A.6). Overall, the promising *in vitro* reactivity of these potentially BBB-permeable molecules toward metal–Aβ species warrants pursuit of structural modifications that would improve the viability of diphenylpropynone derivatives in biological settings, followed by more detailed characterization by MS and molecular modeling. This study has demonstrated the capability of two diphenylpropynone derivatives to target and modulate the reactivity of metal-Aβ species, which can be further optimized toward the development of future chemical reagents and therapeutics for AD.

Acknowledgment. This study was supported by the Alzheimer's Art Quilt Initiative, the Alzheimer's Association (NIRG-10-172326), and the Ruth K. Broad Biomedical Foundation (to M.H.L.), as well as start-up funding from the University of Michigan (to B.T.R.). A.K., M.T.S., and A.S.D. are grateful for the Research Excellence Fellowship from the Department of Chemistry at the University of Michigan, the NIH Training grant (T32 CA140044), and the NSF Graduate Research fellowship, respectively. We thank Dr. Xiaoming He for synthetic assistance and Nathan Merrill for the NMR measurement for Zn^{2+} binding studies.

Supporting Information

Table A.1, and Figures A.1 – A.6 are available in Appendix A

Acknowledgements

This study was supported by the Alzheimer's Art Quilt Initiative, the Alzheimer's Association (NIRG-10-172326), and the Ruth K. Broad Biomedical Foundation (to M.H.L.), as well as start-up funding from the University of Michigan (to B.T.R.). A.K., M.T.S., and A.S.D. are grateful for the Research Excellence Fellowship from the Department of Chemistry at the University of Michigan, the NIH Training grant (T32 CA140044), and the NSF Graduate Research fellowship, respectively. We thank Dr. Xiaoming He for synthetic assistance and Nathan Merrill for the NMR measurement for Zn^{2+} binding studies.

References

1. Alzheimer's Association *Alzheimers Dement.* **2012**, *8*, 131-168.

2. Kepp, K. *Chem. Rev*. **2012**, *112*, 5193-5239.

3. Hardy, J. A.; Higgins, G. A. *Science* **1992**, *256*, 184-185.

4. Jakob-Roetne, R.; Jacobsen, H. *Angew. Chem. Int. Ed.* **2009**, *48*, 3030-3059.

5. Rauk, A. *Chem. Soc. Rev.* **2009**, *38*, 2698-2715.

6. Teplow, D. B. Lazo, N. D.; Bitan, G.; Bernstein, S.; Wyttenbach, T.; Bowers, M. T.; Baumketner, A.; Shea, J. E.; Urbanc, B.; Cruz, L.; Borreguero, J.; Stanley, H. E. *Acc. Chem. Res*. **2006**, *39*, 635-645.

7. Scott, L. E.; Orvig, C. *Chem. Rev.* **2009**, *109*, 4885-4910.

8. DeToma, A. S.; Salamekh, S.; Ramamoorthy, A.; Lim, M. H. *Chem. Soc. Rev.* **2012**, *41*, 608-621.

9. Haass, C.; Selkoe, D. J. *Nat. Rev. Mol. Cell. Biol*. **2007**, *8*, 101-112.

10. Lovell, M. A.; Robertson, J. D.; Teesdale, W. J.; Campbell, J. L.; Markesbery, W. R. *J. Neurol. Sci.* **1998**, *158*, 47-52.

11. Frederickson, C. J.; Koh, J.-Y.; Bush, A. I. *Nat. Rev. Neurosci.* **2005**, *6*, 449-462

12. Gaggelli, E.; Kozlowski, H.; Valensin, D.; Valensin, G. *Chem. Rev.* **2006**, *106*, 1995-2044.

13. Faller, P.; Hureau, C. *Dalton Trans.* **2009**, 1080-1094.

14. Faller, P. *ChemBioChem* **2009**, *10*, 2837-2845.

15. Bourassa, M.; Miller, L. M. *Metallomics* **2012**, *4*, 721-738.

16. Zhu, X.; Su, B.; Wang, X.; Smith, M. A.; Perry, G. *Cell. Mol. Life Sci.* **2007**, *64*, 2202-2210.

17. Zatta, P.; Drago, D.; Bolognin, S.; Sensi, S. L. *Trends Pharmacol. Sci.* **2009**, *30*, 346-355.

18. Hureau, C.; Faller, P. *Biochimie* **2009**, *91*, 1212-1217.

19. Bonda, D. J.; Lee, H.-g.; Blair, J. A.; Zhu, X.; Perry, G.; Smith, M. A. *Metallomics* **2011**, *3*, 267-270.

20. Jomova, K.; Valko, M. *Toxicology* **2011**, *283*, 65-87.

21. Pithadia, A. S.; Lim, M. H. *Curr. Opin. Chem. Biol.* **2012**, *16*, 67-73.

22. Bush, A. I.; Tanzi, R. E. *Neurotherapeutics*, **2008**, *5*, 421-432

23. Hureau, C.; Sasaki, I.; Gras, E.; Faller, P. *ChemBioChem* **2010**, *11*, 950-953.

24. Braymer, J. J.; DeToma, A. S.; Choi, J.-S.; Ko, K. S.; Lim, M. H. *Int. J. Alzheimers Dis.* **2011**, *2011*, Article ID 623051.

25. Perez, L. R.; Franz, K. J. *Dalton Trans.* **2010**, *39*, 2177-2187.

26. Rodríguez-Rodríguez, C.; Telpoukhovskaia, M.; Orvig, C. *Coord. Chem. Rev.* **2012**, *256*, 2308-2332.

27. Sharma, A. K.; Pavlova, S. T.; Kim, J.; Finkelstein, D.; Hawco, N. J.; Rath, N. P.; Kim, J.; Mirica, L. M. *J. Am. Chem. Soc.* **2012**, *134*, 6625-6636.

28. Rodríguez-Rodríguez, C.; Sánchez de Groot, N.; Rimola, A.; Álvarez-Larena, Á.; Lloveras, V.; Vidal-Gancedo, J.; Ventura, S.; Vendrell, J.; Sodupe, M.; González-Duarte, P. *J. Am. Chem. Soc.* **2009**, *131*, 1436-1451.

29. Hindo, S. S.; Mancino, A. M.; Braymer, J. J.; Liu, Y.; Vivekanandan, S.; Ramamoorthy, A.; Lim, M. H. *J. Am. Chem. Soc.* **2009**, *131*, 16663-16665.

30. Choi, J.-S.; Braymer, J. J.; Nanga, R. P. R.; Ramamoorthy, A.; Lim, M. H. *Proc. Natl. Acad. Sci. U. S. A.* **2010**, *107*, 21990-21995.

31. Choi, J.-S.; Braymer, J. J.; Park, S. K.; Mustafa, S.; Chae, J.; Lim, M. H. *Metallomics* **2011**, *3*, 284-291.

32. Braymer, J. J.; Choi, J.-S.; DeToma, A. S.; Wang, C.; Nam, K.; Kampf, J. W.; Ramamoorthy, A.; Lim, M. H. *Inorg. Chem.* **2011**, *50*, 10724-10734.

33. He, X.; Park, H. M.; Hyung, S.-J.; DeToma, A. S.; Kim, C.; Ruotolo, B. T.; Lim, M. H. *Dalton Trans.* **2012**, *41*, 6558-6566.

34. Seregin, I. V.; Schammel, A. W.; Gevorgyan, V. *Org. Lett.* **2007**, *9*, 3433-3436.

35. Harkat, H.; Blanc, A.; Weibel, J.-M.; Pale, P. *J. Org. Chem.* **2008**, *73*, 1620-1623.

36. Friel, D. K.; Snapper, M. L.; Hoveyda, A. H. *J. Am. Chem. Soc.* **2008**, *130*, 9942-9951.

37. Di, L.; Kerns, E. H.; Fan, K.; McConnell, O. J.; Carter, G. T. *Eur. J. Med. Chem.* **2003**, *38*, 223-232.

38. Avdeef, A.; Bendels, S.; Di, L.; Faller, B.; Kansy, M.; Sugano, K.; Yamauchi, Y. *J. Pharm. Sci.* **2007**, *96*, 2893-2909.

39. *pION Inc. BBB protocol and test compounds*; Woburn (MA), **2009**.

40. Gans, P.; Sabatini, A.; Vacca, A. **1999**, *89*, 45-49.

41. Alderighi, L.; Gans, P.; Ienco, A.; Peters, D.; Sabatini, A.; Vacca, A. *Coord. Chem. Rev.* **1999**, *184*, 311-318.

42. Braymer, J. J.; Merrill, N. M.; Lim, M. H. *Inorg. Chim. Acta* **2012**, *380*, 261-268.

43. Sun, J.; Kitova, E. N.; Wang, W.; Klassen, J. S. *Anal. Chem.* **2006**, *78*, 3010-3018.

44. Hernández, H.; Robinson, C. V. *Nat. Protoc.* **2007**, *2*, 715-726.

45. Trott, O.; Olson, A. J. *J. Comput. Chem.* **2010**, *31*, 455-461.

46. Vivekanandan, S.; Brender, J. R.; Lee, S. Y.; Ramamoorthy, A. *Biochem. Biophys. Res. Commun.* **2011**, *411*, 312-316.

47. Reinke, A. A.; Seh, H. Y.; Gestwicki, J. E. *Bioorg. Med. Chem. Lett.* **2009**, *19*, 4952-4957.

48. Ono, M.; Watanabe, H.; Watanabe, R.; Haratake, M.; Nakayama, M.; Saji, H. *Bioorg. Med. Chem. Lett.* **2011**, *21*, 117-120.

49. Leuma Yona, R.; Mazères, S.; Faller, P.; Gras, E. *ChemMedChem* **2008**, *3*, 63-66.

50. Lipinski, C. A.; Lombardo, F.; Dominy, B. W.; Feeney, P. J. *Adv. Drug Deliv. Rev.* **2001**, *46*, 3-26.

51. Clark, D. E.; Pickett, S. D. *Drug Discov. Today* **2000**, *5*, 49-58.

52. Storr, T.; Merkel, M.; Song-Zhao, G. X.; Scott, L. E.; Green, D. E.; Bowen, M. L.; Thompson, K. H.; Patrick, B. O.; Schugar, H. J.; Orvig, C. *J. Am. Chem. Soc.* **2007**, *129*, 7453-7463.

53. Lippard, S. J.; Berg, J. M. University Science Books: California, 1994.
54. Gray, H. B.; Stiefel, E. I.; Valentine, J. S.; Bertini, I. University Science Books: California, 2007.

55. Bernstein, S. L.; Dupuis, N. F.; Lazo, N. D.; Wyttenbach, T.; Condron, M. M.; Bitan, G.; Teplow, D. B.; Shea, J. E.; Ruotolo, B. T.; Robinson, C. V.; Bowers, M. T. *Nat. Chem.* **2009**, *1*, 326-331.

Chapter 3: Influence of a Curcumin Derivative on hIAPP Aggregation in the Absence and Presence of Membrane Lipids

This chapter was adapted from the following publication:

Pithadia, A. S.; Bhunia, A.; Sribalan, R.; Tamilenthi, P*.; Fierke, C. A.; Ramamoorthy, A. *Chem. Commun*. **2015**. 10.1039/c5cc07792c.[III]

*CurDAc was provided by Padmini Tamilenthi

3.1. Introduction

Human islet amyloid polypeptide (hIAPP) or amylin, is a 37 residue peptide hormone secreted from β-cells within the islet of Langerhans in the pancreas. hIAPP has received much attention due to its possible involvement in the pathology of diabetes mellitus, or type-II diabetes.[1,2] The protein found in islet cell deposits was characterized as IAPP and further confirmed the deposits as amyloid fibers,[3] a particular form of misfolded proteins which adopt a cross-β sheet structure with each monomer in the fibril adopting a β-sheet structure. More careful analysis indicated that β-cell mass is reduced strongly in islets containing IAPP deposits suggesting a possible toxic effect of IAPP on β-cells due to intermediary species (*e.g*., oligomers) generated during amyloid fibril assembly. A well-studied mechanism of toxicity by IAPP is the disruption of cellular (plasma and organelle) membranes.[4] These disruption events are suggested to happen through pore-like and fragmentation mechanisms which compromise the integrity of the lipid bilayer.[5-9]

[III]ASP – biophysical studies; AB – NMR; RS and PT – synthesis of CurDAc

A method to probe the inhibition of aggregation as well as rescue membrane integrity has been through the employment of small molecules.[10-12] These chemical modulators could stabilize the monomer thus blocking the formation of toxic oligomers, divert the monomeric peptide to off-pathway non-toxic intermediates, prevent the primary nucleation process by destabilizing oligomers, or destabilize fibrils to form monomers or non-toxic oligomers. Specifically, natural products make a promising class of viable candidates as small molecule inhibitors of amyloids.[13-17] Curcumin, a natural product found abundantly in turmeric that is used in most south Asian spices, has been widely categorized as having therapeutic properties due to its antioxidant, anti-cancer, antibiotic and anti-amyloidogenic properties.[18] It has been shown to non-specifically bind to amyloid-β monomers and fibrils and modify the protein aggregation pathway;[18-21] but less is known about the interactions between curcumin and hIAPP. Curcumin has demonstrated inhibitory properties against hIAPP; however, its mechanism of action still remains elusive.[22,23] Many recent studies have focused on the anti-amyloidogenic, properties, but limited utility of curcumin, thus leading to the generation of rationally designed curcumin analogues and derivatives which have demonstrated to have increased stability and solubility compared to curcumin while showing very promising activity against amyloid proteins both *in vitro* and *in vivo*.[24-28]

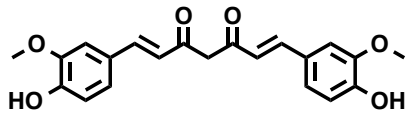

Curcumin

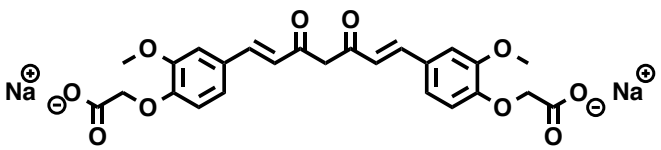

CurDAc

Figure 3.1. Chemical structures of curcumin ((1*E*,6*E*)-1,7-bis(4-hydroxy-3-methoxyphenyl)hepta-1,6-diene-3,5-dione) and **CurDAc** (sodium 2,2'-((((1*E*,6*E*)-3,5-dioxohepta-1,6-diene-1,7- diyl)bis(2-methoxy-4,1-phenylene))bis(oxy))diacetate). The hydroxyl moieties are modified to acetates.

Herein, we present a curcumin derivative, curcumin diacetate (**CurDAc**) (Figure 3.1) which exhibits increased stability and solubility in aqueous conditions, as an ideal small molecule candidate to study against IAPP aggregation and membrane stability. Our results demonstrate that this derivative has the propensity to modulate amyloid aggregation through an inhibition mechanism in the presence and absence of biological membrane mimics, unlike the results seen for this molecule with Aβ, which did not have a substantial influence on Aβ aggregation.[24] **CurDAc** serves as a template to modify curcuminoids which can help toward developing therapeutic compounds for modulating hIAPP aggregation and rescuing membrane integrity thus greatly reducing IAPP-induced toxicity. Biophysical characterization has helped us evaluate the effects of the curcumin derivative, **CurDAc** on an inhibitory mechanism of mature IAPP fibril formation.[29]

MATERIALS AND METHODS

Vanillin, 2,4-pentadione and n-butylamine were purchased from Sigma Aldrich. Tri-n-butyl borate was purchased from Alfa Aesar. All compounds were used without further purification. NMR characterizations for synthetic intermediates and **CurDAc** were performed using a Bruker Avance 300 MHz spectrometer. Mass spectra were recorded on a LCQ Fleet Mass Spectrometer (Thermo-Fisher Ltd., U.S.A.)

Scheme 3.1: Synthesis of CurDAc

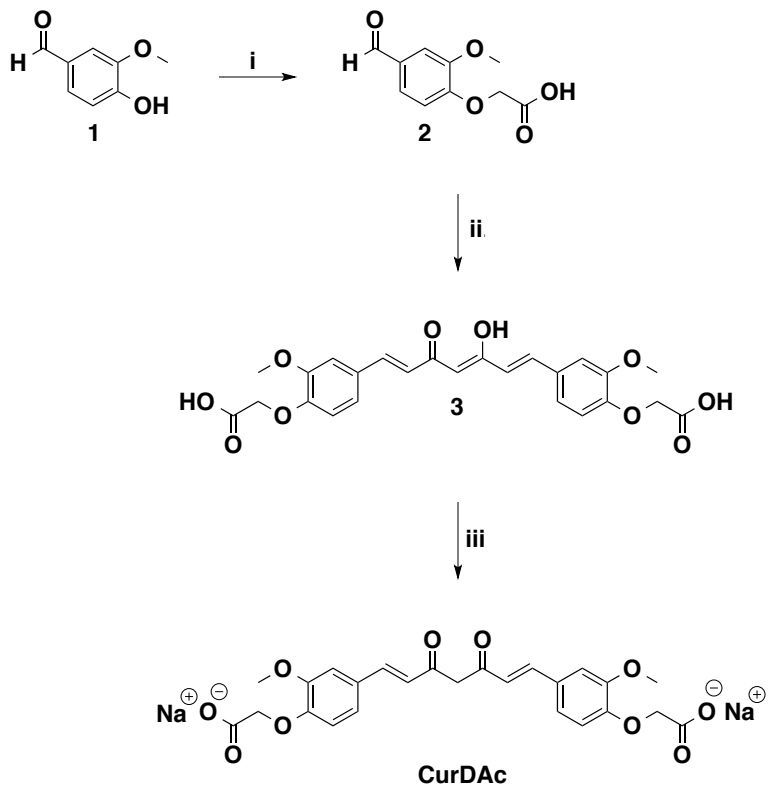

Reagent Conditions: (i) $ClCH_2COOH$; 1 N NaOH; H_2O; reflux, 12 h. (ii) 2,4-pentadione; boron oxide; tri n-butyl borate; n-butylamine; DMF; 70 ^{O}C, 4 h. (iii) ACN, 1 N NaOH, 0 ^{O}C, 5 min.

Synthetic procedure for 2-(4-formyl-2-methoxyphenoxy)acetic acid (2): **[24]**

The vanillin (1.0g, 0.0065 mol) was dissolved in 1 N NaOH (16 mL) solution. The solution was refluxed with chloroacetic acid (0.68g, 0.0072 mol) for 12 hrs. Then the reaction mixture was diluted with water (10 mL) washed with ethyl acetate (2 x 25 mL), then the aqueous layer was separated and acidified with conc HCl. Then the mixture was extracted with ethyl acetate (3 x 50 mL) (in the ethyl acetate layer the product was dissolved along with unreacted vanillin). The combined organic layers were extracted with saturated sodium bicarbonate solution (2 x 50 mL) and separated. The sodium bicarbonate solution was acidified with conc. HCl which gave the product as a white precipitate. The product was subsequently filtered and dried in hot air oven at

60 °C for 24 hrs (yield: 86.2%). ^{1}H NMR (300 MHz, $CDCl_3$) δ 9.86 (s, 1H), 7.44 – 7.42 (m, 2H), 6.92 (d, *J* = 8.7 Hz, 1H), 4.76 (s, 2H), 3.95 (s, 3H). ^{13}C NMR (75 MHz, $CDCl_3$+DMSO-D_6) δ 190.52, 169.57, 152.52, 130.57, 125.77, 112.14, 109.79, 65.39, 55.74. ESI-MS calculated. m/z 210.04. found 209.03 (M^--1).

Synthetic procedure for 2,2'-((((1E,6E)-3,5-dioxohepta-1,6-diene-1,7-diyl)bis(2-methoxy-4,1-phenylene))bis(oxy))diacetic acid (3):

To a 2,4-pentadione (0.099 mL, 0.95 mmol), boron oxide (0.065 g, 0.95 mmol), tri-n-butyl borate (0.50 mL, 1.89 mmol) and vanillin acetic acid (0.4g, 1.89 mmol) were added. The mixture was dissolved in dimethylformamide (2 mL) and heated to 70 °C. When the reaction temperature reaches 70 °C, n-butylamine (0.096 mL, 0.95 mmol) was added drop wise over 5 min. Then the reaction mixture was stirred at 70 °C for 4 hrs. Then the reaction mixture was added to 5% hot acetic acid solution (4 mL) and stirred for 3 hrs. It was diluted with water (25 mL) and extracted with ethyl acetate (2 x 50 mL). The combined organic layers were again washed with water (50 mL) and extracted with 10% sodium bicarbonate solution (2 x 25 mL). The aqueous layer was separated and neutralized with 2 N HCl (the pH of the solution should be 6.0-6.5). The yellow precipitate obtained was filtered and dried in vacuum. The filtered solid was washed with ethyl acetate afforded product **3** as a yellow solid (yield: 62.5%). ^{1}H NMR (300 MHz, DMSO-D_6) δ 7.64 (d, *J* = 15.6 Hz, 2H), 7.43 (s, 2H), 7.29 (d, *J* = 7.8 Hz, 2H), 7.96 – 6.86 (m, 4H), 6.18 (s, 1H), 4.79 (s, 4H), 3.90 (s, 6H). ESI-MS calculated. m/z 484.14. found 485.04 (M^++1).

Synthetic procedure for sodium 2,2'-((((1E,3Z,6E)-3-hydroxy-5-oxohepta-1,3,6-triene-1,7-diyl)bis(2-methoxy-4,1-phenylene))bis(oxy))diacetate (CurDAc)

The compound **3** (0.1 g, 0.20 mmol) was taken in the round bottom flask and cooled to 0 °C. To that solid 1 N NaOH (0.413 mL) was added and stirred for 5 min at 0 °C. Then to that solution acetonitrile (3mL) was added, the precipitate was obtained as the free acid. The product was filtered and dried in vacuum to give the sodium salt as a reddish brown solid (yield: 90.1%). ^{1}H NMR (300 MHz, D_2O) δ 7.13 (d, *J = 15.8 Hz*, 2H), 6.87 (d, *J = 8.0 Hz*, 2H), 6.81 (s, 2H), 6.57 (d, *J = 8.0 Hz*, 2H), 6.24 (d, *J = 15.8 Hz*, 2H), 4.29 (s, 4H), 3.74 (s, 6H). ESI-MS calculated. m/z 528.10. found 529.25 (M^{+}+1).

Peptide Preparation. To remove preformed aggregates, hIAPP was dissolved in hexafluoroisopropanol (HFIP) followed by removal of the solvent by lyophilization for 48 hours in aliquots of either 0.1 - 0.3 mg. The peptide aliquots were then stored at -20 ^{O}C. hIAPP monomer sample was prepared by dissolving the lyophilized peptide in chilled, dilute HCl (pH 4) to stock concentration between 150 – 200 μM, kept at 0 ^{O}C (ice), vortexed for 15 s. and bath sonicated (at 0 ^{O}C) for 1 min. Fresh hIAPP monomer samples were diluted into the appropriate buffer for each subsequent experiment.

Bicelle and Vesicle Preparation: All lipids were purchased from Avanti Polar Lipids (Alabaster, AL). DMPC/DHPC (2:1) bicelles were prepared by lypholizing the lipid film overnight. Lipids were rehydrated in phosphate buffered saline (10 mM, 100 mM NaCl, pH 7.4) and vortexed at 4 ^{O}C until lipids were completely dissolved. Lipid solutions underwent five freeze-thaw cycles to generate bicelles. Lipid vesicles were prepared by rehydration and micro-extrusion through a 100 nm membrane 21 times. Vesicles were measured by dynamic light scattering (DLS) to confirm their size (data not shown). Dye-filled vesicles were prepared at 10 mg/mL in a similar fashion, however rehydrated with a 6-carboxyfluorescein solution. After extrusion, dye-filled vesicles were separated on a size-exclusion column (GE Sephadex G50) to

remove any free carboxyfluorescein. The concentration of dye-filled vesicles was measured using the Stewart assay.

Thioflavin T (ThT) Fluorescence Assays. ThT fibril formation was measured by increased fluorescence emission upon binding of amyloid fibers to the commonly used amyloid-specific dye, ThT. ThT was added to a chilled phosphate buffered saline (10 mM phosphate, 100 mM NaCl, pH 7.4) to make a final dye concentration of 20 μM. For experiments without lipids, **CurDAc** (10 mM) was added. To solutions containing bicelles and vesicles, lipids were added to a final concentration of 100 - 1000 μM. hIAPP monomer solution was added to each well to a final peptide concentration of 10 μM. Fluorescence emission was measured in microplate formate on a BioTek Synergy 2 microplate spectrofluorometer using excitation and emission wavelengths of 440 and 480 nm, respectively.

Dye Leakage Fluorescence Assay: POPC/POPG (7:3) vesicles were prepared with 6-carboxyfluorescein as describe above. The final concentration of dye-filled vesicles used in each experiment was 0.2 mg/mL. Vesicles were added to a solution of PBS (10 mM, 100 mM NaCl, pH 7.4) and to this **CurDAc** (10 μM) was added. An initial fluorescence scan (λ_{ex} = 490 nm; λ_{em} = 520 nm) was taken to ensure no free dye was present in solution. To each well hIAPP (10 μM) was then added. After 24 h, vesicles were treated with 0.1% Triton-X to burst the vesicles for the maximum fluorescence measurement. Control fluorescence scans (λ_{ex} = 490 nm) were run in the presence of 0.2 mg/mL carboxyfluorescein and 10 μM **CurDAc** to demonstrate no signal overlap between the dye and the small molecule.

Circular Dichroism (CD). CD measurements were performed on JASCO J-815 Spectropolarimeter using a 0.1 cm path length cell. Freshly prepared monomer solution was added to PBS (10 mM, 100 mM NaF, pH 7.4) at a final concentration of 20 μM. Samples

containing **CurDAc** were co-incubated with 20 mM compound. Molar CD per residue values were calculated using $\varepsilon = \theta_{obsd}/(3298lcn)$, where θ_{obsd} is the observed ellipticity measured in millidegrees, c is the molar concentration, l is the cell path length in centimeters, and n is the number of residues in the peptide.

Dynamic Light Scattering (DLS). Light scattering experiments were performed on hIAPP (25 μM) and hIAPP with **CurDAc** (25 μM) using a DynaPro Nanostar instrument from Wyatt Technology (Santa Barbara, CA). Light scattering was measured at 90°. The intensity correlation function and the distribution of the hydrodynamic radii (R_{hyd}) of the particles contributing to the scattering were determined using DYNAMICS software (Wyatt Technology).

Transmission Electron Microscopy (TEM). Samples for negative stain TEM analysis were deposited on continuous carbon films on copper rhodium 100 mesh grids (Electron Microscopy Sciences, EMS Hatfield PA.). Prior to adding samples, the grids were charged using a glow discharger for 15 s at 30 mA negative discharge. Aliquots from ThT experiments incubated for 4 h were adsorbed to the grids for 2 min prior to rinsing with two 10 μL drops of water for 10 s. Samples were blotted using No. 2 Whatman filter paper. Samples for TEM were then stained with a 10 μL drop of freshly filtered 2% uranyl acetate (EMS) for 15 s before blotting excess stain. Samples were analysed using a Philips CM-100 microscope operating at 80 kV.

Saturation Transfer Difference Nuclear Magnetic Resonance (STD NMR). Saturation transfer difference (STD) NMR experiments for a sample containing **CurDAc** (250 μM) and hIAPP monomers (25 μM) were carried at 25 ºC for 18 hours consecutively with an interval of 15 min using a Bruker 600 MHz NMR spectrometer equipped with a cryo probe. The peptide, hIAPP or its fibril was RF-irradiated at -1 (on-resonance) and at 40 ppm (off-resonance) for a duration of 2 s and 128 scans were co-added to get the spectrum. The selective RF-irradiation

was achieved by a train of Gaussian pulses with 1% truncation for a duration of 49 ms with an interval of 1 ms at 50 dB.

Results and Discussion

CurDAc was designed as a water-soluble derivative of curcumin that requires organic solvents for solubilization and use in aqueous buffered systems (Figure 3.1).[30] This was achieved through the insertion of an acetate moiety that introduces two negative charges on the framework at pH > 5 (sodium salt form, Scheme 3.1).[28] A degradation mechanism through the autoxidation of curcumin that occurs through the phenolic moieties has been proposed.[31] Therefore, by capping these sites, more stable derivatives can be formed, as in the case of **CurDAc** that appends acetate functional groups to diminish this oxidation event. These negative charges may also provide a molecular basis for interaction with hIAPP through electrostatic as well as hydrogen bonding. The design of a curcumin derivative was of particular interest due to the instability of curcumin in aqueous conditions, which has made it increasingly difficult to study the activity of the parent structure with amyloid proteins (Figure B.1).[25-27]

Both the excitation and emission profiles for **CurDAc** do not interfere with thioflavin-T (ThT), thus making it possible to study aggregation through fluorescence.[22] In our experimental conditions, hIAPP displayed a lag phase of ~75 min and fully mature fibrils at ~200 min (Figure 3.2A). In the presence of 1 equiv. **CurDAc**, a complete inhibition of hIAPP aggregation was seen, which is attributed to the stabilization of monomers, or low molecular weight (LMW) oligomers that do not consequently form β-sheet rich fibrillar species in the presence of a small molecule. To verify this inhibition and at the same time to rule out false positives results by fluorescence experiments, ^{1}H STD NMR experiment was employed (Figure 3.2B). This technique is commonly used to understand ligand-receptor interactions by measuring

the magnetization transfer between the receptor (hIAPP), which is irradiated at a specific on-resonance frequency, and the ligand (**CurDAc**).[32] The top spectrum is a standard ^{1}H NMR spectrum of **CurDAc** displaying only the aromatic region of the ligand. The ^{1}H STD spectrum displayed no signal when **CurDAc** was co-incubated with freshly prepared monomers, indicating that the ligand, **CurDAc**, and hIAPP monomers tumble fast in solution due to their low molecular weight. Remarkably, no signal was observed even when the experiment was continued over 18 h (**CurDAc** + monomer), suggesting that hIAPP did not exist in its fibrillar form and may be stabilized as LMW species through an inhibition mechanism. In contrast, when hIAPP fibril was added to the ligand, efficient magnetization transfer from the large-size hIAPP fibrils to **CurDAc** resulted in a strong STD effect, mainly in the aromatic region of the ligand revealing interaction of aromatic rings with hIAPP (Figure 3.2B, **CurDAc** + fibril). These results are also in good agreement with microscopy images (Figure B.2). Under the conditions of ThT assay, **CurDAc** induced small, but more amorphous, hIAPP species that may not propagate toward toxic higher-order fibrils.

As shown in Figure 3.3A, circular dichroism (CD) experiments revealed the expected random coil to β-sheet conformation transition of hIAPP after 24 h. However, in the presence of **CurDAc**, a more pronounced helical conformation was observed, indicating selective IAPP intermediate species stabilized through interactions with the ligand. This may occur through charge-charge interaction between **CurDAc** and hIAPP, which may force the peptide to a specific conformation and thus altering its aggregation properties rather than disrupting the helix to force IAPP aggregation as reported previously.[22] Investigations are on going to decipher if **CurDAc** is reordering the monomer to a helix, or if the small molecule binds to a helical conformation, similar to the interactions seen between curcumin and the amyloid protein

PrP.[33] This observation is unique to this derivative as studies on curcumin showed the instability of the helical intermediate upon incubation.[23] Dynamic light scattering (DLS) experiments further confirms the formation of a LMW hIAPP species in solution with **CurDAc** present. Filtered samples of **CurDAc** and hIAPP at 4 h showed relatively mono disperse intensity peaks ~10 nm in hydrodynamic radius (Figure B.3), different from peptide alone sample that has a heterogeneous dispersity of large oligomers and protofibrils between 50 and 100 nm (Figure B.3). This conformational change could be responsible for the inhibitory properties of **CurDAc**, which does not allow for specific interactions between hIAPP strands that are responsible for the formation and growth of fibrils.[34]

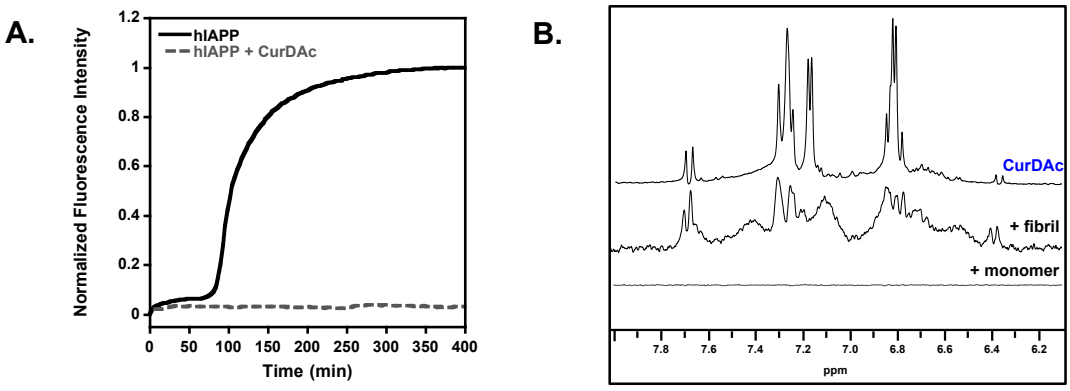

Figure 3.2. Inhibition of hIAPP by **CurDAc**. A) Thioflavin-T (ThT) fluorescence assay to measure the aggregation of hIAPP in the absence (10 μM, black) and presence of 1 equiv. **CurDAc** (10 μM, grey). B) ^{1}H NMR spectra of **CurDAc** (250 μM) alone (top, blue), ^{1}H STD NMR spectra of **CurDAc** + hIAPP (25 μM) fibril (middle) and **CurDAc** + hIAPP (25 μM) monomer (bottom). At a stoichiometric ratio of **CurDAc**, a full mitigation of fibrillation was observed. The absence of a STD signal in (B) indicates lack of large, slow-tumbling species or aggregates.

Inhibitors have the connotation that they mitigate fibril formation from freshly prepared monomers in solution; however, identifying some of these compounds as chemical modulators, instead of inhibitors is more accurate. The disassembly of hIAPP in solution was also monitored

using the ThT assay by adding **CurDAc** at ~200 min, when a high population of mature β-sheet containing fibrils was present (Figure B.4). Upon addition of **CurDAc**, a gradual loss in the ThT fluorescence signal was seen, inferring that the population of mature fibrils was diminishing in solution through the disaggregation of hIAPP. A depolymerisation event of α-synuclein has also been seen with curcumin-pyrazole derivatives,[21] alluding to the possible broader scope of **CurDAc** for disassembling fibrils of other amyloids. The intensity did not equilibrate to the baseline, which may suggest that the small molecule does not disaggregate hIAPP fibers to monomers.[16] Taken together, these results suggest that **CurDAc** has both the ability to halt fibril formation from fresh monomers as well as depolymerize preformed fibrils in solution.

Given the promising results, we wanted to further investigate how **CurDAc** behaves in the presence of lipid membrane to measure its amyloid inhibitory role towards lipid membrane protection and stabilization. Studies in the presence of lipid membrane have demonstrated that curcumin can interact with the lipid bilayer through two modes: (i) a surface interaction through electrostatic interaction with positively charged lipid head groups by H-bonding or (ii) a transmembrane insertion that segmentally orders lipid bilayers due to its rigidity.[35]

We investigated the influence of **CurDAc** on hIAPP aggregation in the presence of model membranes such as bicelles and lipid vesicles. The kinetics of hIAPP aggregation are altered in the presence of lipid bilayers due to possible surface level interactions that help nucleate monomers and LMW oligomers into fibril formation more quickly (Figure 3.4).[36] Though the exact mechanism for the interaction between **CurDAc** and membrane has not been worked out yet, surface adsorption of the small molecule could coat the membrane to disable fibrillation at the surface.

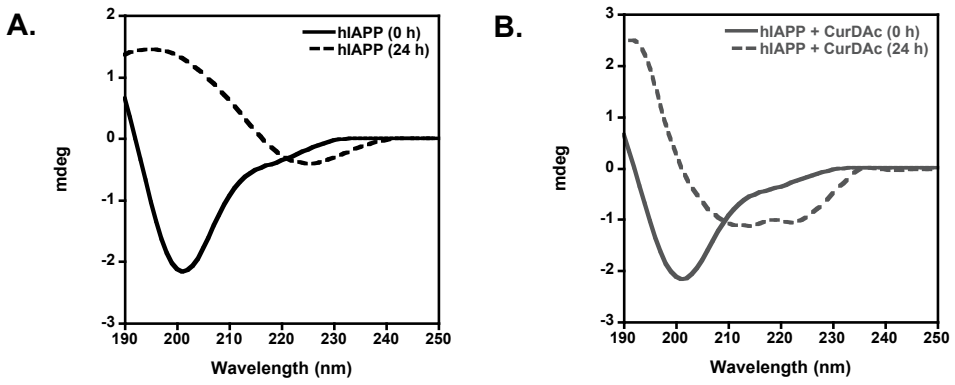

Figure 3.3. CD measurements indicating a change in peptide secondary structure after 24 h. CD spectra of 20 μM hIAPP solution without (A) and with (B) 20 μM **CurDAc**. A transition from random coil to b-sheet in the absence of **CurDAc** (A) and random coil to a-helix in the presence of 20 μM **CurDAc** (B, grey) was observed after 24 h. **CurDAc** may stabalize a specific monomer conformation or small oligomer assemblies of hIAPP.

Experimental results shown in Figures 3.4A and 3.4B suggest that the fibrillation of hIAPP was negligible when **CurDAc** was incubated with DMPC/DHPC (2:1) bicelles and hIAPP or POPC/POPG (7:3) large unilamellar vesicles (LUVs) and hIAPP. These results shed insights into molecular frameworks that could be used as membrane-protective agents against amyloid-induced cellular toxicity.[37] A surface level or membrane insertion mechanism has been considered and further investigated; but a membrane protection occurs with **CurDAc** as seen from dye leakage studies. POPC/POPG vesicles encapsulated with 6-carboxyfluorescein are traditionally used to measure membrane permeation through pore-like or detergent-like mechanisms.[38] In this case, we see direct membrane fragmentation of the vesicles by hIAPP (Figure B.5) [39,40] which are inhibited by the addition of **CurDAc**.

In summary, our study demonstrated a curcumin derivative, **CurDAc**, that can be used in stoichiometric amounts to suppress hIAPP fibril formation in solution both in the absence and presence of lipid membrane. The adoption of a helical intermediate may be a feature to exploit for further atomic-level structural investigations due to its stability over time. Furthermore, the

ability of **CurDAc** to protect lipid membrane may make it a useful scaffold for potential therapeutic applications. This small molecule possesses advantageous characteristics compared to its natural product counterpart, and further studies toward understanding its high-resolution interaction with hIAPP and lipid bilayer should be fruitful.

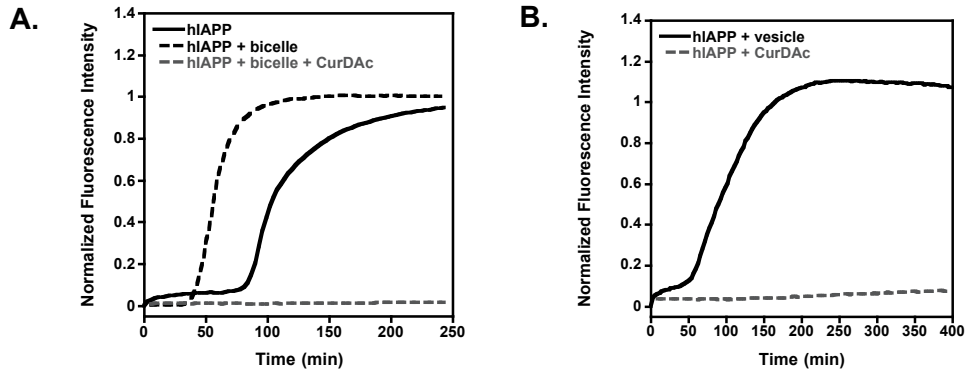

Figure 3.4. Thioflavin-T assays of 10 μM hIAPP (A, black) incubated with 2:1 DMPC:DHPC bicelles (A) and with **CurDAc** added (A, grey). B) Aggregation of 10 μM hIAPP in 7:3 POPC:POPG large unilamellar vesicles (black) and with the addition of **CurDAc** (grey). Fibrillation is mitigated in both model membrane systems showing full inhibition of fibrillation as discussed in the text.

Acknowledgements: This study was supported by the Protein Folding Initiative at Michigan and partly by funds from NIH (to A.R.). We acknowledge Dr. Patrick Walsh for assistance with acquiring TEM data, Dr. Hiren Patel for initial studies on **CurDAc**, and Dr. Jeffrey Brender for helpful scientific discussion for this manuscript.

References

1. P. A. Rushing, M. M. Hagan, R. J. Seeley, T. A. Lutz and S. C. Woods, *Endocrinol.*, 2000, **141**, 850-853.
2. P. Westermark, A. Andersson and G. T. Westermark, *Physiol. Rev.*, 2011, **91**, 795-826.
3. P. Westermark, C. Wernstedt, E. Wilander and K. Sletten, *Biochem. Biophys. Res. Commun.*, 1986, **140**, 827-831.

4. H. A. Lashuel, *Sci. Aging Knowledge Environ.*, 2005, **2005**, pe28.

5. A. Quist, I. Doudevski, H. Lin, R. Azimova, D. Ng, B. Frangione, B. Kagan, J. Ghiso and R. Lal, *Proc. Natl. Acad. Sci. U.S.A.*, 2005, **102**, 10427-10432.

6. T. A. Mirzabekov, M. C. Lin and B. L. Kagan, *J. Biol. Chem.*, 1996, **271**, 1988-1992.

7. J. D. Green, L. Kreplak and C. A. Goldsbury, *J. Mol. Biol.*, 2004, **342**, 877-887.

8. M. F. M. Engel, L. Khemtèmourian, C. C. Kleijer, H. J. D. Meeldijk, J. Jacobs, A. J. Verkleij, B. de Kruijff, J. A. Killian and J. W. M. Höppener, *Proc. Natl. Acad. Sci. U.S.A.*, 2008, **105**, 6033-6038.

9. R. Capone, F. G. Quiroz, P. Prangkio, I. Saluja, A. M. Sauer, M. R. Bautista, R. S. Turner, J. Yang and M. Mayer, *Neurotox. Res.*, 2009, **16**, 1-13.

10. S. Lee, X. Zheng, J. Krishnamoorthy, M. G. Savelieff, H. M. Park, J. R. Brender, J. H. Kim, J. S. Derrick, A. Kochi, H. J. Lee, C. Kim, A. Ramamoorthy, M. T. Bowers and M. H. Lim, *J. Am. Chem. Soc.*, 2014, **136**, 299-310.

11. B. J. Blanchard, A. Chen, L. M. Rozeboom, K. A. Stafford, P. Weigele and V. M. Ingram, *Proc. Natl. Acad. Sci. U.S.A.*, 2004, **101**, 14326-14332.

12. F. Evers, C. Jeworrek, S. Tiemeyer, K. Weise, D. Sellin, M. Paulus, B. Struth, M. Tolan and R. Winter, *J. Am. Chem. Soc.*, **131**, 2009, 9516-9521.

13. R. Mishra, D. Sellin, D. Radovan, A. Gohlke and R. Winter, *ChemBioChem*, 2009, **10**, 445-449.

14. Y. Porat, A. Abramowitz and E. Gazit, *Chem. Biol. Drug Design*, 2006, **67**, 27-37.

15. F. L. Palhano, J. Lee, N. P. Grimster and J. W. Kelly, *J. Am. Chem. Soc.* 2013, **135**, 7503-7510.

16. P. Cao and D. P. Raleigh, *Biochemistry*, 2012, **51**, 2670-2683.

17. L. M. Young, J. C. Saunders, R. A. Mahood, C. H. Revill, R. J. Foster, L.-H. Tu, D. P. Raleigh, S. E. Radford and A. E. Ashcroft, *Nat. Chem.*, 2014, **7**, 73-81.

18. K. Ono, K. Hasegawa, H. Naiki, M. Yamada, *J. Neurosci. Res*. 2004, **75**, 742-750.

19. A A. Reinke, J. E. Gestwicki, *Chem. Biol. Drug Des.* 2007, **70**, 206-215.

20. A. S. Strimpakos, R. A. Sharma, *Antioxid. Redox Signal* 2008, **10**, 511-545.

21. N. Ahsan, S. Mishra, M. K. Jain, A. Surolia, S. Gupta, *Sci. Rep*., 2015, **5**, doi:10.1038/srep09862.

22. S. Sparks, G. Liu, K. J. Robbins and N. D. Lazo, *Biochem. Biophys. Res. Commun.*, 2012, **422**, 551-555.

23. G. Liu, J. C. Gaines, K. J. Robbins and N. D. Lazo, *ACS Med. Chem. Lett.*, 2012, **3**, 856-859.

24. A. Kochi, H. J. Lee, S. M. Vithanarachchi, V. Padmini, M. J. Allen, M. H. Lim, *Curr. Alzheimers Res*. 2015, **12**, 415-423.

25. D. Yanagisawa, N. F. Ibrahim, H. Taguchi, S. Morikawa, K. Hirao, N. Shirai, T. Sogabe, I. Tooyama, *Neurobiol. Aging*, 2015, **36**, 201-210.

26. H. Endo, Y. Nikaido, M. Nakadate, S. Ise, H. Konno, *Bioorg. Med. Chem. Lett*., 2014, **24**, 5621-5626.

27. P. P. N. Rao, T. Mohamed, K. Teckwani, G. Tin, *Chem. Biol. Durg. Des*. 2015, **86**, 813-820.

28. R. Sribalan, M.Kirubavathi, G. Banuppriya, and V. Padmini, *Bioorg. Med. Chem. Lett.,* 2015, ***25***, 4282-4286.

29. H. R. Patel, A. S. Pithadia, J. R. Brender, C. A. Fierke, A. Ramamoorthy, *J. Phys. Chem. Lett*. 2014, **5**, 1864-1870.

30. B. T. Kurien, A. Singh, H. Matsumoto, R. H. Scofield, *Assay Drug Dev. Technol.* 2007, **5**, 567-576.

31. O. N. Gordon, P. B. Luis, H. O. Sintim, C. Schneider, *J. Biol. Chem*. 2015, **290**, 4817-4 828.

32. A. Bhunia, S. Bhattacharjya, S. Chatterjee*, Drug. Discov. Today*, 2012, **17**, 506-513.

33. J. Hafner-Bratkovic, J. Gaspersic, L. M. Smid, M. Bresjanac, R. Jerala*, J. Neurochem*. 2008, **104**, 1553-1564.

34. L. M. Young, P. Cao, D. P. Raleigh, A. E. Ashcroft and S. E. Radford, *J. Am. Chem. Soc.,* 2014, **136**, 660-670.

35. J. Barry, M. Fritz, J. R. Brender, P. E. S. Smith, D.-K. Lee, A. Ramamoorthy, *J. Am. Chem. Soc.* 2009, **131**, 4490-4498.

36. J. R. Brender, S. Salamekh, A. Ramamoorthy, *Acc. Chem. Res*. 2012, **45**, 454-462.

37. S. Kumar, A. D. Miranker, *Chem. Commun*. 2013, **49**, 4749-4751.

38. M. F. Sciacca, S. A. Kotler, J. R. Brender, J. Chen, D. K. Lee and A. Ramamoorthy, *Biophys. J.* 2012, **103**, 702-710.

39. J. R. Brender, U. H. N. Durr, D. Heyl, M. B. Budarapu, A. Ramamoorthy, *Biochim. Biophys. Acta Biomembr*. 2007, **1768**, 2026-2029.

40. J. Zhao, R. Hu, M. F. M. Sciacca, J. R. Brender, H. Chen, A. Ramamoorthy, J. Zheng, *Phys. Chem. Chem. Phys*. 2014, **16**, 2368-2377.

Chapter 4: Self Assembly of a 9-Residue Peptide Fragment of SARS Corona Virus E-protein: Mechanism of Self Aggregation and Amyloid-Inhibition of hIAPP

This chapter was adapted from the following publication:

Ghosh, A[§].; **Pithadia, A. S**[§].; Bhat, J.; Bera, S.; Midya, A.; Fierke C. A.; Ramamoorthy, A.; Bhunia, A. *Biochemistry*, **2015**, 54, 2249.[3]

[§]Authors contributed equally to this work.

4.1 Introduction

The formation of nanostructures through molecular self-assembly has been demonstrated to be a ubiquitous process in nature as seen by organic molecules (polymers), proteins, peptides and DNA. These nanostructures have been characterized by their highly ordered aggregate formation through non-covalent interactions (e.g., electrostatic, hydrogen bonds, van der Waals, and aromatic π-stacking and cation-π). The emerging field of nanotechnology has exploited self-assembly systems due to the key advantage that their physical, chemical, optoelectronic, magnetic and mechanical properties are tunable via control of their size and shape.[1] Interestingly, all the aforementioned non-covalent forces are quite weak in nature, individually, but cumulatively they support the self-organization of simple units into complicated and controlled structures.[2] Despite tremendous research efforts, the relative involvement of these forces in self-assembly processes is yet to be more clearly understood. Recently, substantial

[3] AG – synthesis and NMR; ASP – ThT, CD, NMR, writing manuscript; JB and SB – simulations; AM - docking

attention has been intended for the rational design and structural analysis of peptide based self-assembly due to their widespread diversity in chemical, structural and functional aspects.[1,3] Furthermore, the complex nature of biomolecules limits the comprehensive understanding of the factors controlling the self-assembling properties. To examine this in more detail, short peptides or peptide fragments can be constructed relatively quickly and may serve as the competent building blocks for self-assembled systems thus avoiding the complexities of forming and studying large protein structures.

Self-assembled peptide systems have also been utilized in studying protein-folding events in order to provide insight into the thermodynamic properties of protein folding and misfolding. These investigations have also helped gain information about specific structural motifs adopted by specific amino acid sequences and combinations which may be responsible for protein misfolding and amyloid formation. Therefore, studying the self-assembly of peptides has been utilized as an important tool for analyzing the local structure (*e.g.*, secondary structure) of peptide fragments in the context of the global protein structure.[4] These peptide nanostructures are generally formed from beta (β)-sheet motifs, although a few helical-based assemblies have also been reported.[5-8] Based on various structural, chemical and physical properties they are classified according to the following categories: a) lipid-like peptides, b) surfactant peptides, c) amphiphilic peptides, d) aromatic di-peptide motifs, e) cyclodextrin-based polyionic amino acids from known self-assembled proteins, e) cyclic peptides and f) arbitrarily chosen peptide sequence based on amino acid properties.[9] The unique supramolecular assemblies can be readily tuned by modifying structural properties such as changing the amino acid sequence or conjugating chemical groups or by varying experimental parameters such as pH or solvent. Peptide nanostructures have also been utilized in vast miscellaneous fields, from antibacterial

agents to molecular electronics with a great achievement and therefore have become of great interest to study.[10, 11]

Importantly, investigating self-assembly systems at the molecular level have been of particular value in studying the complex phenomena behind the aggregation of amyloid proteins and aggregation of other proteins related to fatal protein conformational disorders.[12] It has been found that amyloid-related diseases (e.g., Alzheimer's disease (AD), Prion diseases, Type II diabetes, Parkinson's disease, and Huntington's disease) are connected by the aggregation of relatively unstructured monomers into a β-sheet rich fibrillar aggregates.[13,14] In spite of the diversity in sequence homology, the fibrillar network have similar morphologies; however, the precise biochemical/biophysical pathways and mechanism of protein fibrillation still remain elusive. Self-assembled short peptides have the potential to serve as model systems to studying amyloid aggregation by simplifying the study of amyloidosis as seen in a study by Lynn and co-workers.[15] This can help probe specific protein-protein interactions between the small peptide assemblies and translate this information to elucidating the aggregation properties of the native peptide/protein. Furthermore, small peptide fragments from amyloid proteins (KLVFF in amyloid-β and NFGAIL in hIAPP) have demonstrated to have inhibitory properties, thus modifying or in some cases halting the aggregation pathway. Therefore, studying self-assembled peptide fragments may also help potentially uncover possible motifs that may be utilized for amyloid inhibition and eventually therapeutic applications.

In the present study, we have investigated and analyzed the self assembly of a 9 residue peptide (hereafter denoted as **TK9**) and its derivatives taken from the sequence of the carboxyl terminal (55-63) of SARS Corona Virus Envelope protein (Scheme 4.1).[16] Generally, corona viruses are enveloped and this enveloped (E) region may be the main culprit in causing virulence

related to various respiratory diseases such as, common colds, bronchiolitis, and acute respiratory distress syndrome in humans and other.[17] The E regions are peptide fragments consisting of 76-108 amino acids and composed of a flexible region at both N- and C- terminals and α-helical transmembrane (TM) region.[18] This region has shown to adopt mainly helical structure in the presence of SDS micelles, suggesting that a membrane surface may influence its secondary structure.[18] Upon mutation of the ^{56}VYVY^{59} region of the C-terminal tail in the SARS Corona virus, the secondary structure has changed to a more discrete β-structure.[18]

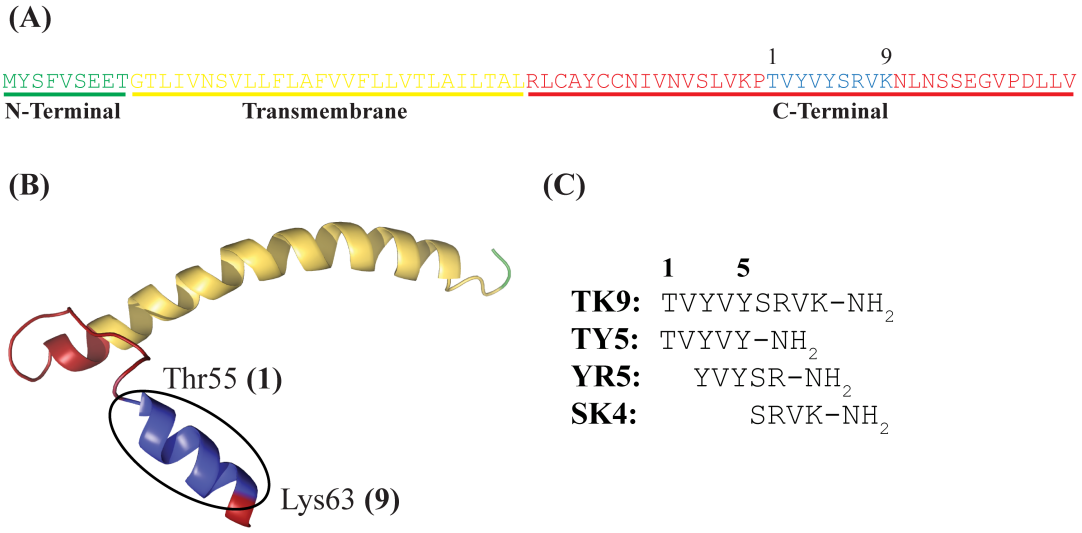

Scheme 4.1. (A) SARS CoV-E sequence with **TK9** region shown in blue. (B) The three-dimensional solution structure of SARS CoV-E protein in sodium dodecyl sulfate (SDS) micelle (2MM4.pdb). The C-terminal tail, Thr55 – Lys63 adopted alpha helical conformation in micelle, makerd by circle, used in this study. (C) The primary amino acid sequence of **TK9** or its shorter fragments.

To gain further insight, whether the short peptide, **TK9** and its variants have a self-assembling tendency, we carried out detailed biophysical and high resolution analyses of **TK9**. These data demonstrated that **TK9** self assembles and forms a β-sheet secondary structure in

solution. To support our experimental findings and also to extract out the atomic level interactions acting as a driving force for this self-assembly process we performed molecular dynamics (MD) simulations. Furthermore, we also studied the ability of **TK9** to inhibit the aggregation of a 37-residue human islet amyloid polypeptide protein (hIAPP) in order to obtain possible structural motifs that may be beneficial for the mitigation of hIAPP aggregation. Previous studies have shown that unstructured hIAPP monomers aggregate to form toxic intermediates and amyloid fibers that composed of β-sheet peptide structures that are implicated in type II diabetes. Therefore, there is considerable current interest in developing compounds to inhibit hIAPP aggregation and islet cell toxicity. In this context, the amyloid-inhibiting ability of **TK9** could be useful and aid in the development of potent amyloid inhibitors.

MATERIALS AND METHODS

Materials and preparation of stock solutions. The parent peptide, **TK9** and its shorter fragments (Scheme 1) were synthesized on a solid phase peptide synthesizer (Aapptec Endeavor 90) using Fmoc protected amino acids and Rink Amide MBHA resin (substitution 0.69 mmol/g; Novabiochem, San Diego, California) by following a solid phase peptide synthesis protocol described elsewhere.[19,20] The C-termini of the peptides are amidated. All the crude peptides were further purified by reverse phase HPLC (SHIMADZU, Japan) using a Phenomenix C18 column (dimension 250 × 10 mm, pore size 100 Å, 5-μm particle size) by linear gradient elution technique using Water and Methanol as solvent both containing 0.1% TFA as the ion pairing agent. The purity and molecular weight of the eluted peptides were confirmed by MALDI-TOF (Bruker, Germany). 4,4-dimethyl-4-silapentane-1-sulfonic acid (DSS) and deuterium oxide (D_2O) were purchased from Cambridge Isotope Laboratories, Inc. (Tewksbury, MA). Thioflavin

T dye was purchased from Sigma Aldrich (St. Louis, MO). Throughout the experiment HPLC grade water was used for sample preparation. hIAPP was purchased from Genscript (Piscataway, NJ). hIAPP was prepared by dissolving the peptide in hexafluoroisopropanol (Sigma Aldrich) followed by lyophilization. Peptide stock was dissolved in 100 μM HCl (pH 4), sonicated for 1 min, diluted into the appropriate buffer system and kept on ice until use.

Circular dichroism. All circular dichroism experiments were performed on Jasco J-815 spectrometer (Jasco International Co., Ltd. Tokyo, Japan) furnished with a Peltier cell holder and temperature controller CDF-426L at 25 ºC. The peptide concentrations were 25 μM for all CD measurements. The samples were scanned between 190 to 260 nm wavelength at a scanning speed of 100 nm min^{-1}. The data interval was 1 nm and path length 2.0 mm. All data-points are the resultant of an average of 4 repetitive scans. All experiments were performed in 10 mM phosphate buffer of pH 7.0. Each spectrum was baseline corrected with reference to buffer. The data obtained in mill degrees were converted to molar ellipticity (ME) ($deg.cm^2.dmol^{-1}$) and plotted against wavelength (nm).

Fluorescence assays. Tyrosine fluorescence experiments were performed using Hitachi F-7000 FL spectrometer with a 0.1 cm path length quartz cuvette at 25 ºC. Intrinsic tyrosine fluorescence property was used to monitor the self assembly property for tyrosine containing peptides **TK9**, **TY5**, **YR5** using an excitation wavelength of 274 nm and emission in a range of 290-370 nm.[21] The excitation and emission slit both were 5 nm. The peptide concentrations were 25 μM throughout the experiment. Thioflavin-T (ThT) experiments were performed on a BioTek multiplate reader using an excitation wavelength of 440 nm and emission wavelength of 485 nm. Samples were prepared by adding hIAPP (10 μM) to a buffer solution (10 mM phosphate, 150

mM NaCl, pH 7.4) containing ThT (20 μM) and varying concentrations of **TK9** monomer (0.5 – 2 equiv). **TK9** aggregates for the ThT assay were prepared by incubation at 37 ºC for 7 days.

Dynamic light scattering. DLS experiments were performed using Malvern Zetasizer Nano S (Malvern Instruments, UK) equipped with a 4-mW He-Ne gas laser (beam wavelength = 632.8 nm) and 173° back scattering measurement facility. All samples were filtered using 0.25-μm filter paper (Whatman Inc, NJ) and degassed before use and measured at 298 K using a low volume disposable sizing cuvette. The peptide concentration was kept at 10 μM in phosphate buffer (pH 7.0) during the duration of the experiment.

Nuclear magnetic resonance. The synthetic peptide, **TK9** and its analogues were dissolved in milli-Q water (pH 7.0). All NMR spectra were recorded at 298 K using Bruker Avance III 500 MHz NMR spectrometer, equipped with a 5 mm SMART probe. Two-dimensional total correlation spectroscopy (TOCSY) and rotating frame nuclear Overhauser effect spectroscopy (ROESY) spectra of **TK9** were acquired in water containing 10% D_2O and DSS (2,2-dimethyl-2-silapentane 5-sulfonate sodium salt) as an internal standard (0.0 ppm for methyl protons). The peptide concentration was kept at 1 mM for the sequential assignment and relaxation studies, respectively. TOCSY mixing time was set to 80 ms using the MLEV-17 spin-lock sequence to ensure coherence transfer via scalar couplings, whereas a 150 ms spin-lock mixing time was used for ROESY experiments. The TOCSY and ROESY experiments were performed with 456 *t1* increments and 2048 *t2* data points. The residual water signal was suppressed by excitation sculpting techniques. The spectral widths were set to 10 ppm in both dimensions with a saturation delay of 1.5 sec. Data acquisition and data processing were carried out using Topspin^{TM} *v3.1* software (Bruker Biospin, Switzerland).

The two-dimensional NMR data were assigned and analyzed using SPARKY[22] program. The cross peak intensities measured from ROESY spectra were qualitatively classified as strong, medium, and weak, which were then converted to upper bound distance limits of 3.0, 4.0, and 5.5 Å, respectively. The lower bound distance was constrained to 2.0 Å to avoid van der Waals repulsion. The backbone dihedral angle (phi, ϕ) was varied from -30^{o} to -120^{o} to restrict the conformational space for all residues. Finally, Cyana 2.1 software was used for structure calculation with the help of distance and dihedral angle restraints.[23] Several rounds of refinement were performed based on the NOE violations, and the distance constraints were accustomed accordingly. A total of 100 structures were calculated, and 20 conformers with the lowest energy values were selected to present the NMR ensemble and staring structure for coarse grain molecular dynamics simulation.

A series of one-dimensional proton NMR spectra for **TK9** and its analogues were recorded at different time intervals to determine their aggregation tendency. The spectra were acquired with water suppression with a spectral width of 12 ppm, 128 transients, a relaxation delay of 1.5 sec. The spectra were processed and plotted with TopSpin software (Bruker, Switzerland) using a line broadening of 1.0 Hz.

Saturation transfer difference (STD) NMR experiments for a sample containing **TK9** (0.5 mM) and hIAPP monomers (10 μM) were carried at 25 ºC for 12 hours consecutively with an interval of 15 min using a Bruker 600 MHz NMR spectrometer equipped with a cryo probe. The peptide, hIAPP or its fibril was irradiated at -1 (on-resonance) and at 40 ppm (off-resonance) for a duration of 2 s and 128 scans were co-added to get the spectrum. The selective irradiation was achieved by a train of Gaussian pulses with 1% truncation for a duration of 49 ms with an interval of 1 ms at 50 dB.

Relaxation studies. To gain access the atomic level dynamics present one-dimensional spin-spin (T_1) and spin-lattice (T_2) relaxation experiments for **TK9** were performed using 500 MHz Bruker Avance III NMR spectrometer. T_1 experiments were performed using the same protocol that we published earlier with different inversion recovery delays starting from 50 ms to 5 s.[24] Similarly, T_2 measurements were carried out using the CPMG sequence for a set of delays: 2, 6, 32, 100, 200, 400, 800, 2000, 3000 and 4000 ms.[25]

Scanning electron microscopy (SEM). The incubated peptide solutions were deposited on a glass slide (1 cm^2) and dried oven night in air. The slide was then coated with gold for 120 s at 10 kV voltage and 10 mA current. The samples were viewed on a ZEISS EVO-MA 10 scanning electron microscope equipped with a tungsten filament gun operating at 10 kV.

Transmission electron microscopy (TEM). The 500 μM peptide stock solutions were incubated at room temperature for up to 15 days and 10 μL aliquots of the solution were placed on 300 mesh Formvar/carbon coated copper TEM grids (Ted Pella, Redding, CA 96049, USA). It was allowed to adsorb on TEM grid for about 3-4 minutes and excess volume was removed with filter paper. The grid was negatively stained with 5 % (v/v) freshly prepared uranyl acetate in water. After 5 minute excess dye was removed and the grids were viewed on a JEOL **J**EM 2100 HR TEM microscope operating at 80 kV. A set of TEM samples for **TK9** were also viewed on a Philips Model CM-100 transmission electron microscope (80 kV, 25,000x magnification) Digital images were acquired using Gatan Digital Micrograph 2.3.0 image Capture Software.

Coarse-Grained Molecular Dynamics Simulations. Coarse-Grained (CG) molecular dynamics (MD) simulation of **TK9** was performed using Martini model.[26,27] Using this model, **TK9** is mimicked by 24 beads in a single chain, as shown in Figure S1. Simulation systems were built with 20 chains of beaded **TK9** placed randomly in a box of size 12 nm. Energy minimization

was initially conducted on peptide in a vacuum using the steepest descent method with a maximum step size of 0.01 nm and a force tolerance of 10 kJ mol^{-1} nm^{-1}. Solvation of the system was carried out with 59652 CG water molecules (each CG water molecule corresponds to 4 all atom water molecules). The solvated system was further minimized using the same parameters as that of energy minimization in a vacuum. Then MD simulation was performed using NPT. The velocities were assigned according to the Maxwell-Boltzmann distribution at 320 K. Temperature was kept at 310 K by the Berendsen method with a time constant of 0.3 ps, and the pressure was maintained at 1 bar with a time constant of 3 ps and a compressibility of 3×10^{-5} bar^{-1}. The periodic boundary conditions (PBC) were applied. The non-bonded Lennard-Jones (LJ) and electrostatic interactions were calculated using a cut off of 1.2 nm. Furthermore, the standard shift function in GROMACS was used to reduce undesired noise.[28] Specifically, the LJ potential and electrostatic potentials were shifted to zero from 0.9 and 0.0 nm, respectively, to the cut off distance (1.2 nm). A time step of 30 fs was used and trajectory was saved every 150 ps for analysis. The simulation duration was 1 μs. Structural changes in the assembly during the simulation run are captured at different time step as shown in (Figure C.2).

Reverse construction of all atom system. Reconstruction of all atom (AA) system from CG was carried out to regain the atomic details. At first, AA particles were placed near to the corresponding CG beads and coupled to CG beads by harmonic restraints. This restrained the system further and then was processed by simulated annealing (SA); the final relaxed atomic model was obtained by the gradual removal of the restraints.[29]

There construction simulations started from the snapshot at 999 ns time step of the CG simulations as illustrated in Figure C.3.The atomistic simulations were carried out with a 2-fs integration time step, and the temperature was controlled by coupling to a Nosé–Hoover

thermostat with a time constant of 0.1 ps.[30] Because of the random initial placement of the atomistic particles, no constraints were applied in the reconstruction simulations, except for SPC water.

For the simulations of the **TK9**, the 53 a6 parameter set of the GROMOS united atom force field was used.[31] The system was simulated within periodic boundary conditions. Non-bonded interactions were calculated using a triple-range cut off scheme: interactions within 0.9 nm were calculated at every time step from a pair list, which was updated every 20 fs. At this time steps, interactions between 0.9 and 1.5 nm were also calculated and kept constant between updates. A reaction-field contribution was added to the electrostatic interactions beyond this long-range cut off, with ϵr=62. In the simulations of bulk SPC water, at win range cut off scheme was used, with a single cut off at 0.9 nm and a pair list up dated every 20 fs. Here, along-range dispersion correction was applied in addition to the reaction field. Other simulation parameters are as given in Table C.1.

RESULTS

Design considerations for TK9 and its variants. The SARS-CoV Envelope region (Cov E) (Scheme 4.1A) contains a relatively hydrophobic C-terminal region (Scheme 4.1B), composed of an alpha helix (α-helix) at the trans-membrane followed by a β-structured region, ^{55}TVYVYSRVK^{63}, or **TK9**, which has been considered an essential sequence content for its function. This region has been predicted to be responsible for directing the protein to the Golgi region.[18,32,33] It should be mentioned that this type of motif remains conserved in other corona viruses and is abundantly expressed in infected cells and may also be critically involved in viral protein assembly.[34,35] Fourier transform infrared (FT-IR) spectroscopy investigations have also shown that this portion of the protein can intrinsically adopt both a random coil and β-

sheet conformation in the absence of a membrane environment.[32] The folding domain (β-structured region), which contains the sequence of TVYVYSRVK and its fragments (Scheme 4.1B) contain residues and sequences similar to those of amyloid proteins. This has led to the hypothesis that **TK9** may have similar properties to the folding domains of amyloid proteins (*e.g.*, amyloid-β), where certain residue regions have limited water solubility and adopt a β-sheet structure and may aggregate to form amyloid-like fibrillar species. This observation has made TK9 and its derivatives insightful nanostructure systems to study protein assembly and mechanism of folding.[36] Specifically, residues I46 – V62 contain branched and bulky side chains which may favor the formation of β-sheet structures.[37] The first five residues of **TK9, TY5** (TVYVY) (Scheme 4.1C) also contain a peptide motif demonstrated to form amyloid-like fibrils; therefore, this short peptide fragment and its derivatives namely, **TY5**, **YR5** and **SK4** (Scheme 4.1C) were chosen as model systems to give possible insights into amyloid folding events. These sequence motifs containing branched, hydrophobic residues as well as residues, which can form H-bonds, has been shown to have a higher aggregation propensity as seen with a Leu-Enkephalin mutant and VEALYL.[38-41]

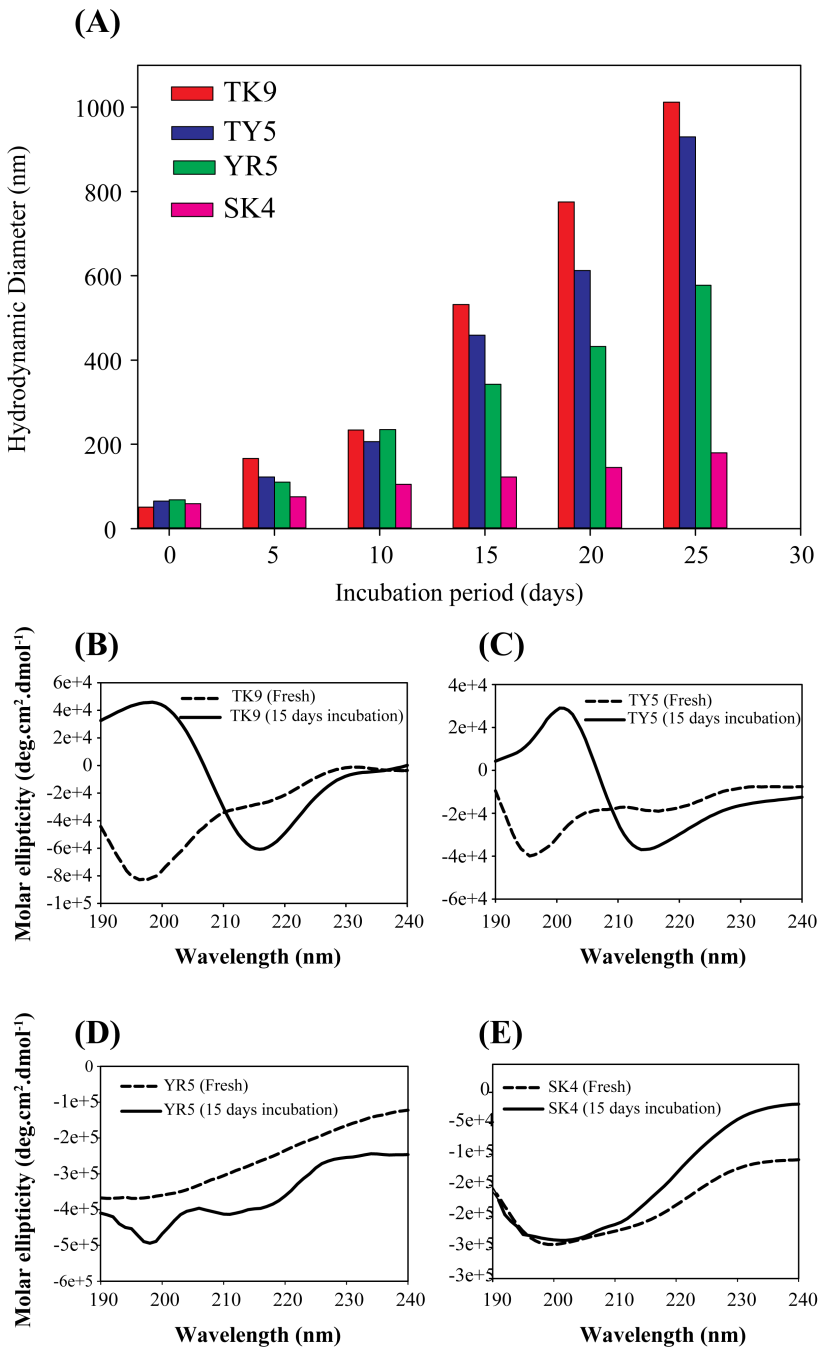

Figure 4.1. (A) Dynamic light scattering (DLS) plot for **TK9** (red), **TY5** (blue), **YR5** (green) and **SK4** (pink);the intensity vs. size distribution bar diagram are plotted at different time intervals. (B – E) Circular Dichroism (CD) plots of secondary structure of **TK9** and its fragments measured after freshly preparation and incubation with 15 days.

TK9 and TY5 are more prone to aggregation with increased incubation time. Dynamic light scattering (DLS) is an analytical method used to establish the size distribution of an ensemble of particles from Brownian motion property in solution.[42] Here, we employed DLS to access the size distribution of the supramolecular structures formed during different incubation periods. It is seen that freshly prepared **TK9** or its analogues, **TY5**, **YR5** and **SK4** (Scheme 4.1C) show a narrow size distribution pattern with a hydrodynamic diameter of ~ 27 nm (Figure 4.1A and Figure C.4). The narrow distribution confirms that the peptides are monomer in freshly dissolved solution at early time points. However, with increasing the incubation time period for **TK9**, **TY5** and **YR5**, the size distribution profile became wider, which accounts for the presence of polymeric subunits in solution (Figure C.4). After 15-days of incubation, clear distinctions in the hydrodynamic diameters were observed for the peptides. **TK9** and **TY5** showed the highest change in hydrodynamic diameter, whereas **YR5** showed a moderate change in size distribution only after 25 days of incubation (Figure C.4). On the other hand, **SK4** showed a negligible amount of change in hydrodynamic diameter within a period of 25 days of incubation, which suggests its lower aggregating propensity. This trend pointed out that aromatic amino acids (Tyr) of these peptides may contribute significantly to the shape and size of their nanostructure assemblies and that polar amino acids may not directly influence their size. Overall, our DLS results proved a similar aggregation behavior of the parent peptide **TK9** and its N-terminal fragments **TY5** and **YR5** can be seen after 25 days of incubation.

Furthermore, circular dichroism (CD) spectroscopy was used to monitor the secondary structure of the peptide fragments at different incubation time (Figure 4.1B-E). Freshly prepared **TK9** and its truncated shorter fragments showed a strong negative maximum at ~195 nm, characteristic of random coil conformation of the peptides or proteins (Figure 4.1B-E).

Interestingly, after 15 days of incubation, samples containing **TK9** and **TY5** showed distinct β-sheet type CD spectral signature consisting of positive maximum at 200 nm and a negative maximum at 215 nm due to n - π^* and π - π^* transition (Figure 4.1B and 4.1C). In contrary, the CD spectrum of **YR5** showed two peaks, one at ~ 198 nm and another broad peak at ~ 215 nm (Figure 4.1D). Similarly, **SK4** showed a large broadening of peaks (Figure 4.1E). This result clearly signifies that both **YR5** and **SK4** are highly dynamic in nature and there may be conformational exchange between random coils to β-sheet in a dynamic state (Figure 4.1D-E). Overall the CD data identified that **TK9** and **TY5** undergo structural reorganization from random coil to β-sheet over time while the other fragments are not prone to this similar conformational change.

Morphology of TK9 and its variants. To understand further about the morphological change of the nanostructures of the peptide self-assembly, various electron microscopic techniques such as transmission electron microscopy (TEM) and scanning electron microscopy (SEM) were employed. TEM data revealed that freshly prepared **TK9** did not show any measureable structure (data not shown), which is in very good agreement with the CD data (Figure 4.1B). However, TEM analysis of the sample containing **TK9** alone with 10 days of incubation displayed a dense fibrillar network which has slight amorphousity and unbranched characteristics (Figure 4.2A and inset, respectively), suggesting that the peptide region are able to form β-sheet morphology, which could be in good agreement with the TEM images of β-sheet forming amyloid fibrils originated from either Aβ or hIAPP.[43] The effect of fibrillation was pronounced for both **TK9** and **TY5** which sequence consisting beta branched amino acids such as Thr1-Val2-Tyr3-Val4-Tyr5 residues. In addition, these residues are prone to form a plane of β-sheet structures (Figure 4.2B). The structure of **TK9** emphasized that the rate of nucleation for the β-sheet formation

could be slower due to presence of two positive charge residues, Arg7 and Lys9 at the C-terminal of the peptide sequence, but our DLS data suggests that they fibrilize with similar kinetics. In contrast, **YR5** and **SK4** did not show any defined nanostructure by TEM (data not shown), which could be attributed to the sole presence of charged residues at the C-terminal of **TK9** sequence which did not allows the peptides to self assemble.

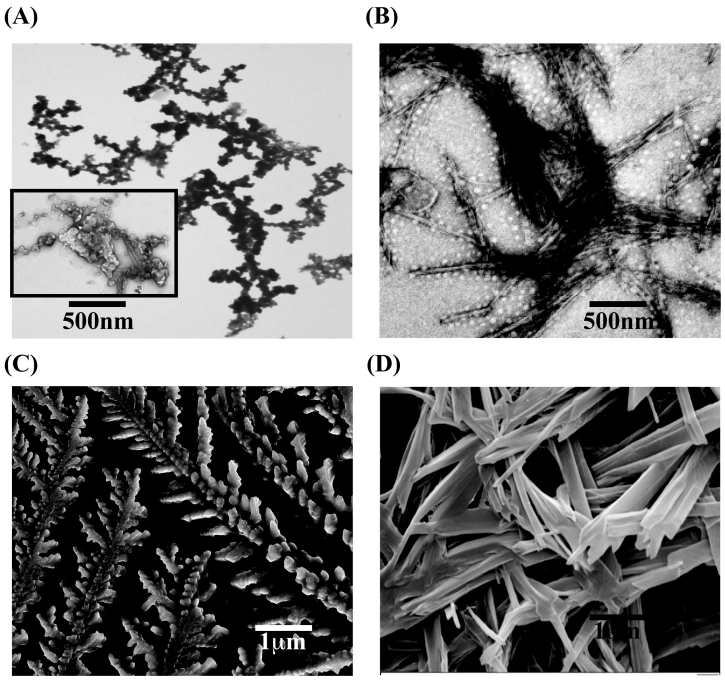

Figure 4.2. Transmission and scanning electron micrographs showing fibrillar nanostructure morphology for **TK9** (A and C) and **TY5** (B and D), respectively.

Subsequently, SEM experiments were performed to understand the self-assembly propensity of **TK9** and its analogues after incubation at 37 °C for several days (Figure 4.2C-D). **TK9** exhibited well-defined, branched, long rod-like fibers (Figure 4.2C) after 25 days. The truncated analogue, **TY5** showed a dense nano-tubular architecture (Figure 4.2D). These results indicate that both **TK9** and **TY5** form fibrils in solution. In contrary, the central region of the peptide sequence, **YR5** showed an amorphous like architecture rather than uniformly well-

defined fibers and tubes (Figure C.5). The C-terminal truncated peptide, **SK4** consists of the charged residues (Ser6, Arg7 and Lys9) did not allow the peptide to adopt any particular structure (Figure C.5). Taken together, **TK9** and **TY5** self assembled to adopt a well-defined nanostructure confirmed by both TEM and SEM.

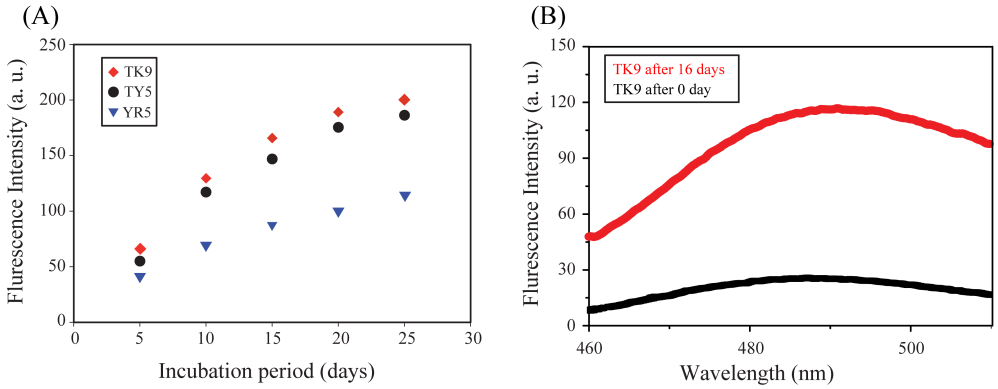

Figure 4.3. (A) Tyrosine fluorescence of **TK9** (red), **TY5** (black) and **YR5** (blue) monitoring increase in Tyr fluorescence signal as peptide aggregates. (B) Thioflavin T (ThT) fluorescence assay measuring β-sheet rich fibril formation of freshly dissolved **TK9** (black) and after 16 days of **TK9** incubation (red).

Fluorescence measurements to monitor peptide aggregation. The intrinsic fluorescence property of tyrosine (Tyr) for **TK9**, **TY5** and **YR5** was used as a probe to determine structural perturbation of the peptides upon incubation and the putative role of the interactions involved. It is noteworthy to mention that there are two Tyr residues in each of the peptide. The intensity for emission maxima of Tyr was increased gradually with increasing the incubation time period for **TK9** as well as **TY5** and **YR5** (Figure 4.3A). This enhancement was attributed to the change in the local environment of the fluorophore from a hydrophilic to a more hydrophobic environment. Initially, the Tyr residues were randomly oriented in solution where solvent molecule could easily quench their fluorescence intensity. However, the fluorescence emission maxima

increased almost 4 times for **TK9** and **TY5** from 5 days of incubation time to 25 days of incubation time (Figure 4.3A). In contrast, the emission maxima of **YR5** increased much less compared to that of **TK9** (Figure 4.3A). Conversely, the incremental increase in fluorescence intensity of emission maxima for **YR5** was negligible and reached a plateau after 25 days of incubation (Figure 4.3A), suggesting YR5 may not form an ordered aggregate in solution.

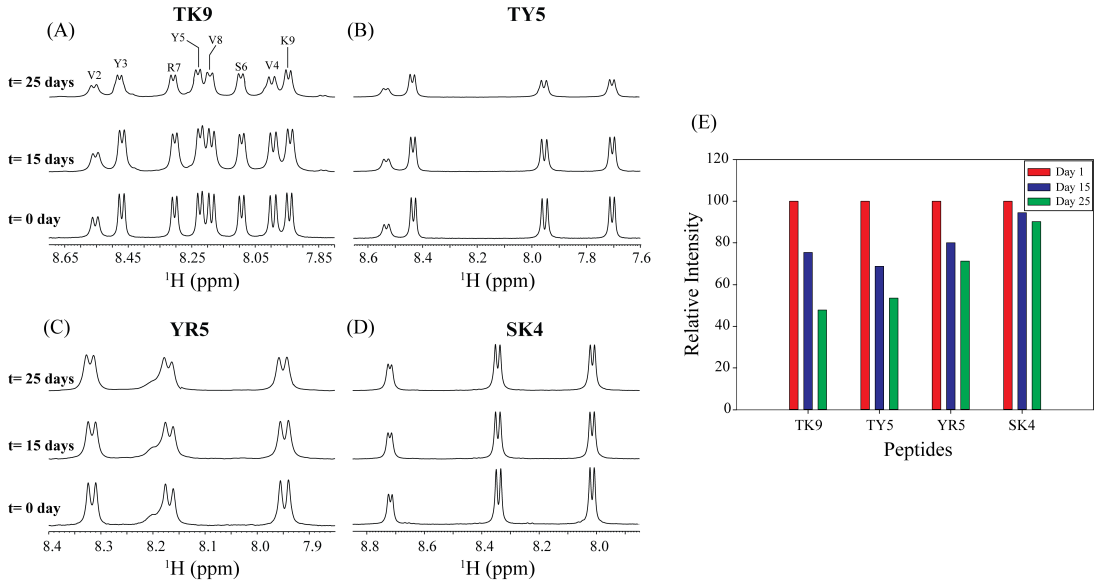

Figure 4.4. (A) Amide proton chemical shift regions of ^{1}HNMR spectra of **TK9** (A), **TY5** (B), **YR5** (C) and **SK4** (D); (E) average decrease in peak intensity for each peptide. Spectra obtained after 0, 15 and 25 days incubation period are overlaid.

Furthermore, thioflavin T (ThT) assays was performed to measure the higher order aggregation of **TK9** over time. It is noteworthy to mention that, ThT is small molecule and specifically bind to the β-sheet rich amyloid fibrils.[44] Figure 4.3B shows the fluorescence intensity of ThT, binding to peptide, **TK9**. The freshly dissolved **TK9**, incubated with ThT demonstrated very low fluorescence intensity. However as **TK9** allowed to self assemble for 16-days, a greater extent of fluorescence intensity of ThT at approx. 490 nm was displayed,

indicative of the presence of a β-sheet rich species. This result further confirms that the aggregation propensity of **TK9** in solution increases over time. Collectively, these results suggest that the non-covalent π-π stacking interaction between the Tyr residues in the supramolecular structures of the aggregated states create a hydrophobic environment (β-sheet structure) where the entrance of water molecule is restricted and hence enhances the fluorescence emission maxima and interacts with the ThT dye.

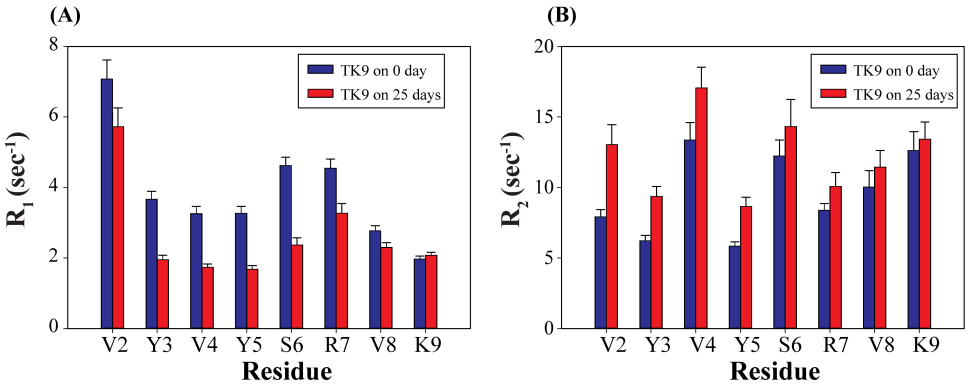

Figure 4.5. The residue-wise relaxation profile for freshly prepared **TK9** (blue) and 25 days incubated **TK9** (red). (A) Longitudinal relaxation rate (R_1) and (B) transverse relaxation rate (R_2) are plotted for each residue of **TK9**.

^{1}H NMR confirms the aggregation propensity of TK9. NMR spectrum of TK9, or its analogs, exhibited well-resolved narrow amide proton peaks indicating that the peptides are highly dynamic in aqueous solution (Figure 4.4). A 2D TOCSY, in conjunction with ROESY, spectrum was used to assign the peaks (Figure C.6). The ROESY spectrum of **TK9** contained intra-residue αN (i, i) as well as sequential, αN (i, i+1) ROEs between backbone and side chain resonances (Figure C.6A), and no medium range αN (i to i+2/i+3/i+4) or long-range αN (i to ≥i+5) cross peaks were observed, indicating that the peptide does not adopt any folded conformation (Figure C.6 and C.7). In addition, ΔHα values of the residues did not show any

pattern of secondary structure (data not shown). A total of 47 ROEs (Table C.2) were used to calculate the random coil structure of **TK9** (Figure C.7), which is also confirmed by the CD data (Figure 4.1).

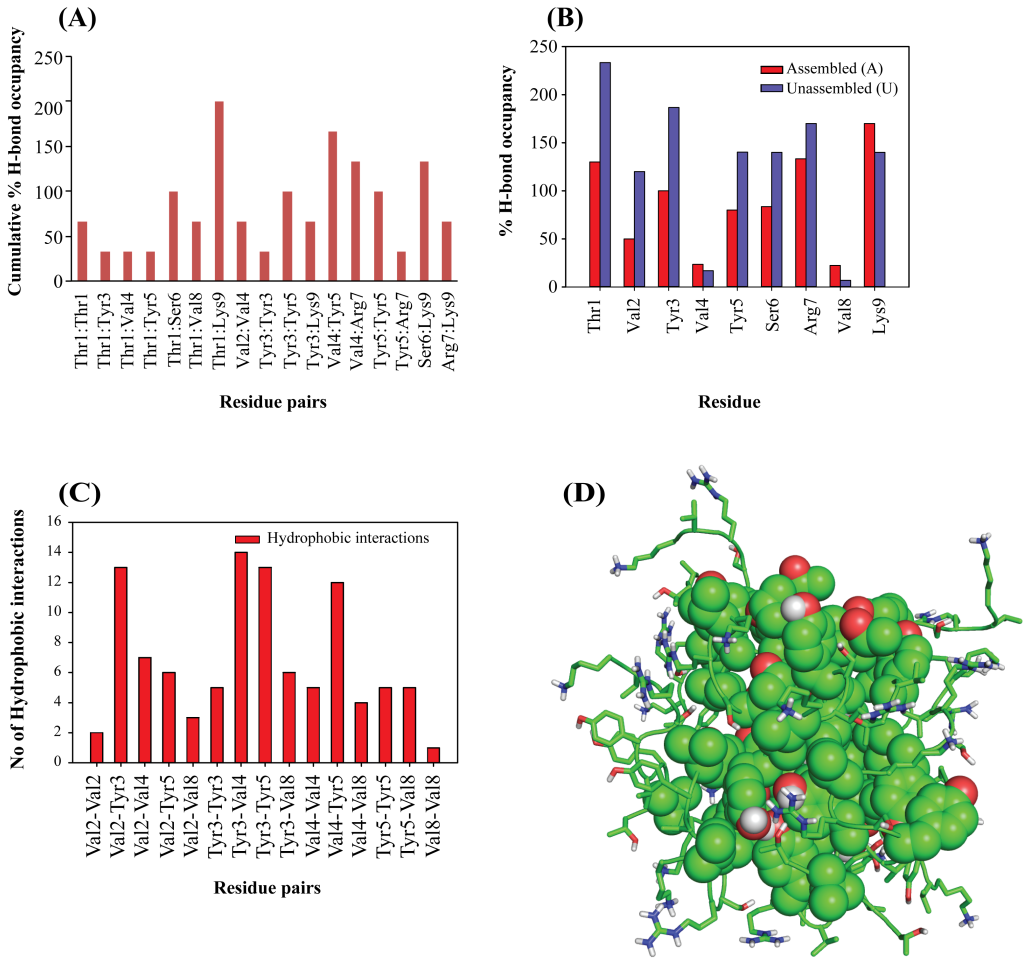

Figure 4.6. (A) Pairwise hydrogen bond analysis between any two monomers. Cumulative % H bond occupancy is calculated for respective residue pair in each peptide. (B) Percentage of H-bond occupancy of respective residue in each monomer was calculated to understand the amino acid-solvent interactions. Red bar represents the assembled and blue bar represents unassembled aggregation of each monomer of TK9. (C) Total number of hydrophobic interactions for respective residue pair is calculated for all the peptides forming cluster. (D) Oligomeric structure of **TK9** is stabilized by hydrophobic hub consisting Tyr, Val, Ser and Thr residues. Positively charged residues are exposed to water.

To determine the extent of aggregation as a function of time, we collected a series of 1D ^{1}H NMR spectra of all the peptides in different time intervals of incubation. Figure 4.4 shows the amide proton chemical shift regions for **TK9** and its analogues at the same time intervals. While freshly prepared peptides exhibited well-dispersed narrow peaks from amide protons, line broadening was observed with time of incubation (Figure 4.4A-4D). **TK9** and **TY5** showed the highest amount of line broadening with respect to time, whereas **SK4** showed the least line broadening (Figure 4.4E). The observed line broadening in NMR spectra could be due to the formation of high molecular weight peptide aggregation. This effect was further confirmed by proton relaxation studies.

^{1}H NMR relaxation studies are used extensively as a sensitive probe to investigate the weak interactions (dissociation constant, K_d ~ μM to mM range) in peptide oligomerization.[45] The formation of high molecular weight oligomers, associated with an increase in correlation times, (τ_c) is revealed by a decrease in longitudinal relaxation rates (R_1) as reported in Figure 4.5A for the N-terminal residues of **TK9**, Val2-Arg7 (Figure 4.5A). On the other hand, the increase in the aggregation size of the species resulted an increase in the transverse relaxation rates (R_2) for all the residues of TK9 in the aged sample as compared to that in the freshly prepared sample as shown in Figure 4.5B. However, the charged C-terminal residues, Arg7-Val8-Lys9, that are more mobile showed less increment of R_2 values for the aged sample of **TK9**. Overall, the observed relaxation data suggest the formation of high molecular weight oligomers in aged samples of **TK9**.

Simulations suggest that both local and global orientation of TK9 may influence aggregation. The above experimental result motivated us to determine the mechanism of aggregation of a small peptide, **TK9**. Interestingly, among the nine amino acid residues, there are

two aromatic amino acid residues, Tyr, three hydrophobic Val residues, two positive charge Lys and Arg and two β-branched amino acid residues, Thr and Ser. The NMR derived extended conformation of **TK9** (Figure C.6C) was used as an initial structure for the coarse grained (CG) molecular dynamics (MD) simulation. It is noteworthy to mention that the self-assembly of a short peptide occurs at a μs time scale, and hence it is a time consuming process to carry out all atom MD simulation.[46] To overcome this problem, coarse-grained MD simulation was adopted to study the aggregation of **TK9** with twenty **TK9** peptide chains.

Figure C.2 summarizes the stages of aggregation of **TK9**. Interestingly, the scattered monomers started self-assembling after 27 ns of simulation and the cluster size was increasing as the time progressed. Finally, after 999 ns of simulation, fifteen out of twenty **TK9** peptide chains were self-assembled to form the **TK9** aggregate (Figure C.2). The remaining five **TK9** monomers were still scattered after 1 μs of simulation. Next, we wanted to understand the driving force of the aggregation for **TK9**. The secondary structure analysis of the assembled as well as the scattered molecules were performed using the Stride web interface.[47] Interestingly, we found that the 60% of conformation of assembled peptide possess a beta turn and more than 35% of conformation exists as random coil (Table C.3).

Closer inspection indicated that the self-assembly of **TK9** (Figure 4.6) was stabilized by a variety of interactions, such as H-bonding, electrostatic, π-cation and van der Waals. The C-terminal positively charged Lys9 residue of **TK9** contributed for a H-bonding interaction with Thr1 and with Ser6. In addition, H-bonding contributions were also observed between Thr1-Ser6, Tyr3-Tyr5, Val4-Tyr5, Val2-Val4 and Thr1-Thr1 of **TK9** in an assembled state. Apart from the H-bonding interactions between two self-assembled monomers, polar residues such as Arg7 and Lys9 formed numerous intermolecular salt bridge interactions (Table C.4).

Hydrophobic contacts were also observed between Val2-Tyr3, Val4-Tyr3, TYR5-Val4, Val2-Val4, Val2-Tyr5 and Tyr3-Val8, which may also play an important role in the aggregated form of **TK9** (Figure 4.6). Interestingly, Tyr3-Tyr3, Tyr5-Tyr5 and Tyr3-Tyr5 aromatic interactions between two monomers of **TK9** aggregates were crucial for stabilization. This result was in very good agreement with the Tyr fluorescence intensity enhancement in the aggregated state (Figure 4.6). A few cation-π interactions between Tyr3-Arg7, Tyr5-Arg7 and Tyr5-Arg9 were also observed in the fibrillar **TK9** (Table C.5).

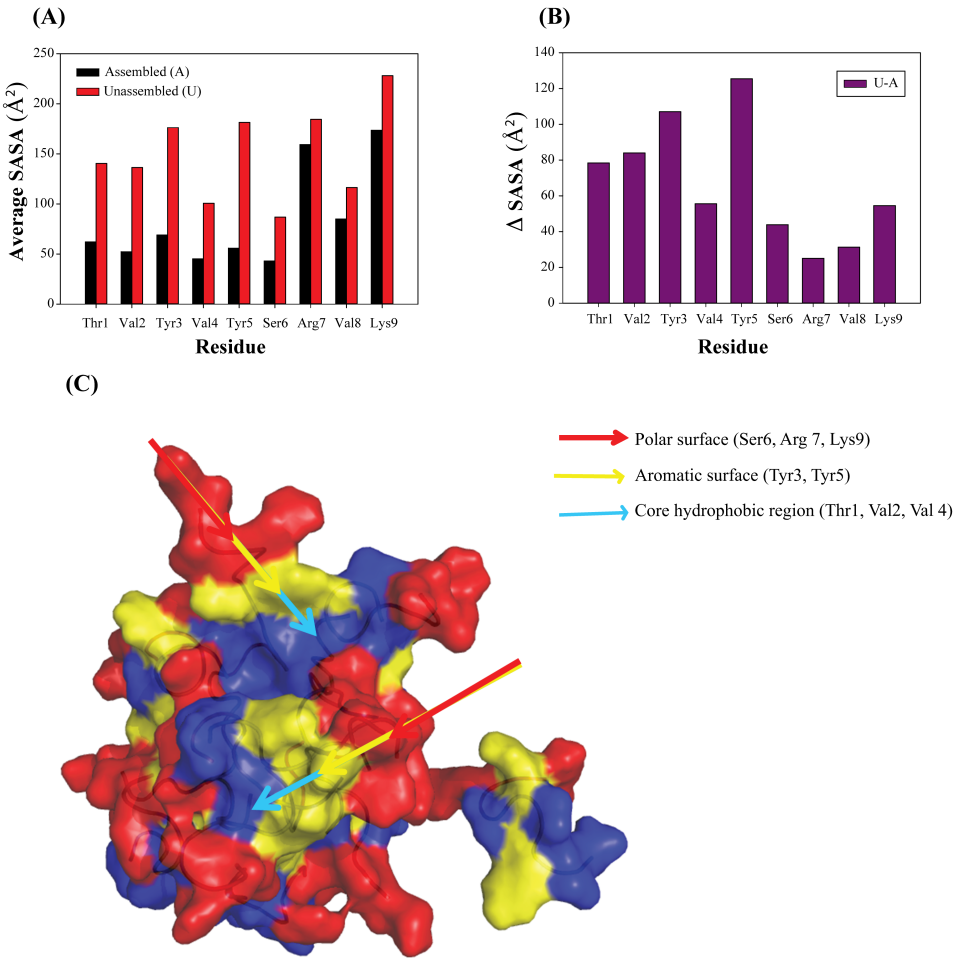

Figure 4.7. (A) Comparative analysis of the average SASA for each residue in assembled and unassembled state. Black represents the assembled state while red represents the unassembled

state. (B) ΔSASA (ΔSASA=$SASA_{unassembled}$ - $SASA_{assembled}$) values for each residue. (C) Surface view of cluster illustrating polarities of residues with color discrimination.

Solvent accessible surface area (SASA) data was evaluated to suggest the conformation of the biomolecule. The SASA values of each residue of **TK9** aggregate as well as in the scattered monomers after 1 μs of simulation were calculated (Figure 4.7) and it was clear that the overall SASA values for all the residues in the cluster or aggregated form was lower, whereas, the same amino acid residues in the scattered peptides (monomer) were much higher. The standard deviation of SASA values of each residue of scattered peptides was less compared to that of aggregated peptides. This behavior could be due to folded conformation in the aggregated form and hence they were less accessible to the solvent. On the other hand, the short peptide **TK9** is highly dynamic in nature and therefore, the peptide is more solvent exposed in the unfolded form. Interestingly, the C-terminal residues, Arg7, Val8 and Lys9 showed comparably higher SASA values both in the scattered as well as in the aggregated form (Figure 4.7). Taken together, the central stabilization of the assembly of **TK9** was due to the strong van der Waals interactions between hydrophobic Val residues as well as between aromatic Tyr residues. In comparison, the Arg7 and Lys9 residues of **TK9** aggregates were pointing towards the solvent to form H-bond with the solvent water molecules.

TK9 inhibits hIAPP aggregation. In order to uncover the potential role of the self-assembling **TK9** peptide on amyloid aggregation, it was co-incubated with freshly dissolved hIAPP and assayed using ThT to monitor β-sheet rich fibril formation. At a stoichiometric concentration of **TK9** monomer, hIAPP still adopted a normal course of aggregation; however, the lag phase was increased and the total fibrillar hIAPP fluorescence intensity was decreased (Figure 4.8A). With the increased concentration of **TK9**, hIAPP aggregation was completely diminished. Similarly,

incubation of freshly dissolved hIAPP with excess **TK9** over 8 hr displayed mainly a random coil peptide in solution as shown by CD experiments (Figure 4.8B). When **TK9** fibril was added to hIAPP solution, aggregation of hIAPP was slightly modified, suggesting possible interactions between **TK9** and hIAPP.

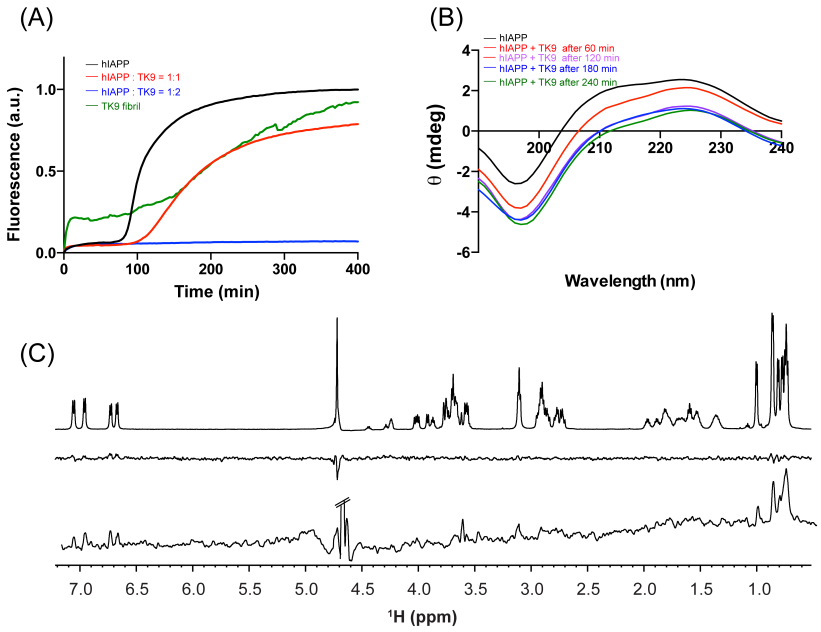

Figure 4.8. (A) ThT fluorescence assay of hIAPP (black) solution incubated with 1 (red) and 2 (blue) equivalents of **TK9**; ThT aggregation of **TK9** peptide in solution is shown in the green trace. (B) CD spectra of freshly dissolved hIAPP (black) and hIAPP incubated over 6 hours with 2 equivalents of **TK9** at the indicated time intervals of aggregation. (C) One dimensional ^{1}H NMR spectrum of freshly dissolved **TK9** in hIAPP (monomer) (top, control); STD spectrum in the presence of hIAPP monomer at t = 12 h. (middle) and in the presence of hIAPP fibril (bottom).

The inhibition of hIAPP aggregation by **TK9** was further confirmed by ^{1}H STD NMR experiments. STD has become a valuable technique to map the interaction of ligands with biomolecules.[48-50] Freshly prepared hIAPP monomers were added to a solution of **TK9** monomers and monitored by NMR for more than 12 hr. Receptor, hIAPP, as well as the ligand, **TK9**, are low-molecular weight molecules; therefore, no STD signals from **TK9** in the presence

of hIAPP monomers were observed due to the fast tumbling of **TK9**. However, if hIAPP fibrillizes, it should be possible to transfer the magnetization from the large-size hIAPP fibrils to **TK9** peptide in STD experiments. But, the fact that we did not observe STD signal within a period of 12 hours indicates that hIAPP did not exist in fibrillar form (Figure 4.8C), as hIAPP (in the absence of **TK9**) completely fibrilizes within 3 hours at the same condition as seen by the ThT assay (Figure 4.8C). In addition, when **TK9** monomers were incubated with hIAPP fibrils, a pronounced STD signal was observed from aromatic as well as aliphatic amino acid residues, indicating that the aromatic and methyl protons are responsible for interacting with fibrillar hIAPP. These observations confirm the ability of **TK9** to inhibit hIAPP aggregation to form an ordered secondary structure.

DISCUSSION

According to the current trend in nanoscience, synthetic amphiphilic small peptides emerge as versatile building block for the fabrication of supramolecular architecture.[51] The ability of these peptides to assemble into ordered nanostructures may help to better understand the natural misfolding pathway of systems such as amyloid proteins.[52] In these systems, short peptide fragments in the wild-type sequence (KLVFF for amyloid-β and NFGAIL for hIAPP) have been identified to be responsible for β-sheet formation thus more clearly investigating the properties and features of small peptide assemblies can help in better understanding larger protein systems.[53-55] The self-assembly regions have also served as a template to rationally design amyloid inhibitors by blocking β-sheet formation, therefore; short peptide fragments of amyloid proteins can also help elucidate possible sequence motifs for therapeutic design and development.[56-58]

The aim of this study has been to reveal self-assembly activity of the ultra small peptide, **TK9** and its variants through biophysical, NMR and computational methods. **TK9** and **TY5** both contain branched, bulky amino acids and a specific sequence (VxVx, Scheme 4.1) that has been shown to be prone to amyloid-like aggregation.[59] Over time, **TK9** spontaneously aggregated in aqueous solution as seen by DLS (Figure 4.1) to adopt rod-like fibrillar morphology, confirmed by microscopic studies (Figure 4.2). Interestingly, the aggregation was β-sheet rich, examined by the increase in ThT fluorescence (Figure 4.3). All four peptides adopt a random coil monomeric conformation at early time points; however, CD experiments confirmed that **TK9** and **TY5** form into a β-sheet containing fibrillar species after incubation over days (Figure 4.1B and 4.1C). In addition, because of the presence of the "amyloid aggregation-prone" sequence motif, a further explanation for the aggregation propensity of **TK9** and **TY5** may be the increase in hydrophobic and aromatic residues, which may favor hydrophobic contacts and π-π interactions as well as undergo a transition to β-sheet during self-assembly more readily than peptides with aliphatic residues.[59]

Structurally different, **YR5** and **SK4**, which do not contain the aggregation-prone sequence, did not show this transition to β-sheet nor did they show an enhanced ThT fluorescence, suggesting an ill-defined secondary structure. The distribution profile of the peptides is also varied upon aggregation as suggested by the DLS studies (Figure 4.1A). As the peptides were incubated, the size of the species increased, which may be attributed to the fibril-like aggregates formed in the case of **TK9** and **TY5**. The π-π interactions could be the governing factor for the folding of the peptide into supramolecular assemblies as seen by Tyr fluorescence experiments (Figure 4.3). As **TK9** is allowed to self-assemble, it forms a hydrophobic core, which does not allow for interactions with water, and thus an enhancement in the Tyr

fluorescence signal by neighboring Tyr residues. Coarse grain MD simulation confirms that the self-assembled oligomer of **TK9** is stabilized by hydrophobic amino acid residues such as Tyr and Val from individual monomers to form a hydrophobic hub and all the charge residues such as Arg7 and Lys9 are exposed to water (Figure 4.6). In contrary, the solvent quenches the fluorescence intensity of **TK9** or **TY5** monomer (Figure 4.3). However, a well-defined secondary structure of **YR5**, the central region of **TK9**, was not observed. In order to probe the mechanistic insights of self-assembly of a short peptide at an atomic resolution, NMR spectroscopy was carried out.

Proton NMR and relaxation studies further confirm the presence of high molecular weight oligomers in aged samples. In ^{1}H NMR spectra, amide resonances are observed for all of the peptides at initial time points. As the peptides are allowed to self-assemble, significant line broadening is visible for **TK9** and **TY5**, whereas a lesser broadening is seen for **YR5** and **SK4** over the time course (Figure 4.4). The line broadening observed for **TK9** or **TY5** peptides confirms the low correlation times with millisecond to microsecond time scale of motion between several states of micelle-like aggregation. This dynamic behavior may further confirm an aggregation process occurring in solution, specifically the formation of high molecular weight assemblies that tumble slowly in NMR time scale, which gave rise to an increased rotational correlation time (Figure 4.5). The TOCSY and ROSEY data, taken of freshly prepared monomers, show no medium or long range cross peaks (or ROEs), confirming the absence of a well-defined secondary structure (possibly random coil) prior to incubation (Figure C.6).

Furthermore, the applications of these self-assembled peptides are of great value since they do have interesting intrinsic properties; however, their role in understanding protein-protein interactions may also be useful. Investigations of the interaction between amyloid proteins and

other biologically relevant proteins have been of great interest. Specifically, reports regarding the interaction of co-secreted proteins, hIAPP and insulin, has shed light into the involvement of a protein on amyloid formation.[60,61] Aforementioned, small peptide sequence from the native protein have been utilized in the design of amyloid inhibitors due to their ability to contain self-recognition motifs which can interact with the target protein through hydrophobic and electrostatic interactions and prevent polymerization to fibrils.[56,62,63] In order to study this, we tested the inhibitory activity of **TK9** against hIAPP, an amyloid protein suggested to be a pathological feature of type-2 diabetes. Our experimental results indicate that the amyloid-inhibition properties of **TK9** monomers are concentration dependent as shown in Figure 4.8. This observation is similar to that shown for amyloid-inhibiting properties of a 9-residue peptide, NK9 (or ^{45}NIVNVSLVK^{53}) adopted from SARS CoV E-protein, against the fibrillation of insulin.[64] Interestingly, **TK9** monomers are able to modify the aggregation kinetics of hIAPP and completely inhibit the fibril formation upon incubation with excess amount of a **TK9**. This result was further verified by STD NMR experiments, which showed that upon incubation of hIAPP monomers with excess **TK9** monomers, no pronounced STD effect was observed indicating the presence of a small, insufficient amount of hIAPP fibers. On the other hand, when **TK9** monomers are present in a solution along with hIAPP fibrils, a strong STD signal was observed, confirming an interaction between the two peptides.

Overall, the study of self-assembled peptides nanostructures can serve, as useful systems for understanding more global systems, like amyloid proteins kinetics and aggregation at the atomic level. Herein, the aggregation properties of **TK9** and its variants were characterized through biophysical, spectroscopic and simulated studies, and it was confirmed that the structure of these peptides influence their aggregation propensity and fibrillar morphology. **TK9**

underwent a transition to a more β-sheet rich structure, which adopted a fibril-like shape. These aggregates were further investigated through simulations to understand more clearly the possible intra- and inter peptide interactions at the molecular level. As described here, self-assembly peptides may also be useful templates for designing amyloid inhibitor. These self-assembly systems may also be used in understanding the molecular and structural biology which will inspire the design and synthesis of increasingly complex self assembled biomaterials for biomedicine. Furthermore, investigations to probe the structural characteristics of these peptides in the presence of membrane can also be of great value since the amyloid beta or hIAPP protein interacts with membrane before going to fibrillation.[65-67] Therefore, instead of using the entire protein of amyloid-β or hIAPP in membrane, this peptide can be a nanoindicator to understand the structural insight at the membrane surface for the mechanism of fibrillation process.

Funding

AB would like to thank Bose Institute, Kolkata, India for financial support. AG thanks CSIR, Govt. of India for senior research fellowship. SB thanks Bose Institute, Kolkata for M. Sc. – Ph.D fellowship. Central instrument facility (CIF) of Bose Institute is greatly acknowledged. Part of this study, and AB and ASP were supported by funds from NIH (GM084018 to A.R.).

Supporting Information

Table C.1-C.4, and Figures C.1 – C.7 are available in Appendix C

References

1. Gazit, E. (2007) Self-assembled peptide nanostructures: the design of molecular building blocks and their technological utilization, *Chem. Soc. Rev. 36*, 1263-1269.

2. Zhao, X., Pan, F., Xu, H., Yaseen, M., Shan, H., Hauser, C. A., Zhang, S., and Lu, J. R. (2010) Molecular self-assembly and applications of designer peptide amphiphiles, *Chem. Soc. Rev. 39*, 3480-3498.

3. Zhang, S. (2003) Fabrication of novel biomaterials through molecular self-assembly, *Nat. Biotechnol. 21*, 1171-1178.

4. Whitesides, G., Mathias, J., and Seto, C. (1991) Molecular self-assembly and nanochemistry: a chemical strategy for the synthesis of nanostructures, *Science 254*, 1312-1319.

5. Lecommandoux, S., Achard, M.-F., Langenwalter, J. F., and Klok, H.-A. (2001) Self-assembly of rod-coil diblock oligomers based on α-helical peptides, *Macromolecules 34*, 9100-9111.

6. Lawrence, D. S., Jiang, T., and Levett, M. (1995) Self-assembling supramolecular complexes, *Chem. Rev. 95*, 2229-2260.

7. Bhunia, A., Saravanan, R., Mohanram, H., Mangoni, M. L., Bhattacharjya, S. (2011) NMR structures and interactions of temporin-1TI and temporin-1Tb with lipopolysaccharide micelles: mechanistic insights into outer membrane permeabilization and synergistic activity, *J. Biol. Chem*. 286, 24394-24406.

8. Saravanan, R., Joshi, M., Mohanram, H., Bhunia, A., Mangoni, M. L., Bhattacharjya, S. (2013) NMR structure of temporin 1 ta in lipopolysaccharide micelles: mechanistic insights into inactiation by outer membrane, *PLoS One* 8, e72718.

9. Lakshmanan, A., Zhang, S., and Hauser, C. A. (2012) Short self-assembling peptides as building blocks for modern nanodevices, *Trends Biotechnol. 30*, 155-165.

10. Hosseinkhani, H., Hong, P.-D., and Yu, D.-S. (2013) Self-assembled proteins and peptides for regenerative medicine, *Chem. Rev. 113*, 4837-4861.

11. Yemini, M., Reches, M., Rishpon, J., and Gazit, E. (2005) Novel electrochemical biosensing platform using self-assembled peptide nanotubes, *Nano Lett. 5*, 183-186.

12. Ross, C. A., and Poirier, M. A. (2004) Protein aggregation and neurodegenerative disease.

13. Knowles, T. P., Vendruscolo, M., and Dobson, C. M. (2014) The amyloid state and its association with protein misfolding diseases, *Nat. Rev. Mol. Cell Biol. 15*, 384-396.

14. Chiti, F., and Dobson, C. M. (2006) Protein misfolding, functional amyloid, and human disease, *Annu. Rev. Biochem. 75*, 333-366.

15. Lu, K., Jacob, J., Thiyagarajan, P., Conticello, V. P., and Lynn, D. G. (2003) Exploiting amyloid fibril lamination for nanotube self-assembly, *J. Am. Chem. Soc. 125*, 6391-6393.

16. Wilson, L., Mckinlay, C., Gage, P., and Ewart, G. (2004) SARS coronavirus E protein forms cation-selective ion channels, *Virology 330*, 322-331.

17. Verdiá-Báguena, C., Nieto-Torres, J. L., Alcaraz, A., DeDiego, M. L., Torres, J., Aguilella, V. M., and Enjuanes, L. (2012) Coronavirus E protein forms ion channels with functionally and structurally-involved membrane lipids, *Virology 432*, 485-494.

18. Li, Y., Surya, W., Claudine, S., and Torres, J. (2014) Structure of a Conserved Golgi Complex-targeting Signal in Coronavirus Envelope Proteins, *J. Biol. Chem. 289*, 12535-12549.

19. Chan, W. C., and White, P. D. (2000) *Fmoc solid phase peptide synthesis*, Oxford University Press.

20. Ghosh, A., Datta, A., Jana, J., Kar, R. K., Chatterjee, C., Chatterjee, S., and Bhunia, A. (2014) Sequence context induced antimicrobial activity: insight into lipopolysaccharide permeabilization, *Mol. BioSyst. 10*, 1596-1612.

21. Lakowicz, J. R. (2007) *Principles of fluorescence spectroscopy*, Springer.

22. Goddard, T., and Kneller, D. (2004) SPARKY 3, *University of California, San Francisco 14*, 15.

23. Güntert, P. (2004) Automated NMR structure calculation with CYANA, In *Protein NMR Techniques*, pp 353-378, Springer.

24. Ghosh, A., Kar, R. K., Jana, J., Saha, A., Jana, B., Krishnamoorthy, J., Kumar, D., Ghosh, S., Chatterjee, S., and Bhunia, A. (2014) Indolicidin Targets Duplex DNA: Structural and Mechanistic Insight through a Combination of Spectroscopy and Microscopy, *ChemMedChem 9*, 2052-2058.

25. Ghosh, A., Kar, R. K., Krishnamoorthy, J., Chatterjee, S., and Bhunia, A. (2014) Double GC: GC Mismatch in dsDNA Enhances Local Dynamics Retaining the DNA Footprint: A High‐Resolution NMR Study, *ChemMedChem 9*, 2059-2064.

26. Marrink, S. J., de Vries, A. H., and Mark, A. E. (2004) Coarse grained model for semiquantitative lipid simulations, *J. Phys. Chem. B 108*, 750-760.

27. Marrink, S. J., Risselada, H. J., Yefimov, S., Tieleman, D. P., and de Vries, A. H. (2007) The MARTINI force field: coarse grained model for biomolecular simulations, *J. Phys. Chem. B 111*, 7812-7824.

28. Hess, B., Kutzner, C., Van Der Spoel, D., and Lindahl, E. (2008) GROMACS 4: Algorithms for highly efficient, load-balanced, and scalable molecular simulation, *J. Chem. Theory Comput. 4*, 435-447.

29. Rzepiela, A. J., Schäfer, L. V., Goga, N., Risselada, H. J., De Vries, A. H., and Marrink, S. J. (2010) Reconstruction of atomistic details from coarse‐grained structures, *J. Comput. Chem. 31*, 1333-1343.

30. Hoover, W. G. (1985) Canonical dynamics: equilibrium phase-space distributions, *Phys. Rev. A. 31*, 1695.

31. Oostenbrink, C., Villa, A., Mark, A. E., and Van Gunsteren, W. F. (2004) A biomolecular force field based on the free enthalpy of hydration and solvation: The GROMOS force‐field parameter sets 53A5 and 53A6, *J. Comput. Chem. 25*, 1656-1676.

32. Cohen, J. R., Lin, L. D., and Machamer, C. E. (2011) Identification of a Golgi complex-targeting signal in the cytoplasmic tail of the severe acute respiratory syndrome coronavirus envelope protein, *J. Virol. 85*, 5794-5803.

33. Fukushi, S., Mizutani, T., Sakai, K., Saijo, M., Taguchi, F., Yokoyama, M., Kurane, I., and Morikawa, S. (2007) Amino acid substitutions in the s2 region enhance severe acute respiratory syndrome coronavirus infectivity in rat angiotensin-converting enzyme 2-expressing cells, *J. Virol. 81*, 10831-10834.

34. Nieto-Torres, J. L., DeDiego, M. L., Álvarez, E., Jiménez-Guardeño, J. M., Regla-Nava, J. A., Llorente, M., Kremer, L., Shuo, S., and Enjuanes, L. (2011) Subcellular location and topology of severe acute respiratory syndrome coronavirus envelope protein, *Virology 415*, 69-82.

35. Ruch, T. R., and Machamer, C. E. (2011) The hydrophobic domain of infectious bronchitis virus E protein alters the host secretory pathway and is important for release of infectious virus, *J. Virol. 85*, 675-685.

36. Halverson, K., Fraser, P. E., Kirschner, D. A., and Lansbury Jr, P. T. (1990) Molecular determinants of amyloid deposition in Alzheimer's disease: conformational studies of synthetic. beta.-protein fragments, *Biochemistry 29*, 2639-2644.

37. Remington, J. S., Klein, J. O., Wilson, C. B., Nizet, V., and Maldonado, Y. (2001) Infectious diseases of the fetus and newborn, *Infectious Disease of the Fetus and Newborn 12*, 643-681.

38. Do, T. D., LaPointe, N. E., Sangwan, S., Teplow, D. B., Feinstein, S. C., Sawaya, M. R., Eisenberg, D. S., Bowers, M. T. (2014) Factors that drive peptide assembly from native amyloid structures: experimental and theoretical analysis of [leu-5]-enkephalin mutants, *J. Phys. Chem. B.* 118, 7247-7256.

39. Ye, W., Chen, Y., Wang, W., Yu, Q., Li, Y., Zhang, J., Chen, H. F. (2012) Insight into stability of cross-β amyloid fibril from VEALYL short peptide with molecular dynamics simulations, *PLoS One*, 7, e36382.

40. Do, T. D., LaPointe, N. E., Economou, N. J., Buratto, S. K., Feinstein, S. C., Shea, J. E., Bowers, M. T. (2013) Effects of pH and charge state on peptide assembly: the YVIFL model system, *J. Phys. Chem. B*. 117, 10759-10768.

41. Zheng, J., Baghkhanian, A. M., Nowick, J. S. (2013) A hydrophobic surface is essential to inhibit the aggregation of a tau-protien-derived hexapeptide, *J. Am. Chem. Soc*. 135, 6846-6852.

42. Berne, B. J., and Pecora, R. (2000) *Dynamic light scattering: with applications to chemistry, biology, and physics*, Courier Dover Publications.

43. Westermark, P., Engström, U., Johnson, K. H., Westermark, G. T., and Betsholtz, C. (1990) Islet amyloid polypeptide: pinpointing amino acid residues linked to amyloid fibril formation, *Proc. Natl. Acad. Sci. USA 87*, 5036-5040.

44. Levine, H. (1993) Thioflavine T interaction with synthetic Alzheimer's disease β-amyloid peptides: Detection of amyloid aggregation in solution, *Protein Sci. 2*, 404-410.

45. Esposito, V., Das, R., and Melacini, G. (2005) Mapping polypeptide self-recognition through 1H off-resonance relaxation, *J. Am. Chem. Soc. 127*, 9358-9359.

46. Klein, M. L., and Shinoda, W. (2008) Large-scale molecular dynamics simulations of self-assembling systems, *Science 321*, 798-800.

47. Heinig, M., and Frishman, D. (2004) STRIDE: a web server for secondary structure assignment from known atomic coordinates of proteins, *Nucleic Acids Res. 32*, W500-W502.

48. Bhunia, A., Bhattacharjya, S., and Chatterjee, S. (2012) Applications of saturation transfer difference NMR in biological systems, *Drug Discov. Today 17*, 505-513.

49. Mayer, M., and Meyer, B. (1999) Characterization of ligand binding by saturation transfer difference NMR spectroscopy, *Angew. Chem. Int. Ed. 38*, 1784-1788.

50. Yesuvadian, R., Krishnamoorthy, J., Ramamoorthy, A., and Bhunia, A. (2014) Potent γ-secretase inhibitors/modulators interact with amyloid-β fibrils but do not inhibit

fibrillation: A high-resolution NMR study, *Biochem. Biophys. Res. Commun. 447*, 590-595.

51. Rajagopal, K., and Schneider, J. P. (2004) Self-assembling peptides and proteins for nanotechnological applications, *Curr. Opin. Struct. Biol. 14*, 480-486.

52. Dobson, C. M. (2003) Protein folding and misfolding, *Nature 426*, 884-890.

53. Tjernberg, L. O., Näslund, J., Lindqvist, F., Johansson, J., Karlström, A. R., Thyberg, J., Terenius, L., and Nordstedt, C. (1996) Arrest of-amyloid fibril formation by a pentapeptide ligand, *J. Biol. Chem. 271*, 8545-8548.

54. Kapurniotu, A., Schmauder, A., and Tenidis, K. (2002) Structure-based design and study of non-amyloidogenic, double N-methylated IAPP amyloid core sequences as inhibitors of IAPP amyloid formation and cytotoxicity, *J. Mol. Biol. 315*, 339-350.

55. Gazit, E. (2007) Self assembly of short aromatic peptides into amyloid fibrils and related nanostructures, *Prion 1*, 32-35.

56. Tatarek-Nossol, M., Yan, L.-M., Schmauder, A., Tenidis, K., Westermark, G., and Kapurniotu, A. (2005) Inhibition of hIAPP amyloid-fibril formation and apoptotic cell death by a designed hIAPP amyloid-core-containing hexapeptide, *Chem. Biol. 12*, 797-809.

57. Watanabe, K.-i., Nakamura, K., Akikusa, S., Okada, T., Kodaka, M., Konakahara, T., and Okuno, H. (2002) Inhibitors of fibril formation and cytotoxicity of β-amyloid peptide composed of KLVFF recognition element and flexible hydrophilic disrupting element, *Biochem. Biophys. Res. Commun. 290*, 121-124.

58. Gazit, E. (2005) Mechanisms of amyloid fibril self‐assembly and inhibition, *FEBS J. 272*, 5971-5978.

59. de la Paz, M. L., and Serrano, L. (2004) Sequence determinants of amyloid fibril formation, *Proc. Natl. Acad. Sci. USA 101*, 87-92.

60. Brender, J. R., Lee, E. L., Hartman, K., Wong, P. T., Ramamoorthy, A., Steel, D. G., and Gafni, A. (2011) Biphasic effects of insulin on islet amyloid polypeptide membrane disruption, *Biophys. J. 100*, 685-692.

61. Susa, A. C., Wu, C., Bernstein, S. L., Dupuis, N. F., Wang, H., Raleigh, D. P., Shea, J.-E., and Bowers, M. T. (2014) Defining the Molecular Basis of Amyloid Inhibitors: Human Islet Amyloid Polypeptide–Insulin Interactions, *J. Am. Chem. Soc. 136*, 12912-12919.

62. Tjernberg, L. O., Lilliehöök, C., Callaway, D. J., Näslund, J., Hahne, S., Thyberg, J., Terenius, L., and Nordstedt, C. (1997) Controlling amyloid β-peptide fibril formation with protease-stable ligands, *J. Biol. Chem. 272*, 12601-12605.

63. Mishra, A., Misra, A., Vaishnavi, T. S., Thota, C., Gupta, M., Ramakumar, S., Chauhan, V. S. (2013) Conformationally restrictred short peptides inhibit human islet amyloid polypeptide (hIAPP) fibrillization, *Chem. Commun*. 49, 2688-2690.

64. Banerjee, V., Kar, R. K., Datta, A., Parthasarathi, K., Chatterjee, S., Das, K. P., and Bhunia, A. (2013) Use of a small peptide fragment as an inhibitor of insulin fibrillation process: A study by high and low resolution spectroscopy, *PloS One 8*, e72318.

65. Brender, J. R., Salamekh, S., and Ramamoorthy, A. (2011) Membrane disruption and early events in the aggregation of the diabetes related peptide IAPP from a molecular perspective, *Acc. Chem. Res. 45*, 454-462.

66. Patel, H. R., Pithadia, A. S., Brender, J. R., Fierke, C. A., and Ramamoorthy, A. (2014) In Search of Aggregation Pathways of IAPP and other Amyloidogenic Proteins: Finding Answers Through NMR Spectroscopy, *J. Phys. Chem. Lett.* 5, 1864-1870.

67. Qiang, W., Akinlolu, R. D., Nam, M., and Shu, N. (2014) Structural Evolution and Membrane Interaction of the 40-Residue beta Amyloid Peptides: Differences in the Initial Proximity between Peptides and the Membrane Bilayer Studied by Solid-State Nuclear Magnetic Resonance Spectroscopy, *Biochemistry 53*, 7503-7514.